Phased-Array Antenna-in-Package Technology for Emerging Millimeter Wave Applications

by

Amir Raeesi

A thesis
presented to the University of Waterloo
in fulfillment of the
thesis requirement for the degree of
Doctor of Philosophy
in
Electrical and Computer Engineering

Waterloo, Ontario, Canada, 2022

Examining Committee Membership

The following served on the Examining Committee for this thesis. The decision of the Examining Committee is by majority vote.

External Examiner: Tayeb A. Denidni
Professor, Centre Energie Materiaux Telecommunications,
Institut National de la Recherche Scientifique (INRS)

Supervisors: 1- Kankar Bhattacharya
Professor, Dept. of Electrical & Computer Engineering,
University of Waterloo
2- Wael Mahmoud Abdel-Wahab
Research Associate Professor,
Dept. of Electrical & Computer Engineering,
University of Waterloo

Internal Member: John Long
Professor, Dept. of Electrical & Computer Engineering,
University of Waterloo

Internal Member: Raafat Mansour
Professor, Dept. of Electrical & Computer Engineering,
University of Waterloo

Internal-External Member: Ehsan Toyserkani

Professor, Dept. of Mechanical & Mechatronics Engineering,

University of Waterloo

Defense Chair: Melanie Campbell

Professor, Dept. of Physics & Astronomy,

University of Waterloo

AUTHOR'S DECLARATION

I hereby declare that I am the sole author of this thesis. This is a true copy of the thesis, including any required final revisions, as accepted by my examiners.

I understand that my thesis may be made electronically available to the public.

Abstract

The ever-increasing data rates for wireless technologies (e.g., satellite communications, fifth generation (5G) wireless communications, and automotive radars) has directed the interests towards millimeter wave (mm-Wave) technology that provides wider absolute bandwidth. Relatively small size of antennas at mm-Wave makes large-scale phased-array antenna (PAA) system a feasible solution to compensate for the path loss and alleviate the requirements of the RF transceiver front-ends at mm-Wave.

Despite developments in the military applications for more than 50 years, active PAA systems have been costly for commercial applications. The high cost is mainly due to the discrete implementation of transmit/receive beamforming modules where III-V front-end monolithic microwave integrated circuits (MMICs) (GaAs or InP, or both) are assembled together with silicon-based chips used for address decoders, power management, and general digital control such as phase and gain setting and calibration. A paradigm shift happened when silicon-based phased arrays had been implemented starting with the work at Caltech using silicon-germanium (SiGe) bipolar CMOS (BiCMOS) and Si CMOS technologies. Silicon-based technologies (Si-CMOS and SiGe-BiCMOS) are not costly and are able to be produced in a large scale. On the other side, multilayer antenna-in-package (AiP) technology is currently the prevailing antenna and packaging technology for miscellaneous mm-Wave applications. These two technologies together make low-cost, low-power active PAA possible. A modular and scalable silicon-based phased-array AiP could be the building block for the development of large-scale mm-Wave PAA systems where hundreds to thousands of antenna elements are required in order to provide a reliable communication link. This approach not only ease the complexity of the system, but also makes the implementation of the system over any conformal geometry feasible.

In this thesis, two different architectures for phased-array AiP are presented. The first architecture is a 4×4 active transmit phased-array AiP with polarization control at Ka-band.

The second architecture is a 4×4 bi-directional antenna array with integrated passive beamformer with left-handed circular polarization (LHCP) radiation.

In chapter II, a 4×4 active transmit phased-array AiP with polarization control at Ka-band is discussed. Silicon-based active transmit phased-array AiP is able to realize any kind of polarization including linear and circular polarization besides providing relatively high effective isotropic radiated power (EIRP). The proposed active AiP is modular and scalable and is able to be employed as the unit cell for a large-scale phased-array antenna system. It consists of 16 dual- linearly polarized cavity-backed patch antennas, four 8-channel active beamformers, and a four-way splitter network. The proposed AiP provides 42 dB of active gain at the boresight. The (EIRP) of the current module is 41 dBm at the 1-dB compression point of the active beamformer chips and it consumes 2.6 W of DC power when the system radiates left-handed circular polarization at the boresight. Calibration and radiation pattern measurement of the system is also discussed and the measurement results for a case of left-handed circularly polarized (LHCP) radiation is presented.

In chapter III, a 4×4 bi-directional antenna array with integrated passive beamformer with left-handed circular polarization (LHCP) radiation is presented. Hybrid approach that combines active and passive PAA architectures is an alternative solution in lowering the cost and complexity of active PAA systems. The design and implementation aspects of a 4×4 antenna array with integrated passive beamformer for low-cost and efficient millimeter wave applications is presented. The phase shifter's operational principle and actuation mechanism are discussed in detail. Slow-wave structure is employed to shrink the size of the phase shifter. The simulation and measurement results of the phase shifter are presented. Measurement results show the maximum insertion loss of 2.2 dB in all the tuning states and the insertion loss variation is 1.2 dB. Also, it provides 380º of the phase tuning range in a compact footprint area of 2.4 mm × 3 mm. 2D P-PAA is designed, simulated and measured over the operating band. Measurement results show the antenna‘s main beam can be steered over an angular range of ±30º in both elevation and azimuth planes.. The operating frequency bandwidth of the

system ranges from 28-30 GHz. The antenna's main characteristics, such as radiation pattern, directivity, efficiency, and reflection coefficient are measured and presented.

Acknowledgements

Unfortunately, Prof. Safieddin Safavi-Naeini passed away in October 2021 unexpectedly. He was more than just a mentor to me. I have always been and will be grateful for his support in all the aspects of my professional and personal life. The completion of my Ph.D. program would not be possible without his invaluable comments and suggestions. Although he is not among us anymore, but his legacy will be alive and his significant contribution to the science and technology will continue to inspire academic and industrial researchers around the world.

I would like to thank my thesis committee members, Prof. John Long, Prof. Raafat Mansour, Prof. Ehsan Toyserkani, Prof. Tayeb Denidni, and Prof. Kankar Bhattacharya for their suggestions and comments on my thesis.

I hold two of my mentors during my M.Sc. program at the University of Tehran in high regard, Prof. Jalil Rashed-Mohassel and Prof. Mahmoud Shahabadi, for their comprehensive teaching of EM theory.

I appreciate all of my colleagues at the Centre for Intelligent Antenna and Radio Systems (CIARS), specially Dr. Naimeh Ghaffarian, Dr. Aidin Taeb, Dr. Wael Abdel-Wahab, Dr. Mohammad Reza Nezhad-Ahmadi, and Dr. Reza Rafi for sharing their experiences with me.

At the end, I would like to acknowledge the Natural Sciences and Engineering Research Council of Canada (NSERC) and C-COM Satellites Inc. for funding this research.

Dedication

To the A·R· in 2017, who took the leap

To my family

Table of Contents

List of Figures

List of Tables

Chapter 1- Introduction

1.1 Motivation

The ever-increasing data rates for wireless technologies (e.g., satellite communications, fifth generation (5G) wireless communications, and automotive radars) has directed the interests towards millimeter wave (mm-Wave) frequencies that provide wider absolute bandwidth. Relatively small size of antennas at mm-Wave makes large-scale phased-array antenna (PAA) system a feasible solution to compensate for the path loss and alleviate the requirements of the RF transceiver front-ends at mm-Wave. A PAA is a class of Multiple-Input and Multiple-Output (MIMO) systems by which the radiation pattern can be steered in to a particular or certain number of desired directions and has much less radiation in undesired directions.

The main advantages of mm-Wave phased-array antenna systems are [1]:

- ✓ Large-scale implementation feasibility due to the small wavelength of mm-Wave frequencies.
- ✓ Increased signal level in the receiver at the output of the combiner for a given power density per area at the RX antennas.
- ✓ Increased overall output power, which scales with N (number of antenna elements).
- ✓ Immunity to interferers due to beamforming, but only within the bandwidth of each receiver and only after the signal combination.
- ✓ Immunity to multi-path fading through antenna diversity in both receivers and transmitters.
- ✓ Electronic beamforming and beam steering

The fast electronic steering is realizable in PAA systems obviating the need for any mechanical rotation. Switched-beam antennas, reflect arrays, and lens antennas like transmit arrays are among architectures used in implementing PAAs [2]-[4]. However, the focus of this thesis is on conventional phased-array antenna systems.

Fig. 1-1 shows N radiating antenna elements with different orientation, radiation pattern and polarization located arbitrarily in the space. Each antenna element is excited by a complex number (w_i).

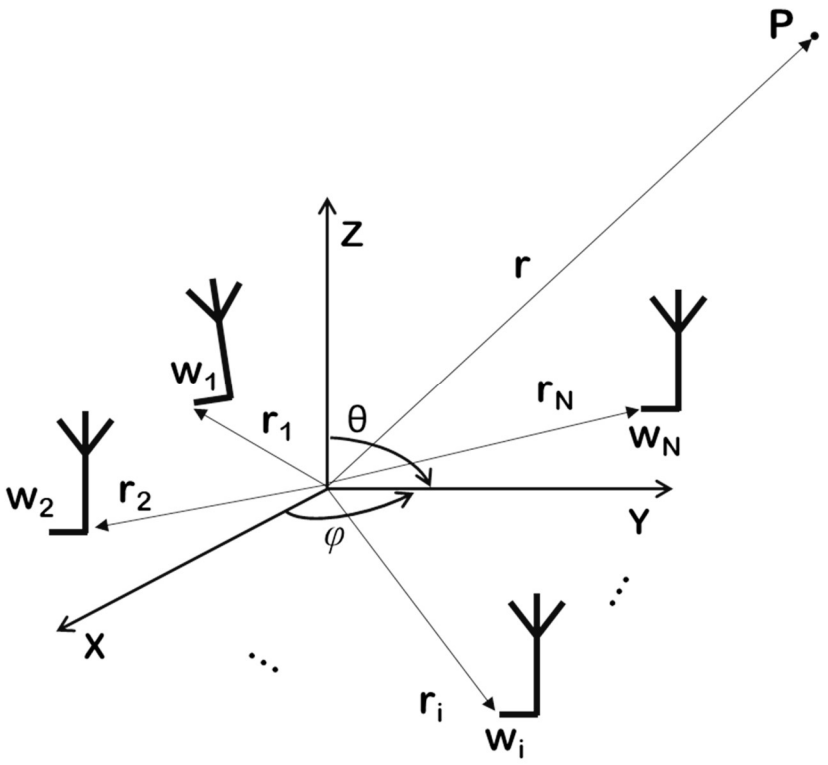

Figure 1-1. An Array of Antennas

The complex vector pattern ($\vec{f}_i(\theta, \varphi)$), which is the normalized complex vector pattern of the *i*th antenna element, determines the radiation pattern and polarization of the *i*th element in

the far field. The far electric field from the *i*th element can be approximated as (1-1) using paraxial approximation.

$$\vec{E}_i(\vec{r}) \approx w_i \vec{f}_i(\theta,\varphi)\frac{e^{-jk_0 r}e^{+jk_0 \hat{r}.\vec{r}_i}}{4\pi r} \tag{1-1}$$

Therefore, based on the superposition principle, the total radiated electric filed ($\vec{E}(\vec{r})$) from an array of antenna elements is the vector sum of the electric fields radiated by each individual antenna element, and is calculated as (1-2).

$$\vec{E}(\vec{r}) = \frac{e^{-jk_0 r}}{4\pi r}\sum_{i=1}^{N} w_i \vec{f}_i(\theta,\varphi)e^{+jk_0 \hat{r}.\vec{r}_i} \tag{1-2}$$

Equation (1-2) is a general term for the far electric field from an array of antenna elements. If the array is planar which means that the array is made of identical antenna elements with the same orientation, the complex vector pattern ($\vec{f}_i(\theta,\varphi)$) would be the same for all the elements as (1-3).

$$\vec{f}_i(\theta,\varphi) = \vec{f}(\theta,\varphi) \qquad \text{for i = 1,…,N} \tag{1-3}$$

In case of a planar array, (1-2) reduces to (1-4).

$$\vec{E}(\vec{r}) = \left[\frac{e^{-jk_0 r}}{4\pi r}\vec{f}(\theta,\varphi)\right]\left[\sum_{i=1}^{N} w_i e^{+jk_0 \hat{r}.\vec{r}_i}\right] \tag{1-4}$$

Equation (1-4), known as the principle of pattern multiplication, consists of a product of two terms. The element pattern and a summation called array factor (AF), which is a function of the array geometry and the elements excitation. As can be seen from equation (1-4), the radiated beam of the antenna array can be steered to any point by changing the excitation phases. This property is known as electronic scanning or electronic beam steering, and such

systems are known as phased-array antennas. Phase shifters or delay lines, and amplifiers are used to adjust the excitation phase and amplitude of each antenna element in order to steer the array's beam towards the desired direction.

PAAs generally comprise four building blocks: antenna elements, splitting\combining network, active or passive beamformers (T/R modules) including phase shifters, low-noise amplifiers (LNA), power amplifiers (PA), and variable gain amplifiers (VGA), and control unit incorporating digital processors. PAAs can be classified into two types: active and passive phased arrays.

A passive phased-array antenna (P-PAA) is one in which the array is fed by a centralized high-power transmit amplifier, with a low-loss power combining/ splitting network and a low-loss phase shifter at every element (Fig. 1-2). High-power centralized transmitters typically utilize klystron vacuum tube amplifiers or travelling wave tube (TWT) amplifiers, both of which are capable of generating output powers of hundred kilowatts at microwave frequencies. Ferrite phase shifters are commonly used in passive arrays since they are capable of handling very high levels of microwave power with very low insertion loss.

A number of shortfalls are associated with passive arrays. First, the centralized transmit power amplifier is a single point of failure. Second, the low-loss combining networks and phase shifters are large, heavy, and difficult to integrate onto airborne or space-based platforms. These factors led to interest in developing active phased-array antenna (A-PAA) systems [4].

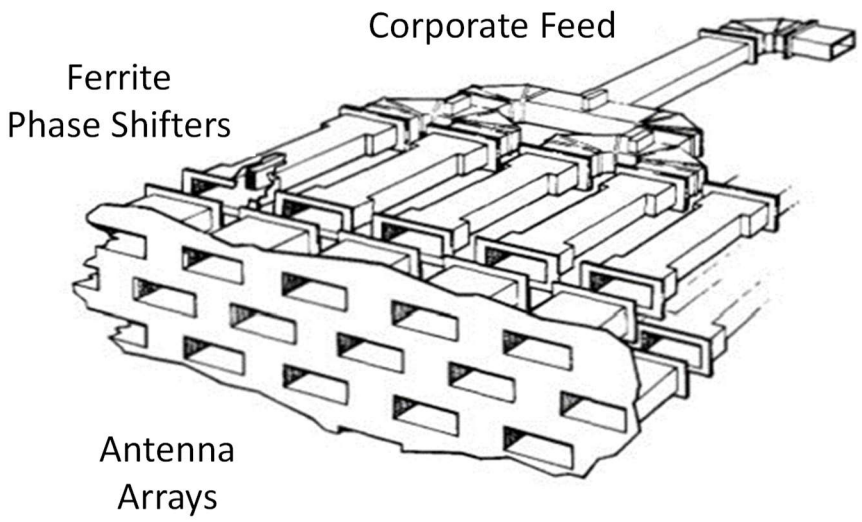

Figure 1-2. Conceptual view of a conventional passive phased array antenna

An A-PAA allows full control of the aperture field (phase and amplitude) since each antenna element excitation is controlled by variable gain power amplifier and phase shifter on the transmitter (Tx) side, and a low-noise amplifier with gain control and phase shifter on the receiver (Rx) side. This approach has the advantage that much lower RF losses are incurred between the transmit amplifiers and free space. This approach also reduces the noise figure of the system and results in improved sensitivity and longer operating distance (range) [4].

Phase shifting can be implemented in different domains in an A-PAA, such as at RF, IF, LO or digital baseband, as depicted in Fig. 1-3 [5].

Phase shifting in the digital domain shown in Fig. 1-3 is often used for beam steering transceivers at low-GHz range, because it often offers several advantages [3]-[5]:

- ✓ High flexibility;
- ✓ High accuracy;

- ✓ Relatively easy to design;
- ✓ Robust against process, temperature and supply voltage variations except for mismatch between paths.

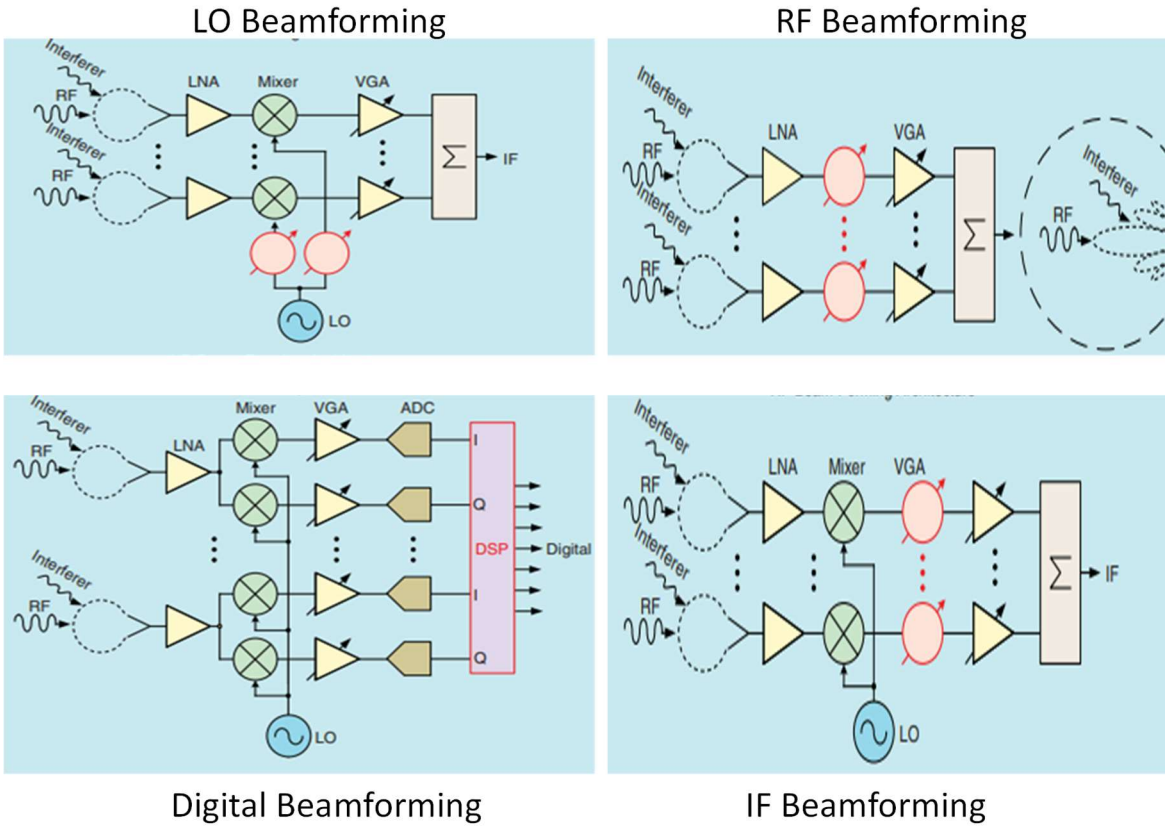

Figure 1-3. Phase shifting implementation in different domains [5]

However, this architecture has several disadvantages at mm-Wave frequencies []:

- ✓ The fractional IF bandwidth of a mm-Wave transceiver is relatively wider making the phase shifting and adding functions challenging to design, and potentially power-hungry.

- ✓ The RF/LO/IF path, including mixers, local oscillators and data converters, has to be implemented for each antenna element independently, generally increasing the cost.
- ✓ Interference cancellation in RX mode is only realizable after the combining function in the digital domain. As a consequence, all circuits before combining need to provide sufficient dynamic range to tolerate these interferers without degrading the signal. The demand for high dynamic range adds more sophistication in the design of RF/IF circuits and data converters, besides increasing the power dissipation of these circuits.

The area occupied by an A-PAA is primarily determined by the area of the $\lambda_0/2$-spaced antenna array. As a result, sharing the antennas among multiple functions has a significant impact on the overall size of the solution. For example, to support half-duplex transmit and receive in both horizontal (H) and vertical (V) polarizations, the phased array needs to support four modes of operation: simultaneous Tx_H and Tx_V, and simultaneous Rx_H and Rx_V [6]. Fig. 1-4 shows the possible configurations for the integration of TX and RX phased-array antennas. Different configurations have their own pros and cons and the selection of a suitable configuration depends on the application, system requirements, cost, and etc.

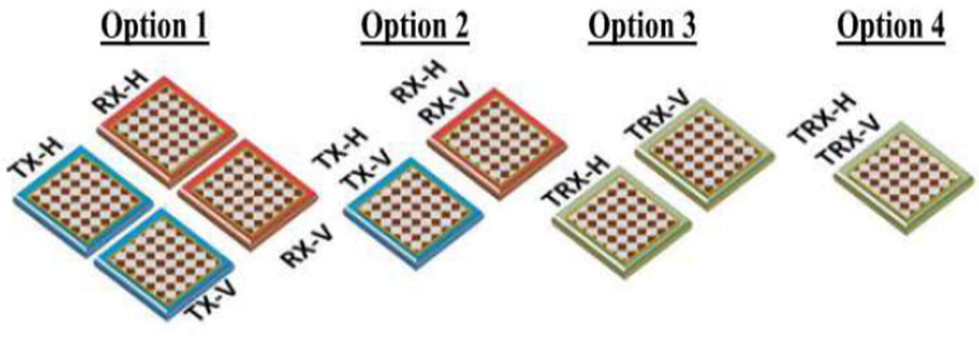

Figure 1-4. Possible configurations for the integration of TX and RX phased-array antennas [6]

There are two approaches in constructing large-scale A-PAAs (Fig. 1-5) [4]. The slat approach has the advantage of providing a large surface area for attaching the T/R modules and supporting electronic components. The disadvantage of slat array configuration is that it requires a large number of RF boards and cabling to route the RF, DC, and control signals. An alternative approach to build A-PAA systems is referred to as a tile architecture [4]. In this approach, the array is constructed of layers that are oriented parallel to the face of the array. The antenna elements and RF beamformers are integrated into a single multilayer RF board. This approach has the impact of reducing the area of the RF boards and significantly reduces the number of connectors and cables and as a consequence a remarkable reduction in the cost of overall system. However, the implementation of an A-PAA requires a large number of electronic components, including MMICs, multi-layer RF printed circuit boards (PCB), RF cables and connectors, and cooling system. These components tend to drive the cost of APAA systems.

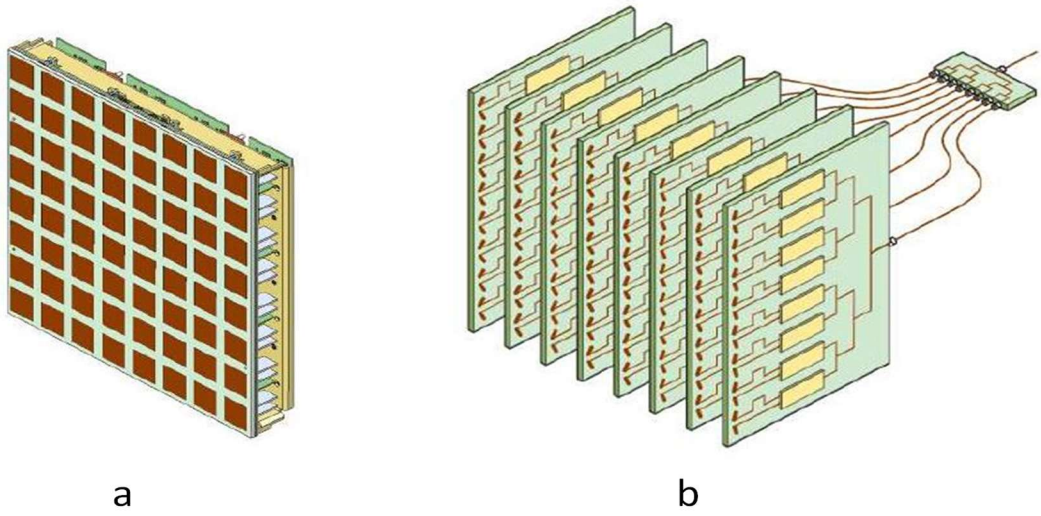

Figure 1-5. (a) Tile and (b) Slat architectures [4]

Despite developments in the defense sector for more than 50 years, A-PAA systems have been mostly absent from affordable, commercial electronics. The high cost is partly because of the discrete implementation of transmit/receive modules where III-V front-end monolithic microwave integrated circuits (MMICs) (GaAs or InP, or both) are assembled together with silicon-based chips used for address decoders, power management, and general digital control such as phase and gain setting and calibration [7]-[8].

A large effort was directed toward the development of compact GaAs-based transmit/receive (T/R) modules with considerable success. The Netherlands/TNO group demonstrated a complete GaAs X-band T/R module with low-loss switches, medium-power amplifiers, very low-noise amplifiers (LNAs), and phase and gain control on a single chip [9]. Other work by Raytheon et al. shows similar performance and with a high degree of integration for GaAs MMICs. Although this is a step in the right direction, it is not enough to greatly reduce the cost of phased arrays, because each T/R module still requires independent silicon control chips, and also, it is not possible to integrate four to eight GaAs T/R modules on the same chip with high yield.

Important breakthrough came exactly a century after the first experiments, when silicon-based phased arrays began to be developed, beginning with the work at the California Institute of Technology (Caltech), Pasadena, using Silicon-Germanium (SiGe) bipolar CMOS (BiCMOS) [10] and Si CMOS technology [11].

Si-based technologies (Si-CMOS and SiGe-BiCMOS) are inexpensive and mass producible and, in conjunction with parallel developments in multilayer antenna-in-package (AiP) technology (Fig. 1-6) [12], make low-cost, low-power phased arrays possible. Significant research on Si-based mm-Wave phased arrays has resulted in improved performance, increased complexity, and forays into sub-mm-wave and terahertz frequencies [13]. Particularly, the

development of standards for 60-GHz communication led to research and commercial development of phased-array integrated circuits (ICs) on silicon [14]–[15].

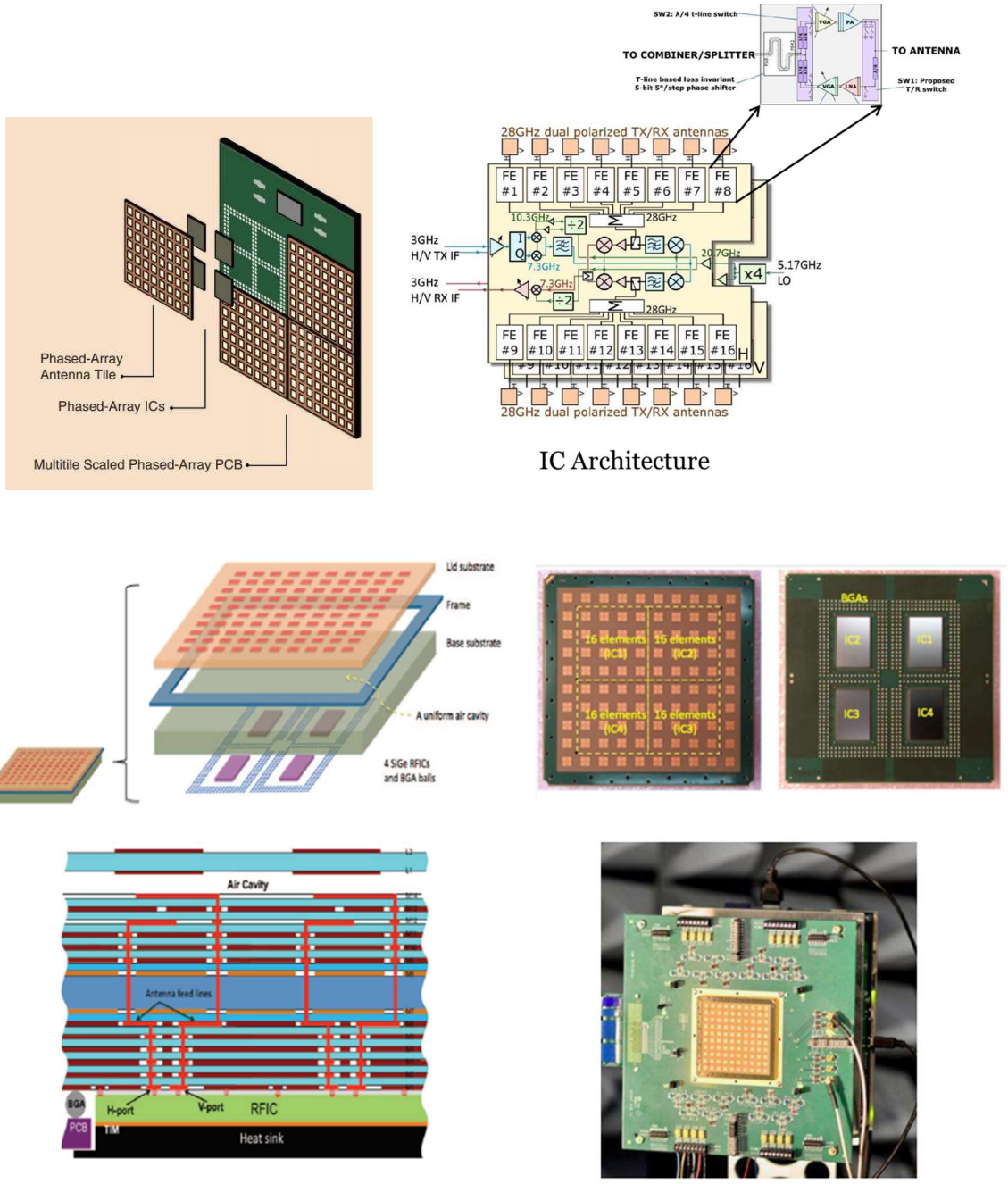

Figure 1-6. Active phased-array antenna system developed at IBM [6], [12]

It is worth mentioning that silicon transistors cannot compete with III-V compounds (GaAs, InP, GaN) for low-noise performance, especially above 8 GHz. Also, in terms of RF power generation, GaAs or GaN transistors can provide higher output powers with high power-added efficiency. However, silicon is better than III-V compounds in terms of integration density, yield, and functionality on a single chip. More recently, there has been an increasing focus on the design of phased arrays with more and more antennas with good reason.

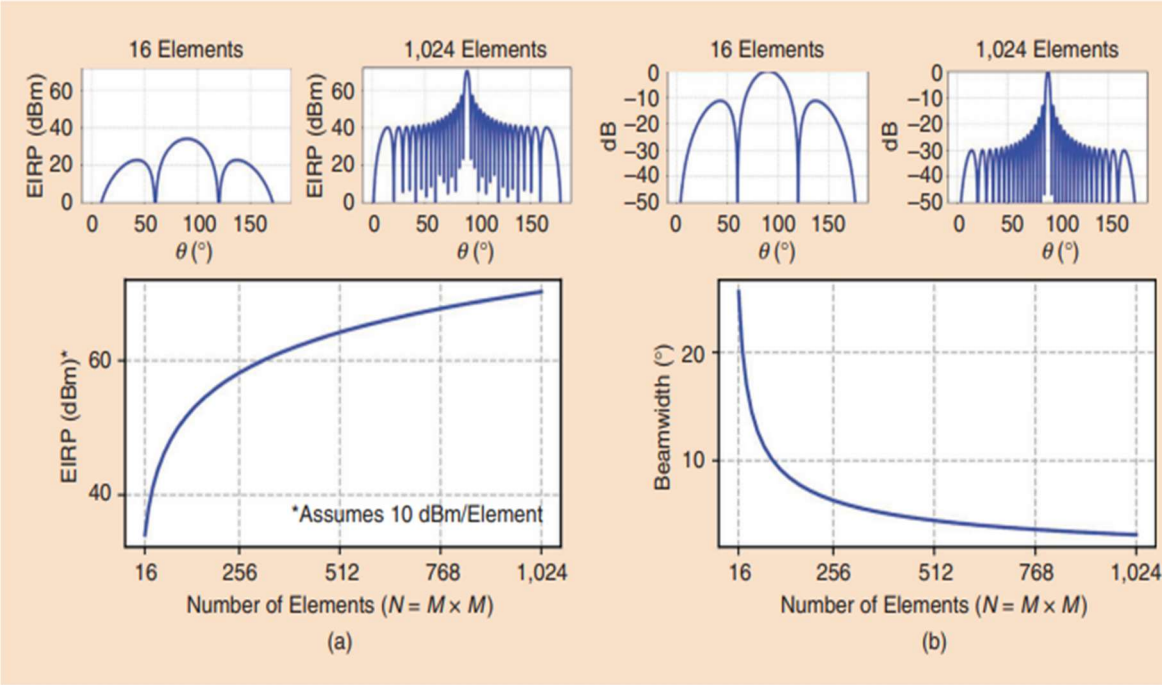

Figure 1-7. (a) The EIRP grows as N^2 while (b) the beamwidth reduces as N versus the number of phased-array elements in a square array, N = M × M, with an antenna spacing of $\lambda_0/2$ [12]

As shown in Fig. 1-7, there is a large (N^2) improvement in the effective isotropic radiated power (EIRP) in a phased-array antenna with N elements [12]. In effect, a phased array provides a very efficient way to combine power in space. In an RX phased-array, the signal-to-noise ratio (SNR) improves by capturing signals from an aperture that is N times larger. The improved EIRP and SNR of large phased arrays effectively translate to an improvement in link

range. For example, while a typical 64-element, 94-GHz Si-based phased array can cover only tens of meters, a 1,024-element Si-based phased array is capable of providing a reliable link at >10 km [16]. The link performance enhancement resolves the shortfall of available output power of Si-based millimeter wave power amplifiers compared to their III-V counterparts commonly used by the military for defense applications. In fact, the link range enhancement using large-scale phased arrays makes it possible to realize long-range Si-based mm-wave radios at the price of increasing the complexity, cost, and size of the system.

1.2 Thesis Objective:

The ever-increasing data rates for wireless technologies along with the service mobility has directed the interests toward aiming at broadband mobile Satellite Communication (SatCom) links. Several services could be provided to passengers as well as to operators of transport platforms like airplanes, trains or ship. Ka-band services and transponders are based on a bi-directional SatCom link at two different frequency bands: uplink from 29.5 GHz to 30.8 GHz and downlink from 19.7 GHz to 21 GHz. The array system needs therefore to have dual band functionalities. This operational frequency band has been selected due to the rising number of available Ka-band transponders in orbit and of new services in Ka-band. A scalable antenna architecture is used to ease its extension to systems of larger dimensions. Furthermore, it is very difficult for such large and complex boards to conform over curved surfaces—this is crucial requirement when developing a communication system that will be deployed on moving terminals (e.g., airplanes, cars, trains, and ships). A low-cost, low-profile antenna system with high RF performance is necessary for such applications. Besides, due to the mobility of the platforms, electronic control of the antenna beam must be realized by the system. Planar large-scale active electronically scanned arrays (AESA) are able to provide the requirements needed for a mobile user terminal [79]. A modular and scalable AESA eases the

complexity of the system besides providing the feasibility of implementing large-scale AESA over conformal geometries [78]. The building block of a modular and scalable AESA is an active phased-array antenna with limited number of antenna elements. Si-based (Si-CMOS and SiGe-BiCMOS) multi-channel beamformers in conjunction with parallel developments in multilayer antenna-in-package (AiP) technology makes a low-cost and low-profile active phased-array antenna realizable [81]-[83]. Antenna-in-package (AiP) technology, in which there is an antenna (or antennas) with a transceiver die (or dies) in a standard surface-mounted device, represents an important antenna and packaging technology achievement in recent years. AiP technology has been widely adopted by chipmakers for 60-GHz radios and gesture radars. It has also found applications in 77-GHz automotive radars, 94 GHz phased arrays, 122-GHz imaging sensors, and 300-GHz wireless links. It is believed that AiP technology will also provide elegant antenna and packaging solutions to the fifth generation and beyond operating in the lower millimeter-wave (mm-Wave) bands. Thus, one can conclude that AiP technology has emerged as the mainstream antenna and packaging technology for various mm-Wave applications [81].

This research covers the design and implementation of a 4×4 modular and scalable active transmit phased-array antenna-in-package (AiP) with polarization control for SATCOM-on-the-Move (SOTM) user terminal are presented. In this thesis, also the system analysis and design aspects of a highly-efficient planar bi-directional 4×4 passive phased-array antenna module at Ka-Band are presented. Hybrid approach that combines active and passive PAA architectures is an alternative solution in lowering the cost and complexity of A-PAA systems [50]. In this approach, the active components (PA, LNA, etc.) are shared between groups of antenna elements which form subarrays, where the amplitude control is executable. Hybrid architecture could reduce the cost and complexity of the system if the number of active devices

is reduced. However, passive beamformers with low insertion loss and compact size have to be developed.

1.3 Thesis Outline

In this thesis, two different architectures for phased-array AiP are presented. The first architecture is a 4×4 dual-polarized active transmit phased-array AiP at Ka-band. The second architecture is a 4×4 bi-directional antenna array with integrated passive beamformer with left-handed circular polarization (LHCP) radiation.

A silicon-based dual-polarized active transmit phased-array AiP is able to realize any kind of polarization including linear and circular polarization besides providing relatively high effective isotropic radiated power (EIRP). The proposed active AiP is modular and scalable and is able to be the unit cell for a large-scale phased array antenna system. It consists of 16 dual-polarized cavity-backed patch antennas, four 8-channel active beamformers, and a 4-way splitter network. The proposed AiP provides 42 dB of active gain at the boresight. The EIRP of the current module is 41 dBm at the 1-dB compression point of the active beamformer chips and it consumes 2.6 W when the system radiates left-handed circular polarization. Calibration and radiation pattern measurement of the system is also discussed and the measurement results for a case of left-handed circularly polarized (LHCP) radiation is presented.

Hybrid approach that combines active and passive PAA architectures is an alternative solution in lowering the cost and complexity of active PAA systems. The design and implementation aspects of a 4×4 antenna array with integrated passive beamformer for low-cost and efficient millimeter wave applications is presented. The phase shifter's operational principle and actuation mechanism are discussed in detail. Slow-wave structure is employed to shrink the size of the phase shifter. The simulation and measurement results of the phase

shifter are presented. Measurement results show the maximum insertion loss of 2.2 dB in all the tuning states and the insertion loss variation is 1.2 dB. Also, it provides 380º of the phase tuning range in a compact footprint area of 2.4 mm × 3 mm. 2D P-PAA is designed, simulated and measured over the operating band. Measurement results show the antenna‘s main beam can be steered over an angular range of ±30º in both elevation and azimuth planes.. The operating frequency bandwidth of the system ranges from 28-30 GHz. The antenna’s main characteristics, such as radiation pattern, directivity, efficiency, and reflection coefficient are measured and presented.

Chapter 2- A Modular and Scalable Active Transmit Phased-Array Antenna-in-Package for Ka-Band Satellite-on-the-Move (SOTM) User Terminal

2.1 Introduction

The ever-increasing data rates for wireless technologies along with the service mobility has directed the interests toward aiming at broadband mobile Satellite Communication (SatCom) links. Several services could be provided to passengers as well as to operators of transport platforms like airplanes, trains or ships as shown in Fig. 2-1.

Ka-band services and transponders are based on a bi-directional SatCom link at two different frequency bands: uplink from 29:5 GHz to 30:8 GHz and downlink from 19:7 GHz to 21 GHz. The array system needs therefore to have dual band functionalities. This operational frequency band has been selected due to the rising number of available Ka-band transponders in orbit and of new services in Ka-band.

A scalable antenna architecture is used to ease its extension to systems of larger dimensions. Furthermore, it is very difficult for such large and complex boards to conform over curved surfaces—this is crucial requirement when developing a communication system that will be deployed on moving terminals (e.g., airplanes, cars, trains, and ships) with minimal aerodynamic drag. A low-cost, low-profile antenna system with high RF performance is necessary for such applications. Besides, due to the mobility of the platforms, electronic control of the antenna beam must be realized by the system.

Planar large-scale active electronically scanned arrays (AESA) are able to provide the requirements needed for a mobile user terminal [79]. A modular and scalable AESA, as shown

in Fig. 2-2, eases the complexity of the system besides providing the feasibility of implementing large-scale AESA over conformal geometries [78].

The building block of a modular and scalable AESA is an active phased-array antenna with limited number of antenna elements. Si-based (Si-CMOS and SiGe-BiCMOS) multi-channel beamformers in conjunction with parallel developments in multilayer antenna-in-package (AiP) technology makes a low-cost and low-profile active phased-array antenna realizable [81]-[83].

Antenna-in-package (AiP) technology, in which there is an antenna (or antennas) with a transceiver die (or dies) in a standard surface-mounted device, represents an important antenna and packaging technology achievement in recent years. AiP technology has been widely adopted by chipmakers for 60-GHz radios and gesture radars. It has also found applications in 77-GHz automotive radars, 94 GHz phased arrays, 122-GHz imaging sensors, and 300-GHz wireless links. It is believed that AiP technology will also provide elegant antenna and packaging solutions to the fifth generation and beyond operating in the lower millimeter-wave (mm-Wave) bands. Thus, one can conclude that AiP technology has emerged as the mainstream antenna and packaging technology for various mm-Wave applications [81].

This thesis presents a 4×4 dual-polarized active transmit phased-array antenna-in-package (AiP) for SATCOM-on-the-Move (SOTM) user terminal. This work demonstrates the evaluation setup of a phased-array AiP unit cell before being mounted permanently on the backplane of a large-scale AESA. In Section 2-2, the architecture, build-up and design of the proposed AiP is presented. In Section 2-3, the solderless test fixture for the measurement of the AiP performance is discussed. Then over-the-air (OTA) test measurement results are presented.

Figure 2-1. SatCom link realization on different mobile platforms

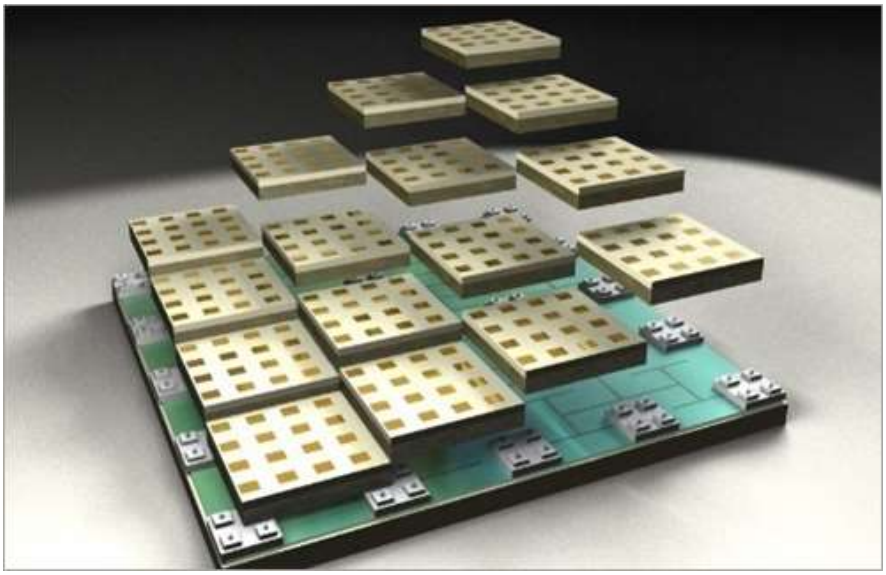

Figure 2-2. Large-Scale planar AESA realized by AiP unit cells [85]

2.2 Antenna-in-Package Design

2.2.1 Architecture

Fig. 2-3 shows the architecture of the proposed active phased-array antenna in package. It consists of sixteen dual-linearly polarized (Horizontal and Vertical) cavity-backed slot-coupled patch antennas in a square-lattice configuration, four 8-channel transmit RFIC beamformers, a four-way Wilkinson power divider, and a substrate-integrated vertical coaxial line which provides the connection between the AiP and the backplane feeding network. The build-up of the AiP is shown in Fig. 2-4. The stack up comprises 12 metal layers and the dielectric constant of the laminates is ε_r=3 and the loss tangent is tgδ=0.001. Fig. 2-5 shows the fabricated 4×4 phased-array AiP.

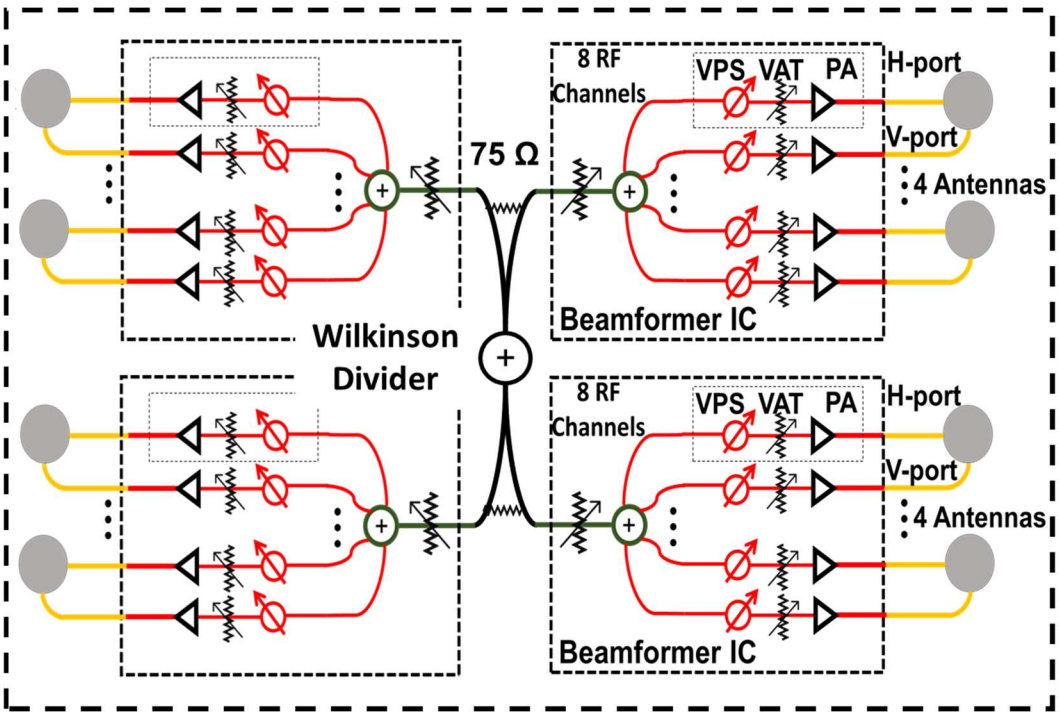

Figure 2-3. The architecture of the proposed AiP

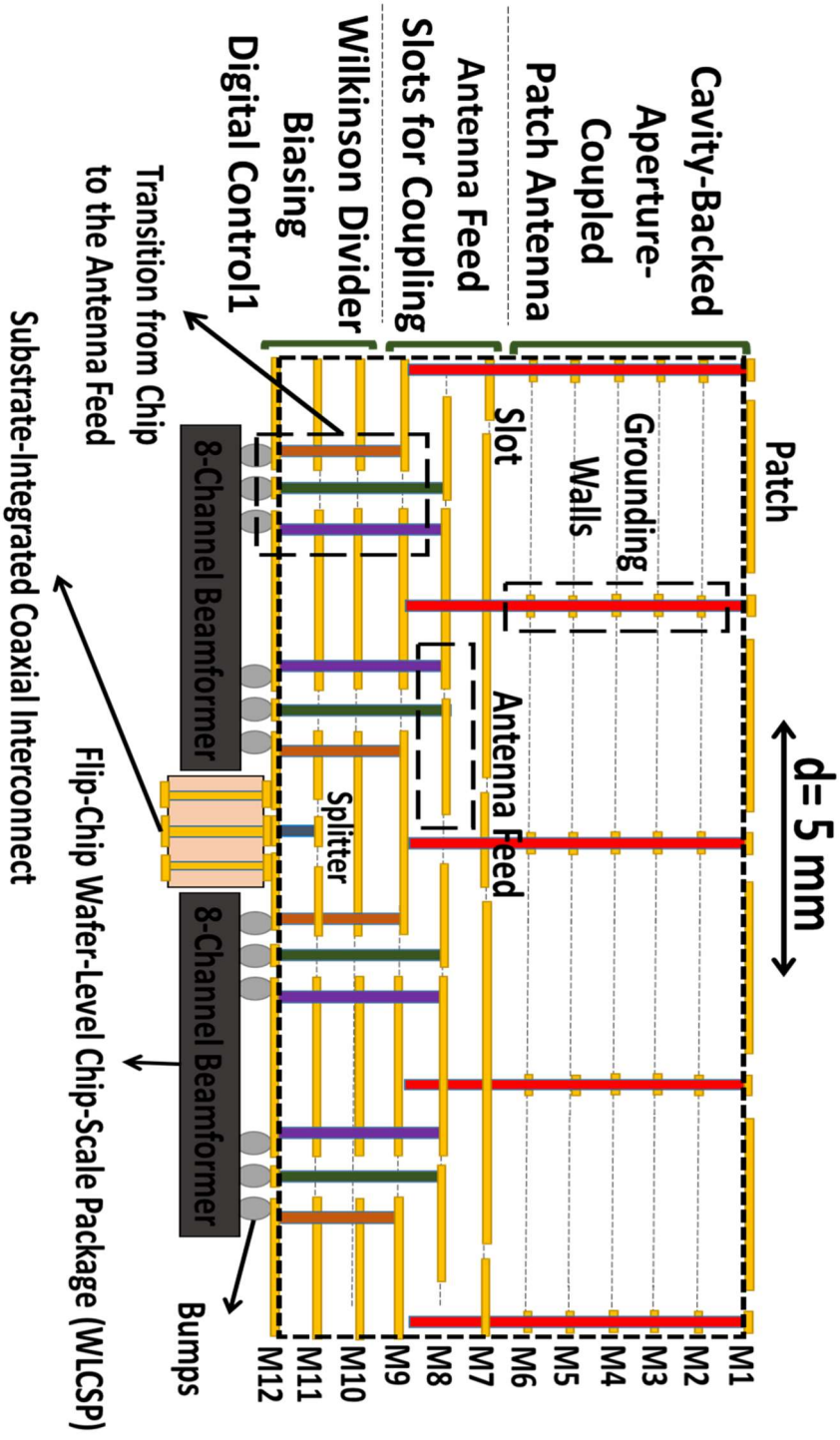

Figure 2-4. The build-up of the AiP

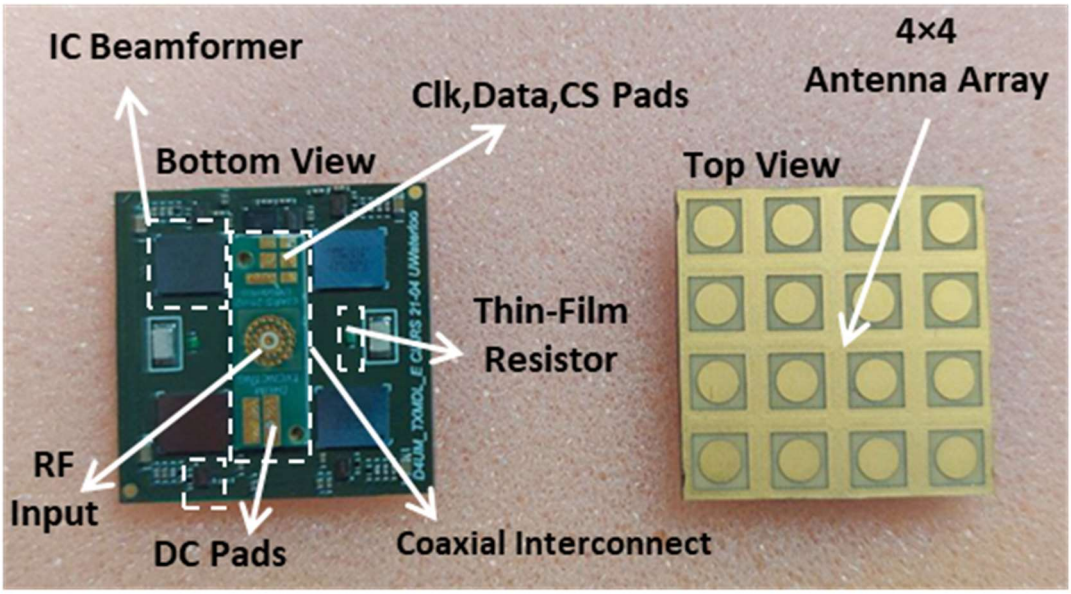

Figure 2-5. Top and Bottom view of the fabricated AiP

2.2.2 Antenna Design

The antenna array consists of sixteen dual-linearly polarized (Horizontal and Vertical) cavity-backed slot-coupled patch antennas in a square-lattice configuration. The cavity-backed design suppresses the excitation of surface modes in the antenna substrate. Dual-linear polarization realizes the polarization control of the radiated field from the antenna system. The element spacing is 5 mm ($0.5\times\lambda_0$ at 30 GHz). A $0.5\lambda_0 \times 0.5\lambda_0$ grid size is chosen for the array and it ensures grating lobe-free scanning. Fig. 2-6 shows the unit cell 3-D model of the planar dual-linearly polarized stacked-patch microstrip antenna.

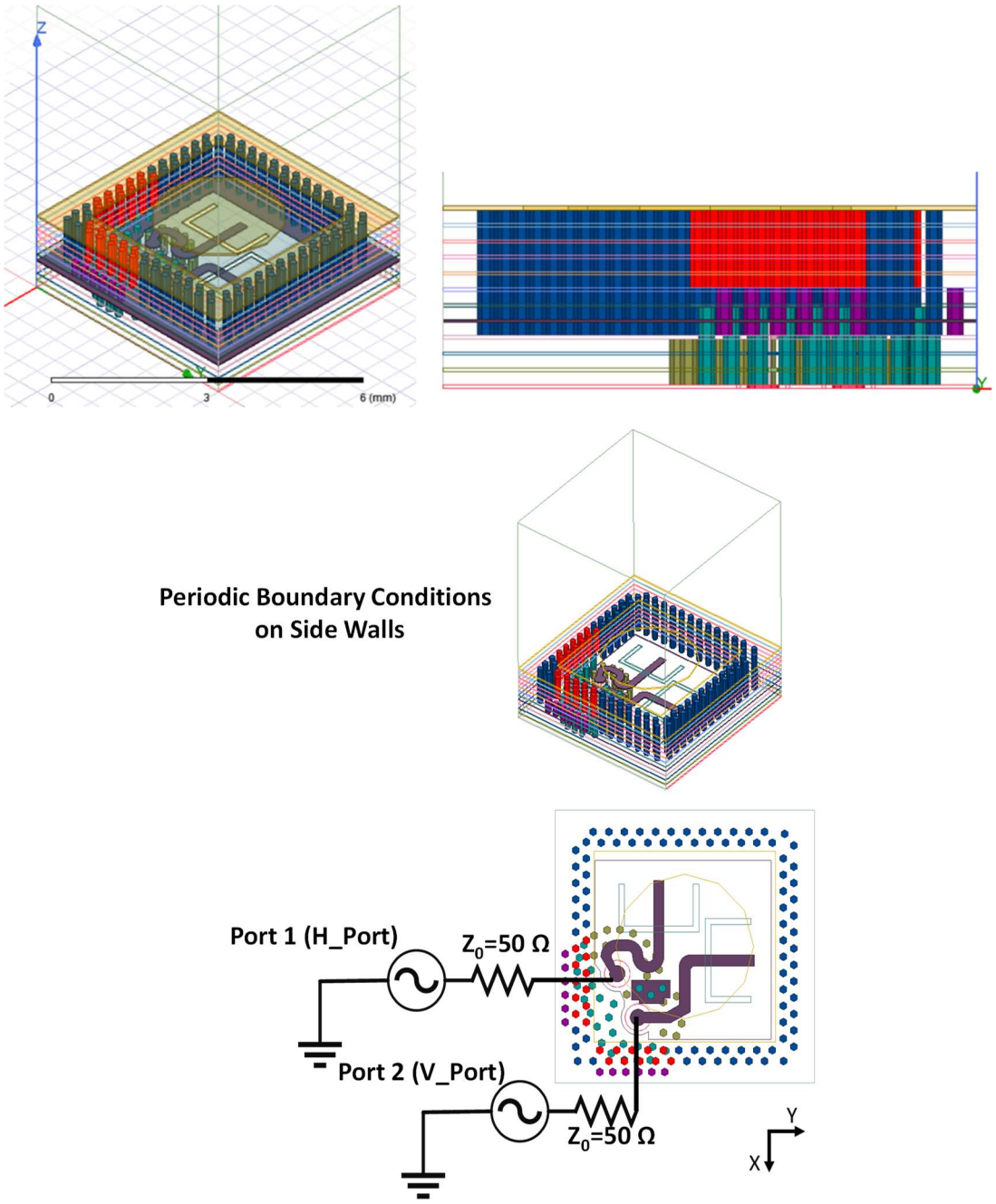

Figure 2-6. The antenna unit cell

The antenna unit cell is simulated under periodic boundary condition using Ansys EDT. This boundary condition realizes boundaries as that of the unit cell in a large-scale phased-array antenna system. Fig. 2-7 shows the EM simulation results of the scattering parameters of the antenna unit cell, as the array scans to 70° in the E-plane of port-1 (H-Port) (X-Z plane) as shown in Fig. 2-7. The antennas are well-matched with S_{11} and S_{22} less than −12 dB and remains less than −6 dB as the array scans in the frequency range of 28-30 GHz. The coupling (S_{21}) between the ports remain below -19 dB for all the scan angles in the frequency range of 28-30 GHz as shown in Fig. 2-7. Fig. 2-8 shows the X-pol discrimination (XPD) of the radiated field from port 1 while port 2 is 50-Ω matched at E-plane of port 1 (X-Z plane) for different scan anlges. The Antenna shows more than 20 dB of XPD for all the scan angles. Also it is shown in Fig. 2-8 that the antenna radiation patterns changes while the array scans.

The orientation of the antenna elements in one quarter of the array is shown in Fig. 2-9. Sequentially rotating the antenna feeds in a 2 × 2 antenna cell significantly decreases the cross-polarization coupling at all scan angles resulting in better XPD by providing rotational symmetry. Besides, this orientation not only reduces the transition from the IC output ports to the antenna ports, but also realizes a symmetrical structure.

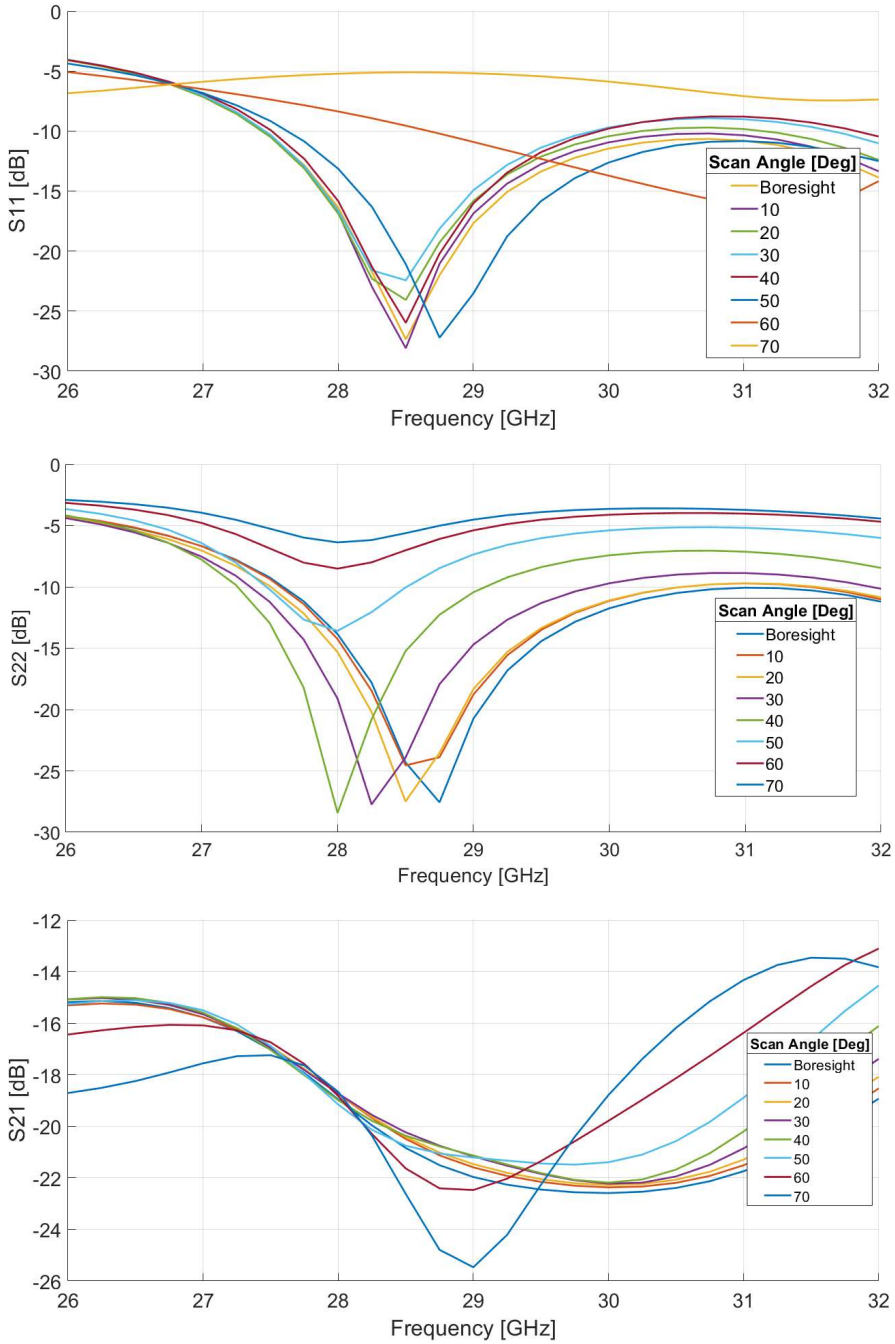

Figure 2-7. The scattering parameters of the antenna unit cell for different scan angles.

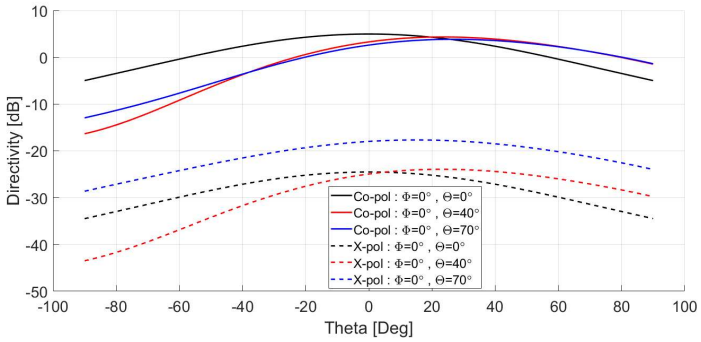

Figure 2-8. The XPD of the radiated field from port 1 while port 2 is 50-Ω matched at E-plane for different scan anlges.

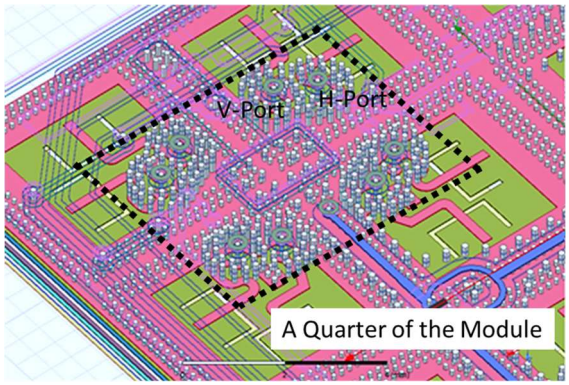

Figure 2-9. The orientation of the antenna elements in a quarter of the AiP.

Fig. 2-10 shows the Co-pol radiation patterns generated by two H and V ports at X-Z plane while both of them are excited by the same phase and amplitude. It shows that although patterns are symmetric at boresight due to the symmetry in the antenna design, the Co-pol radiation patterns of two orthogonal ports (H-port and V-port) differ when the array scans.

This is because the periodic boundary conditions perturb the current distribution on the microstrip patch excited from two ports differently. The difference in the Co-pol radiation patterns must be taken into account while calibrating the phased-array antenna system for different polarizations.

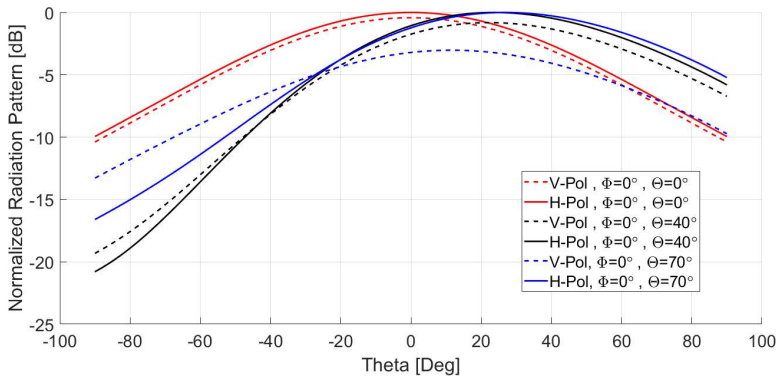

Figure 2-10. The Co-pol normalized radiation patterns of two ports at X-Z plane for different scan angles.

Fig. 2-11 shows the radiation patterns of the 4×4 antenna array for different scan angles up to 70° when the array radiates right-handed circular polarization. The interpolation of the peaks of the radiation patterns at different scan angles behaves as $Cos^{1.5}(\theta)$ which shows the scan loss of the 4×4 antenna array.

The scan loss is due to the decrease in the aperture area as the beam scans, and the radiation pattern of the single-element antenna as well as the mutual coupling between the antenna elements.

As shown in Fig. 2-11, the scan pointing accuracy is not as accurate at large scan angles as that of small scan angles. The main reason is the small size of the array. For a small array, the radiation pattern is not only dominated by the array factor, but also the single-element radiation pattern is taken in to account as in (1-4).

Fig 2-12 shows the radiation pattern of the 4×4 antenna while the array scans toward 60°. Although the array factor has a peak at 60°, the peak of the radiation pattern has a peak at a smaller scan angle (< 60°) which is mainly due to the impact of the single-element radiation pattern in the array radiation pattern.

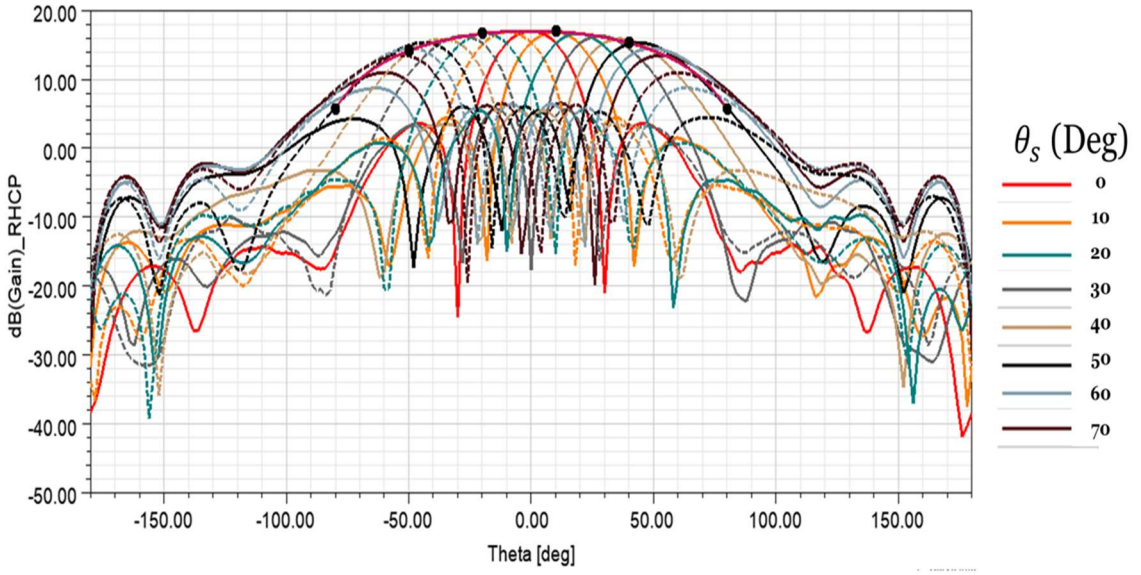

(a)

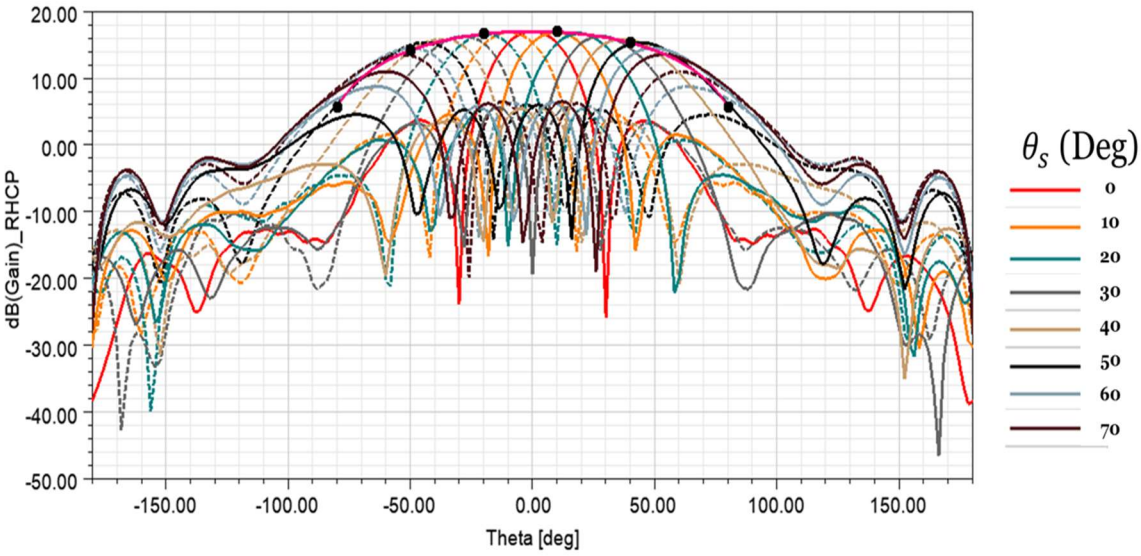

(b)

Figure 2-11. The Co-pol radiation patterns of the 4×4 antenna array for different scan angles when the array radiates right-handed circular polarization. (a) X-Z plane scanning (b) Y-Z plane scanning.

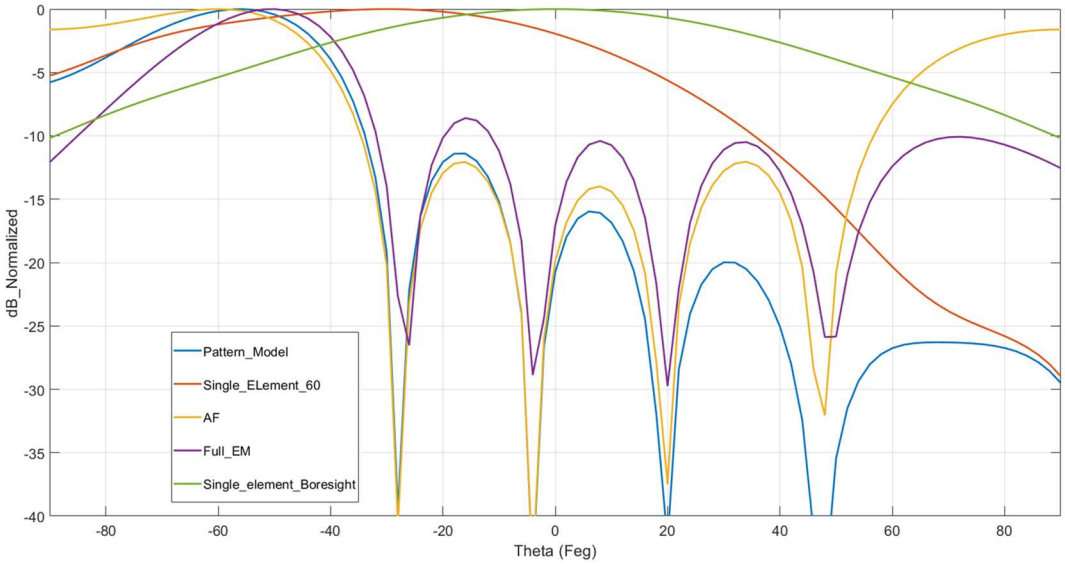

Figure 2-12. The radiation pattern of the 4×4 antenna while the array scans toward 60°.

2.2.3 Beamformer IC Characteristics

The beamformer Tx RFIC is a commercialized Ka-band beamformer. The beamformer chip has eight RF channels and one common RF input as shown in Fig. 2-13.

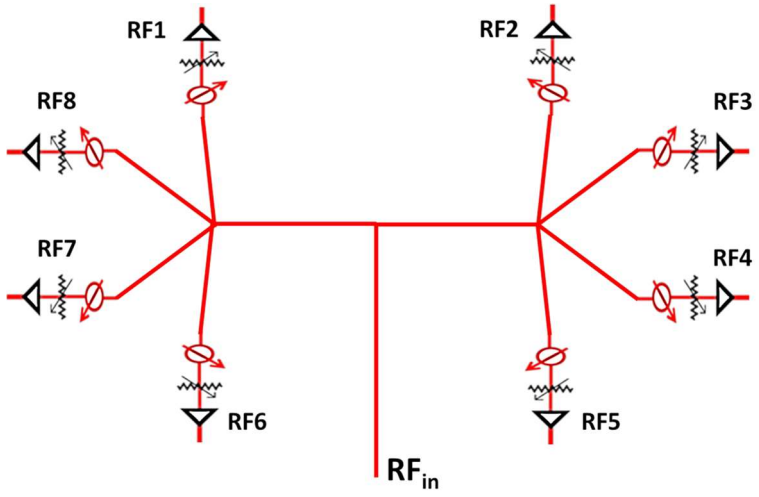

Figure 2-13. Beamformer evaluation board

Each RF channel comprises a variable phase shifter (VPS), a variable attenuator (VAT), and a power amplifier (PA). The chip architecture allows for a single beam with polarization diversity. It has 15.5 dB dynamic range (5 bits) for the gain control with the resolution of 0.5 dB, a 6-bit (64 states) phase shifter with rms phase and amplitude errors of < 4.5° and < 0.8 dB at 27.5–30 GHz. The power amplifier (PA) 1-dB compression point at the output (OP1dB) is ~10 dBm at 29 GHz. The measured active gain of each RF port is 22 dB at 29 GHz where active gain is the gain between the common input port of the beamformer IC and one of the output ports. Table I summarizes the specification of the beamformer IC.

TABLE I
BEAMFORMER IC CHARACTERISTICS

Beamformer IC Characteristics:	
Frequency of Operation	**27.5-30.5 GHz**
Active Gain*	**21 dB**
Amplitude Control (5 bit, 0.5 dB Resolution)	**0-15.5 dB Attenuation**
Phase Control (6 bit, 5.625 ° Resolution)	**0-360° [Deg]**
Output 1dB Compression Point (OP1dB)	**9~10 dBm**
Biasing	**1.2 [V] (Drawing Current: 390 mA)****

* Active gain is the gain between the common input port of the beamformer IC and one of the output ports.

** Quiescent current consumption (no RF signal is injected.)

2.2.4 Splitter Network

The splitter network is a 4-way Wilkinson divider. The Wilkinson divider uses strip line technology and is embedded in layers M10-M12. The resistors used in the structure of the Wilkinson divider are 75-Ω surface-mount high frequency thin-film resistors. The splitter network structure and its prototype is shown in Fig. 2-14.

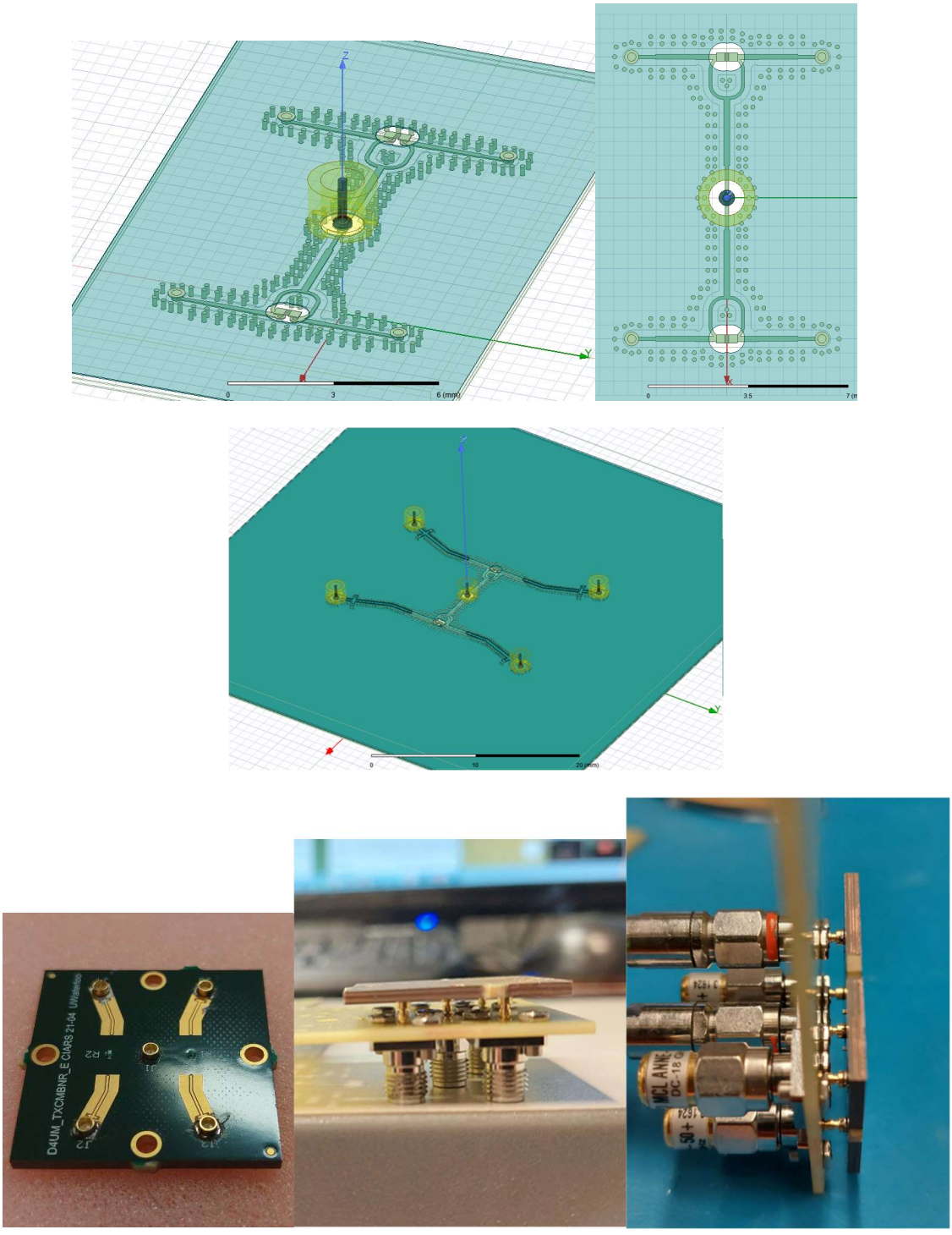

Figure 2-14. The splitter network design and evaluation board

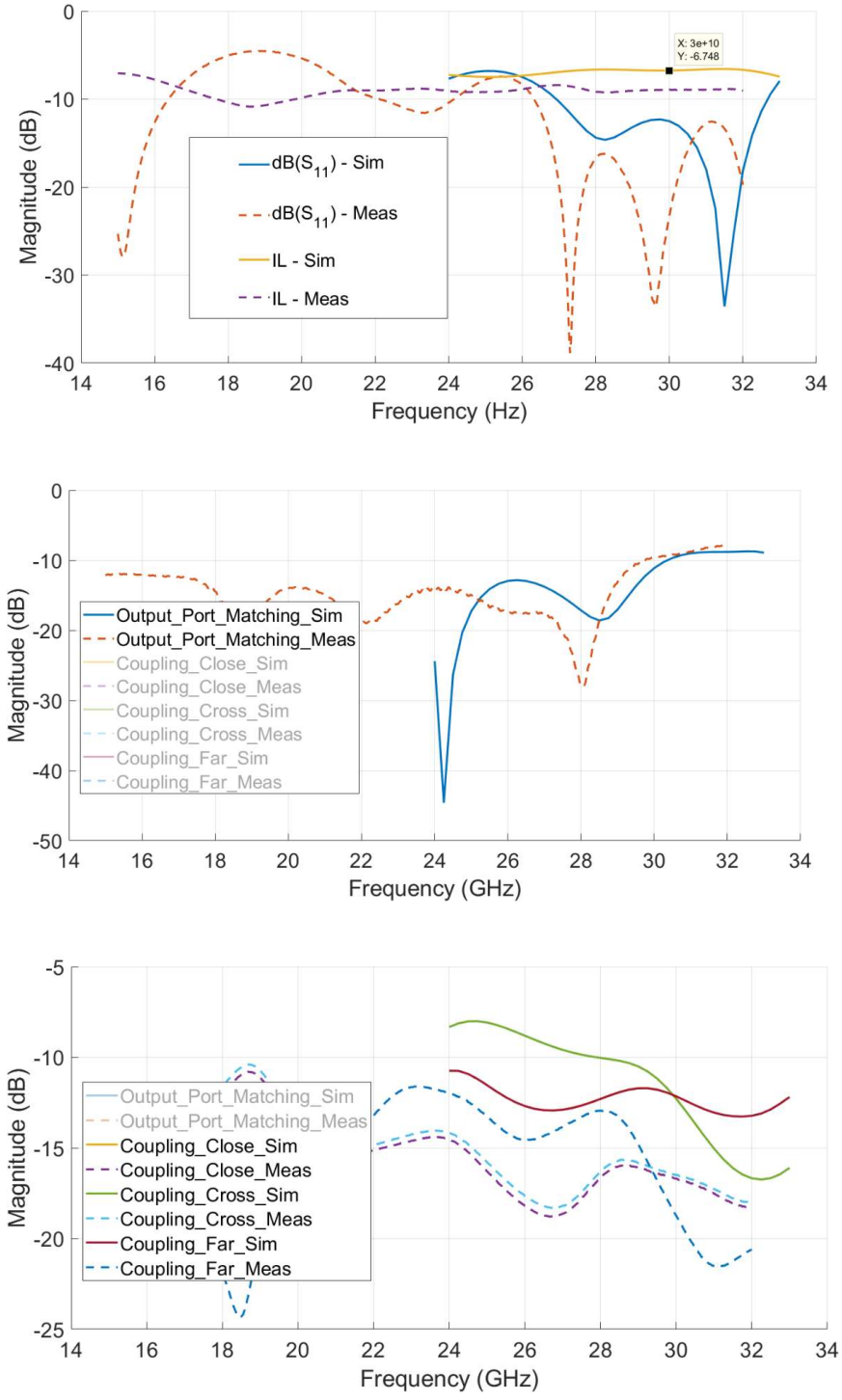

Figure 2-15. The simulation and measurement results of the splitter network

The fabricated splitter network is tested using the test fixture shown in Fig. 2-14. The measurement results of the splitter's evaluation board shows 1.6 dB of loss and more than 15 dB of isolation between the output ports over the frequency range of 27-30 GHz as shown in Fig. 2-15. As shown in Fig.2-15, there is discrepancy in the simulation and measurement results of the insertion loss. The measurement results of the thru-reflection-load (TRL) calibration kit (Fig. 2-16) shows that the attenuation constant of the stripline is 0.52 dB/cm while that of the simulation is 0.32 dB/cm (Fig. 2-17).

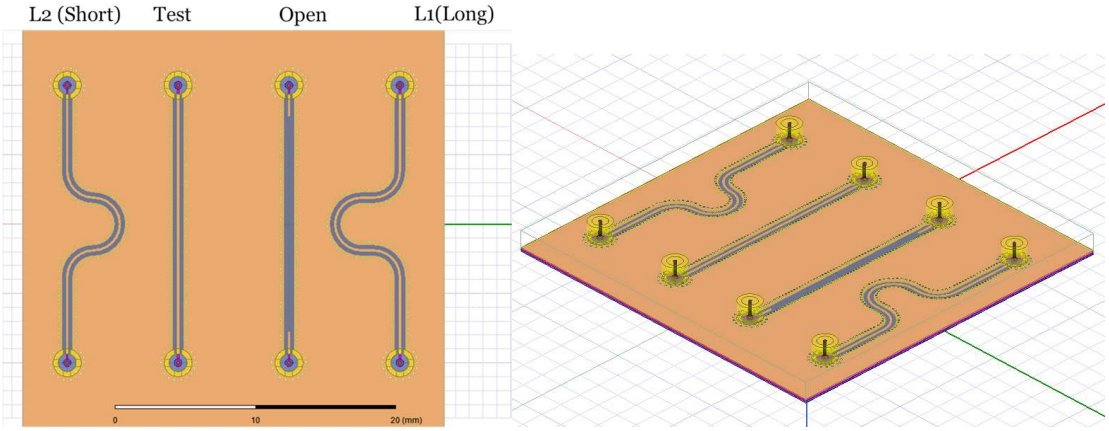

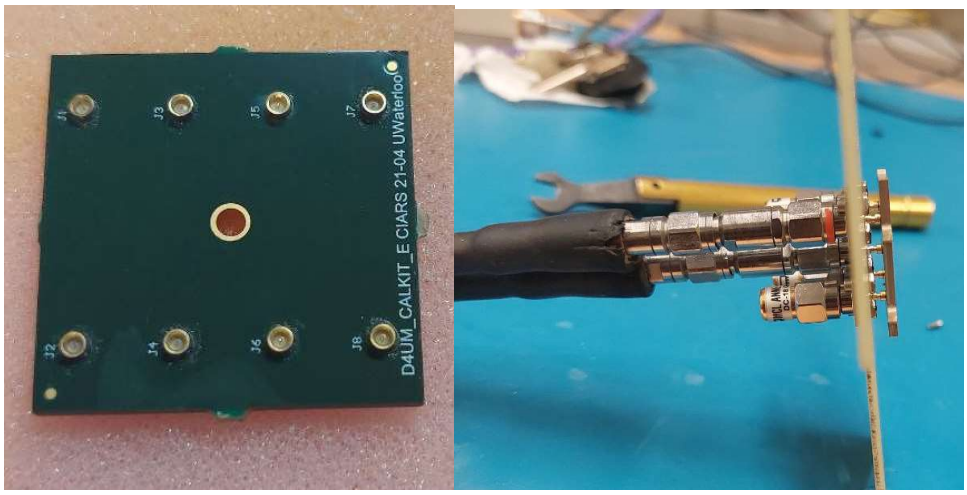

Figure 2-16. The orientation of the antenna elements in the system

The first reason could be because of the inaccuracy in the electrical properties of the laminate. The second reason is that the surface roughness of the metal layers is not taken into consideration in the simulation.

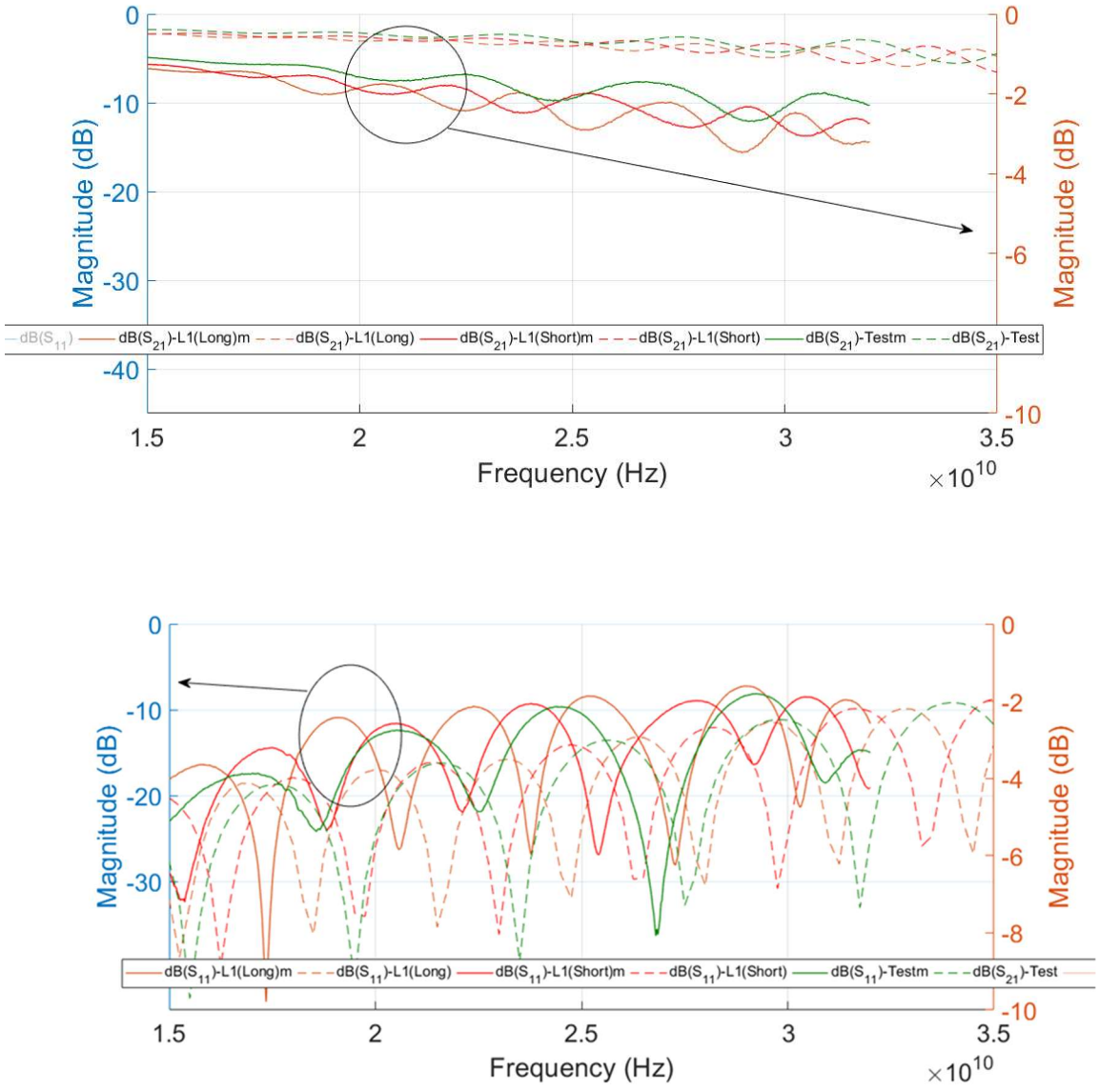

Figure 2-17. The measurement results of the TRL calibration kit.

2.2.5 Substrate-Integrated Vertical Coaxial Line

Substrate-integrated vertical coaxial line (SIVCL) provides the connection between the AiP and the backplane which would be a feeding network for providing the input power to the AiP as shown in Fig. 2-4. The structure of the SIVCL is shown in Fig. 2-18. The design parameters of the SIVCL are specified in such away that the input and output ports provide the proper matching for 50 Ω terminations. The fabricated SIVCL is tested using the test fixtures shown in Fig. 2-19. The measurement results of the fabricated SIVCL shows the average 0.6 dB of insertion at 30 GHz as shown in Fig. 2-20 besides providing high return loss of more than 20 dB.

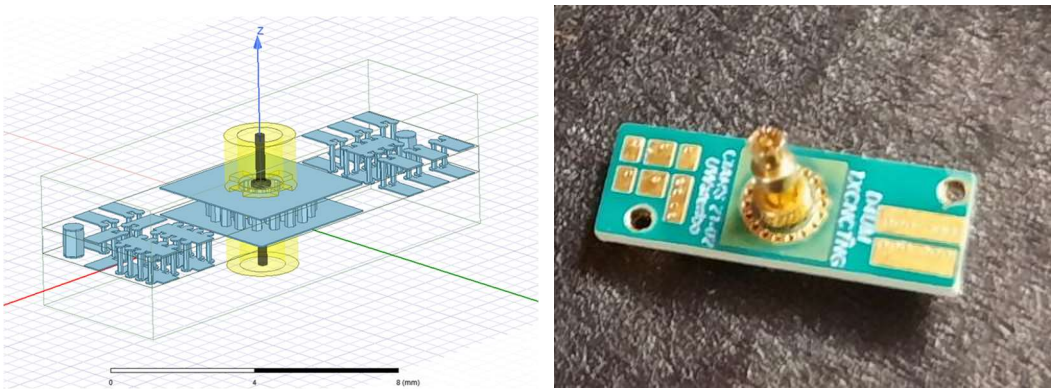

Figure 2-18. The structure of Substrate-integrated vertical coaxial line (SIVCL)

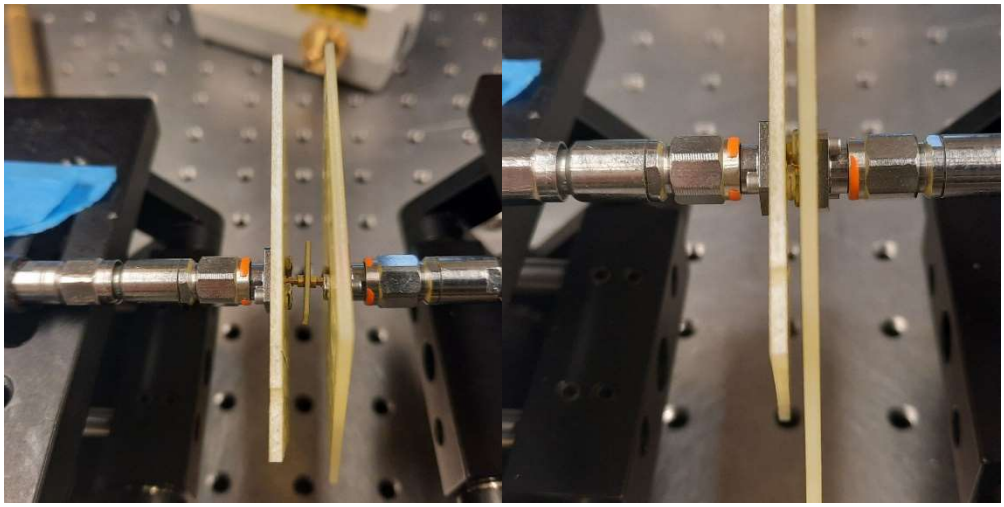

Figure 2-19. The test fixtures for evaluation of the Substrate-integrated vertical coaxial line (SIVCL)

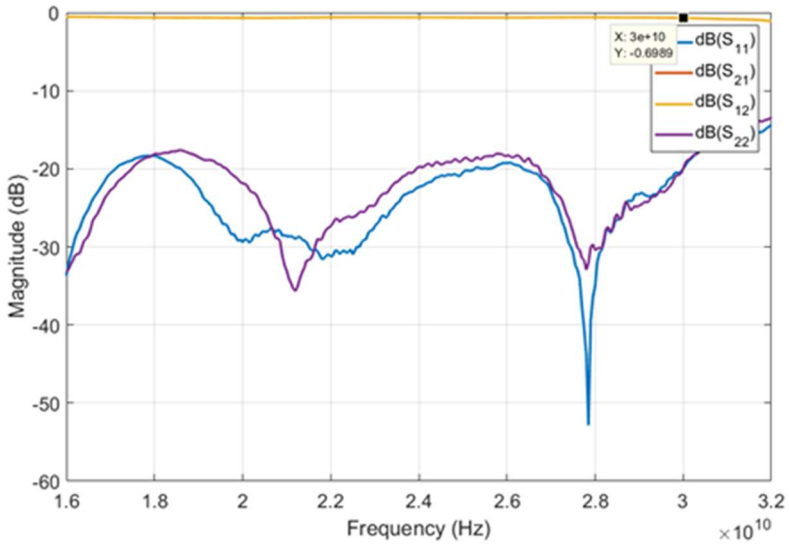

Figure 2-20. The measurement results of the fabricated SIVCL

2.3 Over-the-Air (OTA) Measurement Results

A mechanical test fixture with solderless RF connection mechanism is developed for testing of the AiP as shown in Fig. 2-21. It demonstrates the evaluation setup of a phased-array AiP unit cell before being mounted permanently on the backplane of a large-scale AESA.

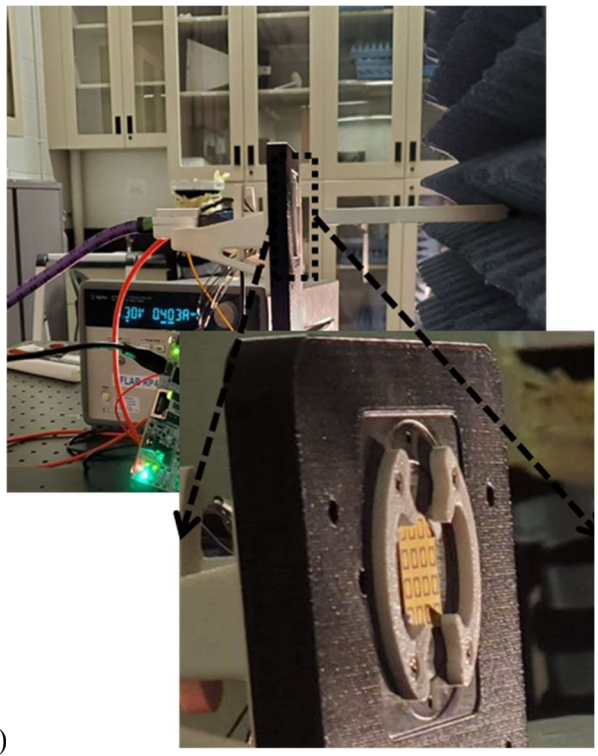

(a)

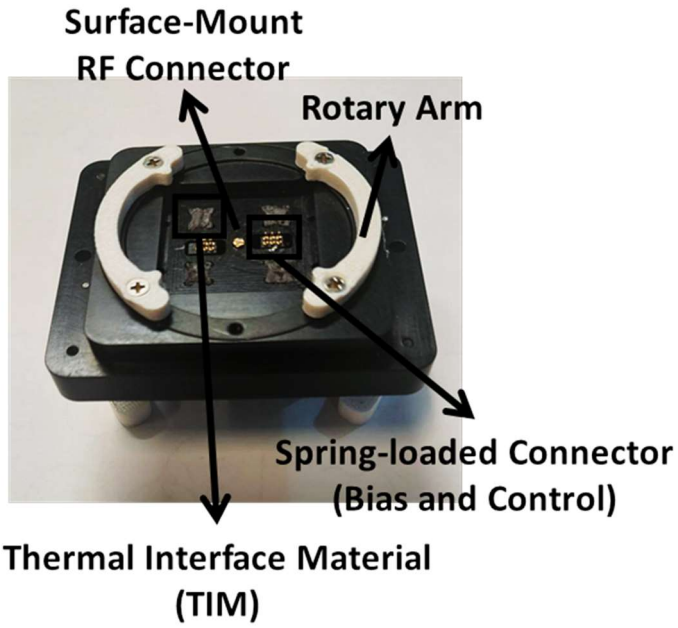

(b)

Figure 2-21. (a) The fixture for mounting the AiP. (b) The components of the fixture.

It consists of a surface-mount mini coaxial connector which is connected to an SMA adaptor from the back. Spring-loaded connectors provide the biasing voltage and digital control signals. The rotary arms keep the AiP in touch with the mini connector as shown in Fig. 2-21. The test setup is shown in Fig. 2-22. An open waveguide probe is used for measuring the near-field of the antenna system. Thermal interface materials (TIM) are embedded inside the fixture in such a way that they are in contact with the surface of the beamformer IC chips after mounting the AiP in the fixture. They enhance the thermal coupling between the chip as the source of heat and the heat sinks at the back of the TIMs.

2.3.1 Beamformers Functionality Evaluation

The phase and amplitude control of each port of the antenna elements are evaluated by placing the probe in front of each specific antenna element and measuring the transmission coefficients (TC) for all the phase and amplitude states.

Fig. 2-24 and Fig. 2-25 show the differential phase shifts for all the phase states with respect to the phase state '0' for all the H-pols (Ports with even numbers in Fig. 2-23).

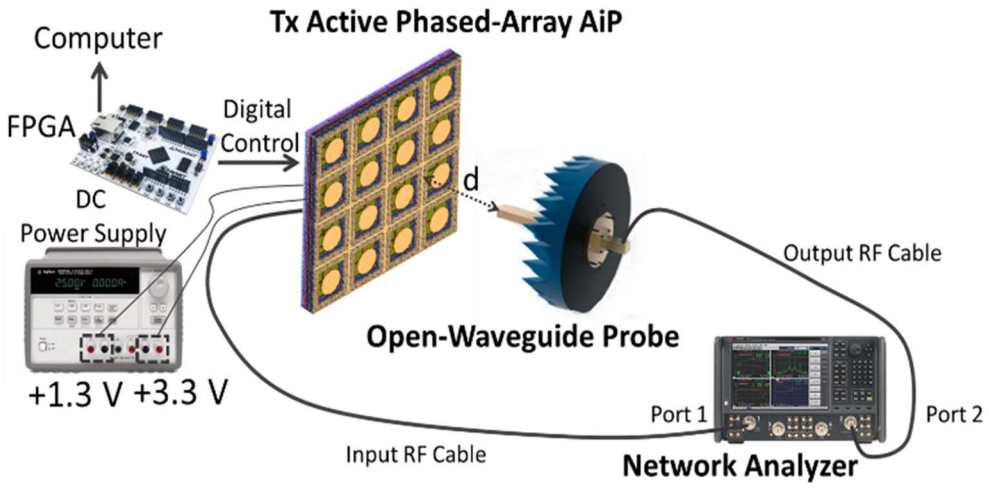

Figure 2-22. Over-the-Air (OTA) measurement setup.

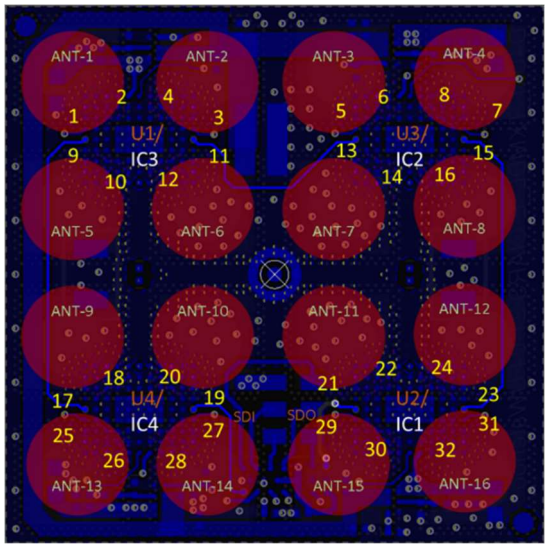

Figure 2-23. Numbering of the antenna ports in the AiP

The measured rms phase shit error is < 6.5° for all the ports. Fig. 2-26 shows the Co-pol and X-pol TCs for all the amplitude states for H-port of the middle antenna element. The measurement results show more than 30dB of X-pol/Co-pol discrimination for the antenna element. Besides, the phase variation is less than 10 degrees for all the amplitude states.

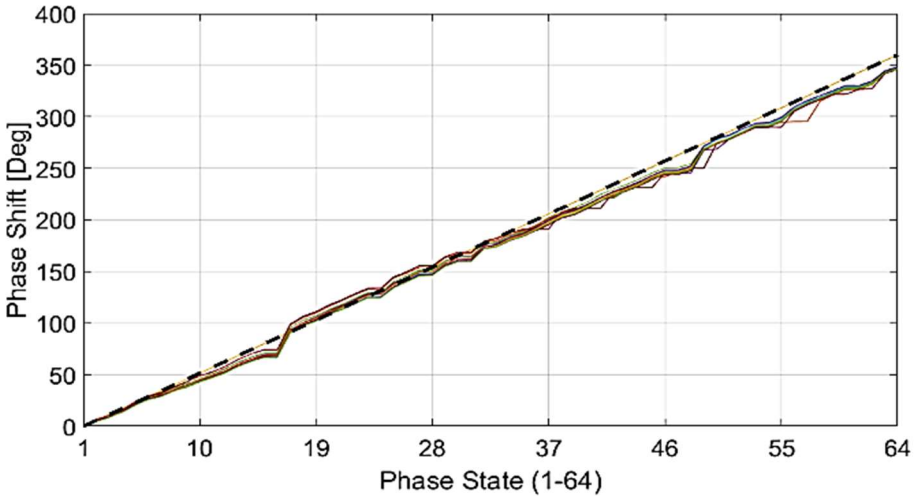

Figure 2-24. The differential phase shift for all the phase states with respect to state '1' for all the H-pols. (Dashed line shows the nominal values.)

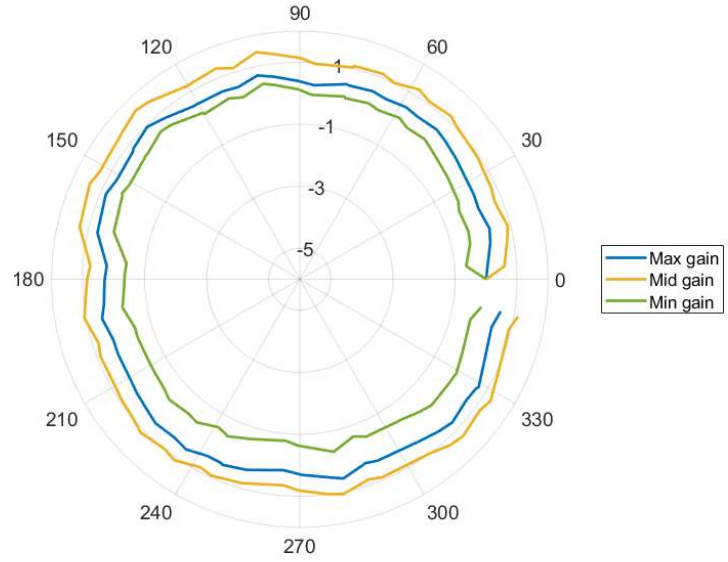

(a)

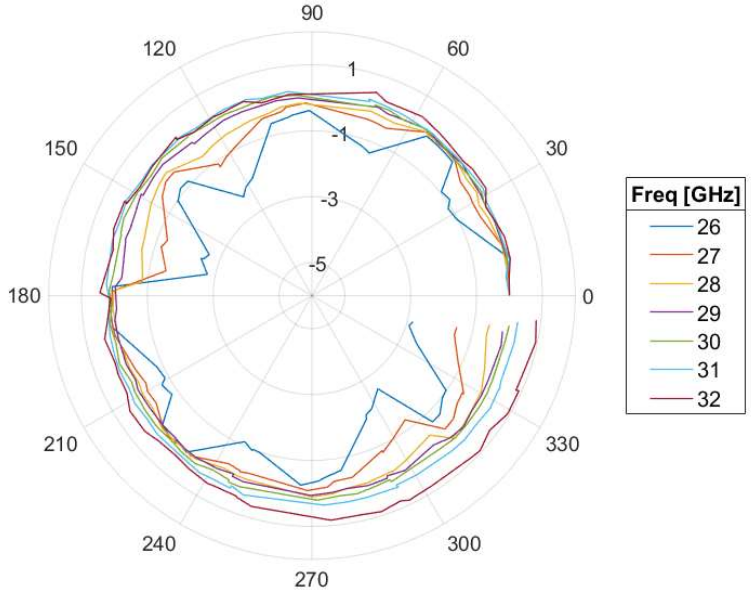

(b)

Figure 2-25. The differential phase shift for all the phase states with respect to state '0' for pot 12. (a) Different amplitude states. (b) Different frequencies.

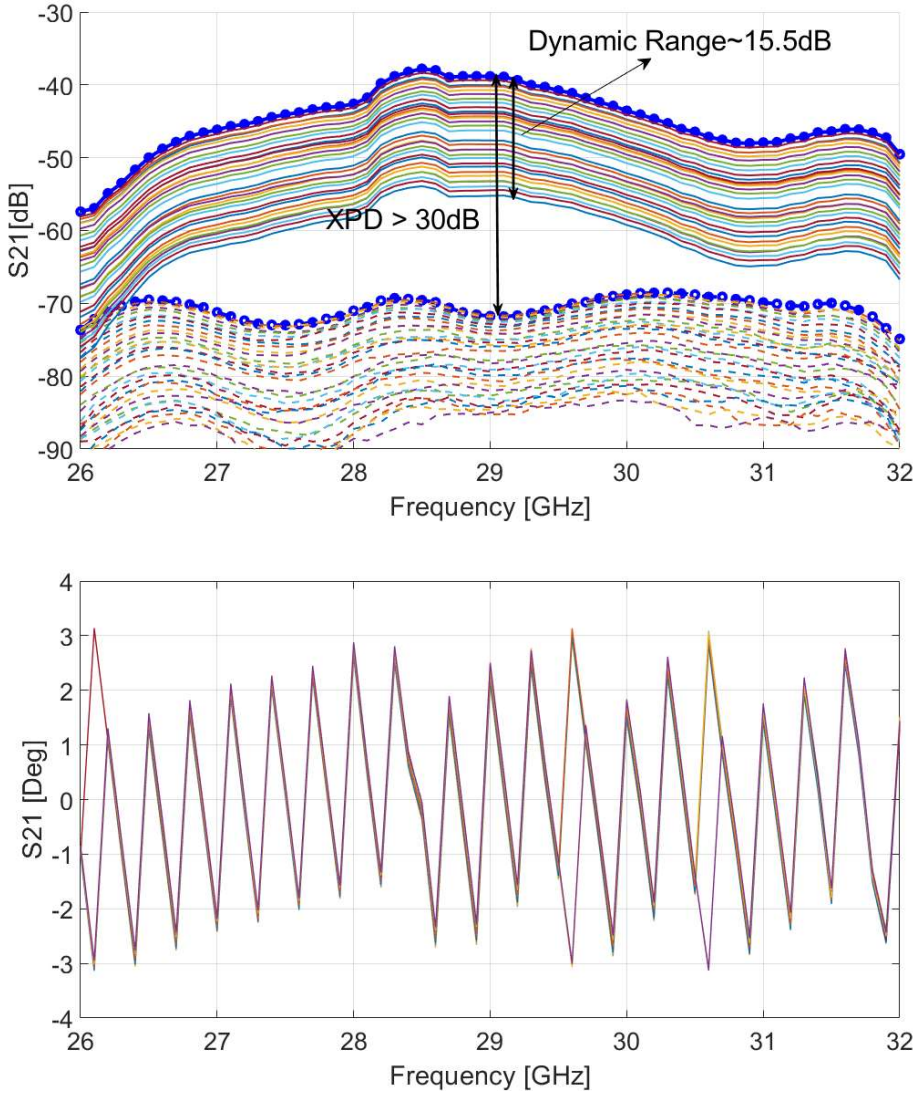

Figure 2-26. The co-pol and x-pol transmission coefficient results for all the amplitude states. (Port 12)

2.3.2 Radiation Characteristics Measurements

The calibration is executed in order to compensate for any unwanted phase and amplitude imbalance between the antenna ports. Then proper phase and amplitude states for

beamforming, steering and polarization control are set. Phase imbalance between the ports is within ~30° and the amplitude imbalance is ~3.5 dB as shown in Fig. 2-27.

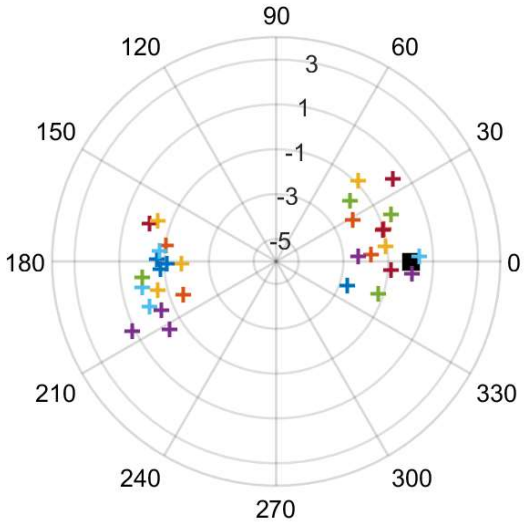

Figure 2-27. The phase and amplitude variation with respect to port 1. (Square mark)

Fig. 2-28 shows the phase and amplitude variation between the antenna ports before and after calibration. 180º phase shift between the ports is due to their orientation in the array as shown in Fig. 2-6. The antenna system is configured for left-handed circular polarization at boresight as shown in Fig. 2-28.

An open rectangular waveguide probe scans and measures the phase and amplitude of the antenna near field (NF) over a finite plane. The scanning range of the scanner is calculated based on the required maximum far-field angle, the size of the antenna and the distance between the probe and the antenna under test (AUT).

In this measurement, in order to accurately measure the far field pattern up to +/- 70 °, the near field data in the area of 0.26 m^2 is captured by the probe. The distance between the probe

and the antenna is 3 cm. Also, the sampling resolution in both X and Y direction is 0.435 λ_0. The resolution is calculated based on the Nyquist sampling theorem for the NF (Near Field) to FF (Far-Field) Fourier transform at the highest measurement frequency, which is f = 31 GHz in our measurement. After near field data acquisition, the system post processes the far field data by using a NF-to-FF Fourier transformation. The far field data is collected with angular resolution of $\Delta\theta = \Delta\varphi = 0.5°$. The directivity is then calculated by having the normalized radiated output power which is the integration of the normalized radiation intensity at the far field points.

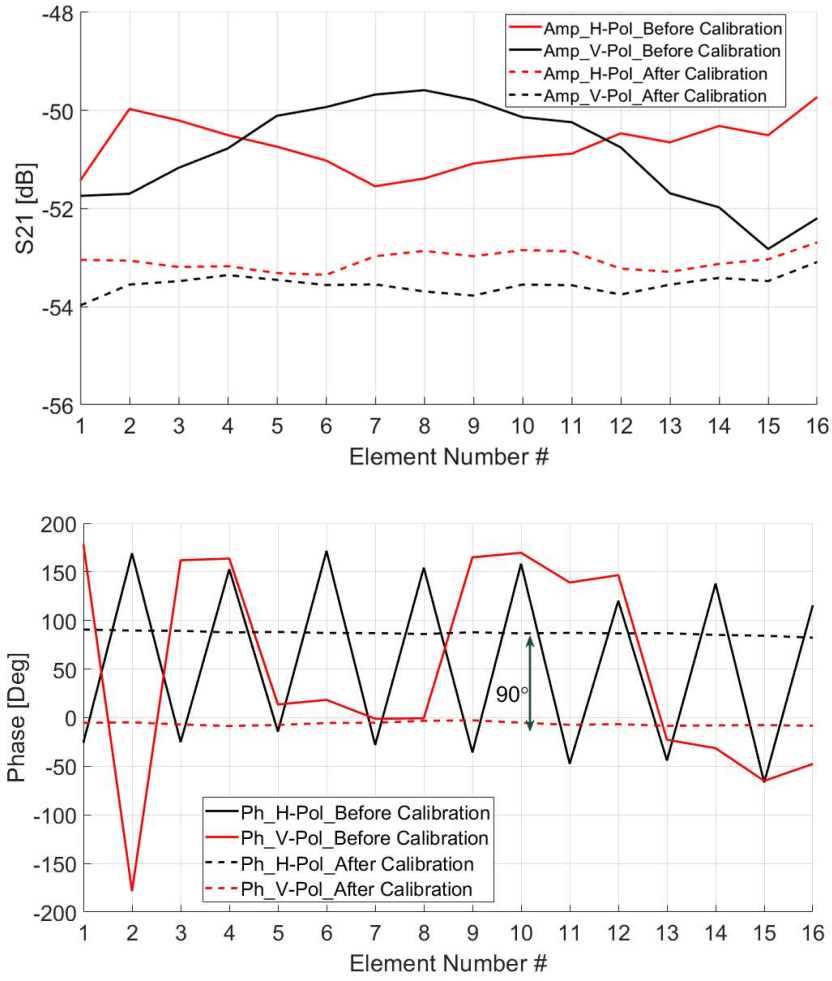

Figure 2-28. The phase and amplitude variation before and after calibration.

Radiation patterns for different scan angles are measured as shown in Fig. 2-29. In each plot, the radiation pattern is shown at 27, 28, 29, 30, and 31 GHz. X-pol/Co-pol discrimination is less than -20 dB for all the scan angles as shown in Fig. 2-29.

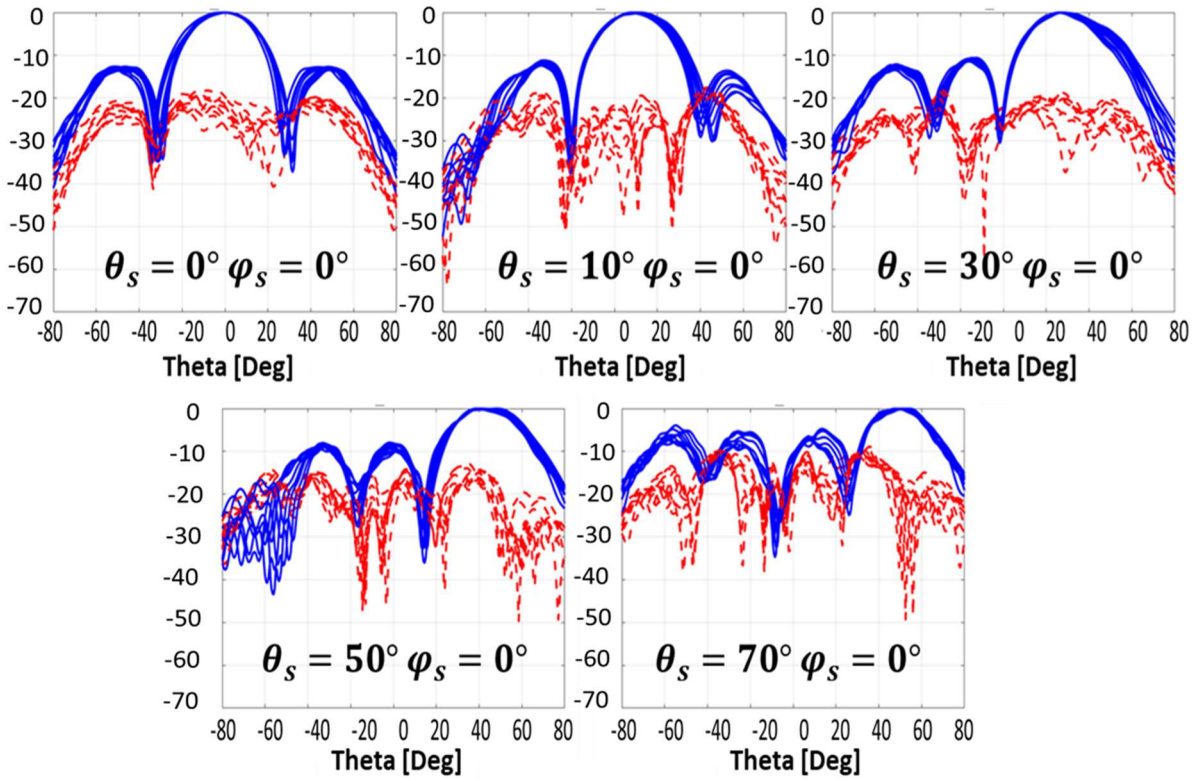

Figure 2-29. The normalized measured Co-pol and X-pol (red lines) radiation patterns for different scan angles (LHCP radiation). (Each plot shows the radiation patterns at 27, 28, 29, 30, and 31 GHz.)

The active gain of the system is 42 dBic at boresight at 29 GHz and the directivity is 16.8 dBic as shown in Fig. 2-30. The active gain of the antenna is defined by (2-1). In (2-1), the electronic gain is defined as (2-2).

$$\begin{aligned} &Antenna\ Active\ Gain \\ &= 10\log(16) + Electronic\ Gain\ [dB] \\ &+ Gain_{Single-element}[dB] - Splittere\ loss[dB] \end{aligned} \tag{2-1}$$

$$Electronic\ Gain\ [dB] = Beamformer\ Active\ Gain[dB] + 10\log(8) \tag{2-2}$$

The measured active gain of the AiP is in good agreement with (2-1), where

$$Splittere\ loss[dB] = 1.6\ dB$$

$$Electronic\ Gain\ [dB] = 30\ dB$$

$$Gain_{Single-element}[dB] = 4\ dB$$

The gain drops by 5 dB when the beam is steered to the scan angle of 70° which is due to the decrease in the aperture area as the beam scans, and the radiation pattern of the single-element antenna as well as the mutual coupling between the antenna elements. The effective isotropic radiated power (EIRP) at 1-dB compression point is 41 dBm at the boresight. Table II shows the comparison study of the proposed active system with respect to the state-of-the-art active phased-array systems operating at Ka-Band.

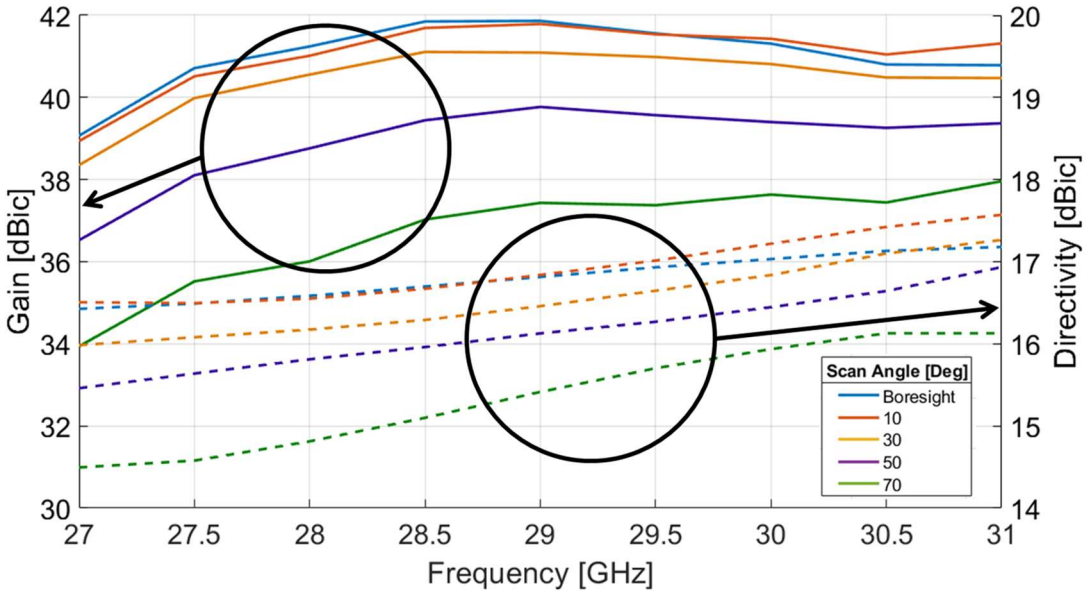

Figure 2-30. The measured active gain and directivity of the antenna system.

2.4 Conclusion

A 4×4 Ka-band active transmit phased-array AiP with polarization control for SATCOM-on-the-Move (SOTM) user terminal is demonstrated. The proposed active AiP is modular and scalable. The fabricated AiP provides 42 dB of active gain at the boresight. The module consumes 2.6 W of the DC power when all the ports are activated and the biasing voltage is 1.2 V. The effective isotropic radiated power (EIRP) of the current module is 41 dBm at the 1dB compression point at the output of active beamformers when the system radiates left-handed circular polarization. It consists of 16 dual-polarized cavity-backed patch antennas, four 8-channel active beamformers, and a 4-way splitter network. A mechanical test fixture with solderless RF connection mechanism is developed for testing of the AiP. It consists of a surface-mount mini coaxial connector which is connected to an SMA adaptor from the back. Spring-loaded connectors provide the biasing voltage and digital control signals.

TABLE II
PERFORMANCE COMPARISON OF THE PROPOSED SYSTEM WITH STATE-OF-THE-ART KA-BAND ACTIVE PHASED-ARRAY ANTENNA SYSTEMS

	This Work	UCSD [86]	UESTC [87]	IBM [6]
Mode of Operation	TX	TX	TX	TRX
Frequency [GHz]	27-31	27-31	29.5-30	27.2-28.7
Array Size	4×4	32×32	32×32	8×8
Polarization	Dual-Linear	Dual-Linear	Dual-CP*	Dual-Linear
Scan range (El / AZ)	±70/±70	±70/±70	±60/±60	±50/±50
EIRP [dBm][1,2,3,4]	41	76	73	54**
DC Power [1,2,3] [W]	2.6	169.2	108	0.319***

[1] @ 29 GHz

[2] Circular Polarization

[3] @ Boresight

[4] $OP_{1\text{-}dB}$

[*] Switch-Mode

[**] Linear Polarization

[***] Per Element

Chapter 3- A 2D Antenna Array with Integrated Passive Beamformer for Low-Cost and Efficient Millimeter Wave Applications

3.1 Introduction

Due to the small free space wavelength at mm-Wave frequencies, the implementation of a large-scale PAA system with hundreds to thousands of antenna elements, which is necessary for a reliable link for mid and long-range communication, is compatible with the form factor requirement of a communication system [38]. The low-cost and low-complexity implementation of large-scale PAA systems at mm-Wave is a necessity for mass production and deployment due to the large number of elements [38], [41]-[42]. As a consequence, all the techniques, architectures, and methods employed in implementing such systems must follow a low-cost and low-complexity approach. In PAA systems, beamforming can be implemented in different domains including RF, IF, LO, and digital baseband. Beamforming in RF domain is a low-cost, low-power approach in large-scale PAA systems mainly because one stage of up/down conversion is used [38]. Switched-beam antennas, reflect arrays, and lens antennas like transmit arrays are among architectures used in implementing PAAs systems in RF domain [43]-[45]. However, the focus of this article is on conventional phased-array antenna systems. Conventional PAAs can be classified into two types of active and passive. For large-scale PAA systems, passive architecture may not be a practical solution as the loss of the beamforming network degrades the performance of the system, particularly at mm-Wave where both dielectric and metallic losses are substantial. On the other side, active phased-array antenna (A-PAA) systems are able to realize a beamforming network with high performance at the expense of more complexity, cost, and power consumption. It is worth mentioning that A-PAA systems are assumed to be implemented based on tile structure rather than brick (slat) structure

in this article because of lower cost, smaller form factor and planarity at the cost of more dense integration levels [5]. A-PAA systems generally incorporates three main RF sub-systems: antenna elements, active beamformers (T/R modules), and power splitting/combining network. A T/R beamformer module encompasses a phase shifter (PS), a low-noise amplifier (LNA), a power amplifier (PA), either a variable-gain amplifier (VGA) or an RF attenuator, RF switches, and digital unit as shown in Fig. 3-1a [42]. In recent years, due to the advancements in silicon technology, it is possible that numbers of beamformer modules be merged on a silicon-based integrated circuit (IC) chip.

Different silicon-based processes including silicon-germanium (SiGe) bipolar CMOS (BiCMOS) and silicon CMOS technology have been used for the development of multi-channel beamformer ICs [46]-[49]. Besides, silicon-based technology makes it possible to integrate the digital unit in the IC chip. Employing multi-channel beamformer ICs in large-scale PAA systems has been expected to be a practical solution to reduce the cost and complexity of the system [47].

Hybrid approach that combines active and passive PAA architectures is an alternative solution in lowering the cost and complexity of A-PAA systems [50]. The system architecture of the hybrid is shown in Fig. 3-1b. In this approach, the active components (PA, LNA, etc.) are shared between groups of antenna elements which form subarrays, where the amplitude control is executable. Hybrid architecture could reduce the cost and complexity of the system if the number of active devices is reduced. However, passive beamformers with low insertion loss and compact size have to be developed.

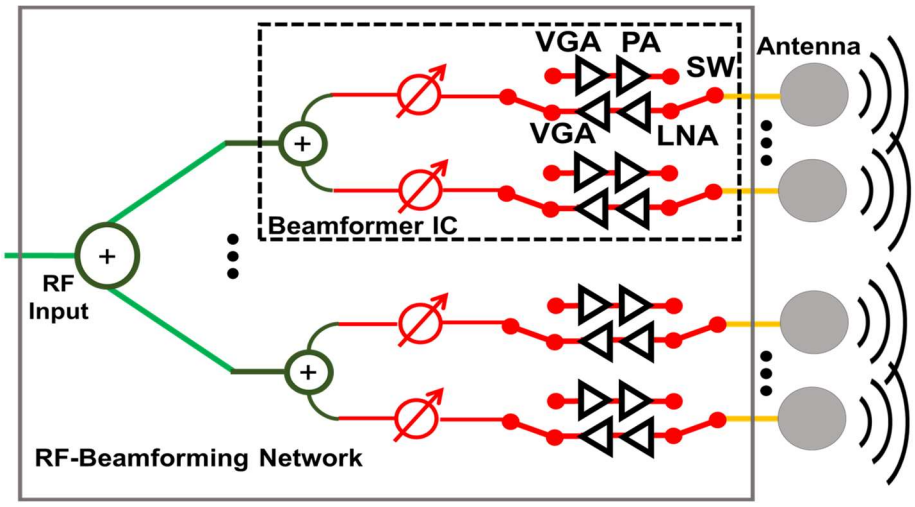

a) Conventional Active Phased-Array Antenna System

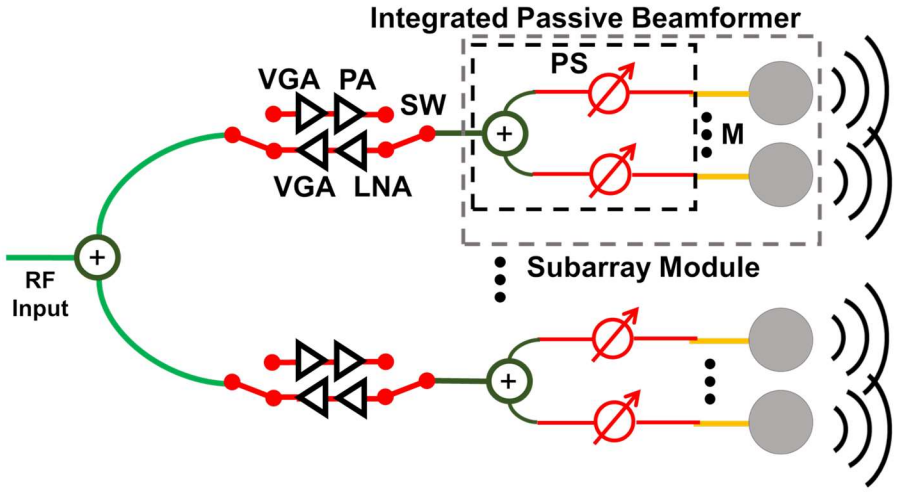

b) Hybrid Active-Passive Phased-Array Antenna System

Figure 3-1. Architectures of the antenna system.

In Section II, the system level analysis is presented to evaluate the performance of the hybrid approach in comparison to the active approach and its impact on lowering the cost and

complexity of the system. RF passive beamformer network incorporates a splitter/combiner and phase shifters [51]. The embedded phase shifter's insertion loss has to be as small as possible to avoid performance degradation. Besides, the phase shifter footprint has to be relatively small for planar 2D PAA design where the area of the phase shifter is limited by the distance (d) between the radiating antenna elements (approximately $d=0.5\times\lambda_0$ where λ_0 is the free space wavelength of the highest operating frequency). In [52], a 2D beam-steering P-PAA using compact tunable phase shifter based on barium-strontium-titanate (BST) film has been reported at X-band. The phase shifter shows average insertion loss of 8 dB which is extremely high. Liquid crystal (LC)-based phase shifters have also been used in P-PAA systems. In [53], an LC-based phase shifter has been employed in a 2×2 P-PAA. However, the measured gain of 6 dBi for the 2×2 antenna array shows that the phase shifter has high insertion loss. The LC-Based phase shifter reported in [54] shows the average insertion loss of 5.35 dB at Ka-Band. Semiconductor-based phase shifters also show high insertion loss [55]-[58]. Researchers also recently have shown switched-type phase shifter using phase change materials (PCM) technology at mm-Waves [59]. The results show that in order to cover the full phase tuning range of 360°, the PCM-based switched-line phase shifter shows the average insertion loss of 6 dB. On the other side, Phase shifters that employ microelectromechanical system (MEMS) technology have large footprint size for providing the full phase tuning range of 360º [60]. Controlling the characteristics of a guiding structure by moving a perturbing structure over the guiding structure has also been proposed as a low-cost solution for the realization of phase shifters. The type of the guiding and perturbing structure together with the actuation system determine the phase shifter performance. Metallic and dielectric structures have been used to alter the characteristics of transmission line [61]-[62]. These phase shifters are low-loss, and low-cost but the area of the phase shifter is relatively large for a planar 2D beam-steering P-PAA. In [26]-[29], dielectric slab with high dielectric constant of $\varepsilon_r= 100$ has been used. The

phase shifters show high performance with a low-profile structure. Although using high-dielectric materials shrink the area of this type of phase shifters, the phase shifters are not small enough for full phase tuning range of 360º which is required for maximum beam-steering angle, particularly for a 2D planar P-PAA. The proposed phased shifter not only shows low insertion loss and insertion loss variation for the full tuning range, but also has a small size. The phase is tuned by moving a high-dielectric ceramic material over a slow-wave microstrip line. The ceramic material has dielectric constant of $\varepsilon r = 60$ and loss tangent of $tg\delta = 0.005$. The movement is done using a magnetic actuation system. Prior works published by the authors' research group are not appropriate candidates for implementing 2D P-PAA systems since their footprint size for realizing a 360° full phase tuning range is large to be integrated with the feeding network of a 2D antenna array [63]-[66]. In this thesis, the system analysis and design aspects of a planar 2D 4×4 fully passive phased-array antenna module at Ka-Band are presented. In Section 3-2, the system analysis is presented. The phase shifter technology is discussed in detail in Section 3-3. Sections 3-4 covers the design of the antenna array and the splitter/combiner network respectively. The actuation systems, fabrication, assembly, and packaging are covered in section 3-5. The simulation and measurement results of the beam steering are reported in Section 3-6.

3.2 System Analysis and Architecture

The system level architecture of two antenna systems are shown in Fig. 3-1. RF performance of two systems are evaluated by calculating effective isotropic radiated power (*EIRP*) and gain-to-noise-temperature (*G/T*) for each system. It is assumed that the number of antenna elements and the antenna unit cell are the same for both of the architectures. Equation (3-1) shows the *EIRP* for an A-PAA, *N* is the number of antenna elements in the array. *Pout* is the generated output power in *dBm* from the power amplifier in transmit (TX) mode.

$$EIRP[dBm] = P_{total} + G = 20log(N) + P_{out} + G_{single-element\ antenna} \quad (3\text{-}1)$$

For hybrid architecture, *EIRP* is calculated in (2) and (3), where *M* is the number of antenna elements in the subarray module, $L_{Passive\ Beamformer}$ is the loss of the passive beamformer network in the subarray module, and P'_{out} is the amount of output power from the power amplifier injected into the subarray module.

$$EIRP[dBm] = 10log(N/M) + P'_{out} + 10\log(N) + G_{single-element\ antenna} - L_{Passive\ Beamformer} \quad (3\text{-}2)$$

$$L_{Passive\ Beamformer}[dB] = L_{Phase\ Shifter} + L_{Splitter/Combiner} \quad (3\text{-}3)$$

It is apparent that the passive beamformer loss is implicitly related to the subarray size (*M*). As the subarray size becomes larger, the routing of the splitter/combiner network becomes longer and as a consequence the passive beamformer shows higher loss. In receive (RX) mode, *G/T* for an A-PAA is calculated in (4) where *F* is the noise factor of the low-noise amplifier, T_0 is the ambient temperature, and T_{ant} is the antenna temperature. For the hybrid, *G/T* is calculated in (5) where *F'* is the noise factor of the low-noise amplifier in front of the subarray module. Hybrid architecture maintains the same *EIRP* and *G/T* as a conventional A-PAA if (6) and (7) are satisfied in TX and RX modes respectively. In other words, active devices with better performance must be selected in hybrid architecture to compensate for the loss contributed by the passive beamformer and power splitter/combiner circuit. GaAs, InP, and

GaN technology-based active devices are excellent candidates for hybrid architecture compared to silicon-based counterparts as they provide better noise figure and output power as shown in Table III.

$$G/T\ [dB/K^{\circ}] \approx 10\log(N) + G_{single-element\ antenna} - 10\log\big((F-1)T_0 + T_{ant}\big) \tag{3-4}$$

$$G/T\ [dB/K^{\circ}] \approx 10\log(N) + G_{single-element\ antenna} - L_{Passive\ Beamformer} - 10\log\big((F'-1)T_0 + T_{ant}\big) \tag{3-5}$$

$$P'_{out} = P_{out} + 10\log(M) + L_{Passive\ Beamformer} \tag{3-6}$$

$$10\log\big((F-1)T_0 + T_{ant}\big) = 10\log\big((F'-1)T_0 + T_{ant}\big) + L_{Passive\ Beamformer} \tag{3-7}$$

TABLE III
THE PERFORMANCE OF POWER AMPLIFIER AND LOW-NOISE AMPLIFIER AT KA-BAND

Architecture	Technology	NF [dB]	$P_{out\text{-}1dB}$*** [dBm]	Ref
Active	SiGe-BiCMOS* 130 nm	4.6	10.5	[30]
Hybrid	GaAs pHEMT** 0.15 μm	2.8	24.5	[31]

* The numbers are based on the measurement results of a 4-channel TRX beamformer IC.

** The numbers are based on the measurement results of a TRX front-end IC.

*** The power amplifiers are class-AB amplifiers.

For a quantitative analysis, based on the RF performance of the low-noise amplifiers (LNA) and the power amplifiers (PA) at Ka-band reported in Table III, the passive beamformer loss ($L_{Passive\ Beamformer}$=2.88 dB) is calculated by (7), and M=12.93 is obtained by (6), assuming that T_{ant}=40 k and T_0=300 k . For realizing a passive beamformer with a corporate-fed network ($M=2^n$) in this work, M=16 is chosen.

TABLE IV
THE PERFORMANCE OF STATE-OF-THE-ART PHASE SHIFTER TECHNOLOGIES AT KA-BAND

Technology	Size [mm^2]	Loss [dB]	Δφ	Ref
Silicon CMOS - 65 nm	0.16	7.75	360	[55]
Silicon Bi-CMOS - 180 nm	0.18	13	320	[56]
RF SOI CMOS - 45 nm	0.28	11.5	182	[57]
GaAs- 0.15 µm	0.78×1.69	12.5	360	[58]
Liquid Crystal	0.38	5.35	275	[54]
Ge/Te Phase-Change Material(PCM)	1.4	4.7	173	[59]
RF MEMS	4×2.6	5.95	120	[60]
MEMS-Based	2.4×3	2	380	This work

The previous calculations show that the number of active elements in an A-PAA system is reduced by a factor of sixteen if a passive beamformer is realized with the inherent loss of $L_{Passive\ Beamformer}$=2.88 dB. This scale of reduction is able to reduce the cost and complexity of a large-scale A-PAA system as the number of active elements reduces significantly. The realization of a passive beamformer with the loss of 3dB ($L_{Passive\ Beamformer}\approx$ 3 dB) is challenging. Based on (3), the loss includes the splitter/combiner loss and the phase shifter loss. If 1.5 dB of the loss is accounted for the splitter/combiner with sixteen branches at Ka-Band, the loss of the phase shifter is almost 1.5 dB. Table IV lists some of the state-of-the-art phase shifter technologies at Ka-Band. The phase shifters either show high insertion loss or

have large footprint size which make their integration in 2D P-PAA design impractical. In this work, a phase shifter with low insertion loss and small footprint size operating at Ka-band which is suitable for 2D P-PAA systems will be discussed in the next section.

3.3 Phase Shifter Technology

3.3.1 Principle of Operation

Being able to tune the propagation constant of a transmission line realizes a tunable phase shifter. Considering the scattering matrix of an ideal transmission line with the length (l) and the phase constant (β) as in (8), it is evident that as the phase constant of the transmission line changes, the insertion phase of the transmission line changes consequently. The range of variation (Δφ) depends on the transmission line length and the phase constant difference (Δβ) as in (9).

$$S_{ideal\ T.L} = \begin{bmatrix} e^{-j\beta l} & 0 \\ 0 & e^{-j\beta l} \end{bmatrix} \tag{3-8}$$

$$\Delta\varphi = -(\Delta\beta)l \tag{3-9}$$

It is obvious that a larger phase constant difference makes the full phase tuning range of 360º to be realized by a shorter length of the transmission line and results in having a tunable phase shifter with lower loss and smaller size.

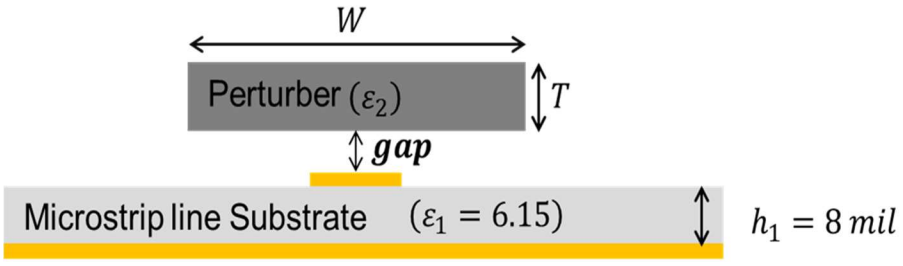

Figure 3-2. Transversal view of the microstrip line loaded with a perturber

In this research, a microelectromechanical (MEMS)-based approach is employed to realize the tuning of the insertion phase of the transmission line. Fig. 3-2 shows the proposed phase shifting mechanism that is achieved by changing the gap distance (Gap) between the RF-transmission line (T.L.) and the dielectric slab (perturber) with high dielectric constant of ε2 as presented by the authors' research group [26]-[27]. Although various T.L technologies have been used for implementing phase shifters using this mechanism, microstrip line technology is chosen to ease the integration of the phase shifter structure to the feeding network of a 2D antenna array which is based on microstrip line technology as well. Microstrip line (MSL) shows a relatively lower insertion loss and more compact routing area. More details about the antenna's feeding network will be discussed in Sections IV. It must be emphasized that the microstrip line design parameters including the substrate material and the thickness are specified by the antenna's feeding network design. Besides, the phase shifter size must be fitted into an area of 3×3 mm2 at 30 GHz. On the other side, the perturber permittivity (ε_2), width (W), and thickness (T) must be chosen such that the structure have a single-mode operation. Modal analysis of the phase shifter structure has been investigated and the first two modes of the structure are shown in Fig. 3-3a and Fig. 3-3b, respectively.

The first mode is the desired mode and its' phase constant depends on the gap distance which is necessary for the phase tuning. Parametric study (not shown for brevity) shows that as the dielectric slab be thicker, wider, and have higher permittivity, larger phase constant difference can be achieved for a specific gap distance as long as the structure has a single-mode operation condition. However, the availability of the dielectric and the size constraints are taken into consideration as well. Full EM-simulations show that the perturber permittivity, ε_2=60, the thickness of T=200 um, and the width of W=1.2 mm, guarantees single-mode operation and provides maximum possible phase constant difference by varying the gap distance from 2 um

up to 500 um (unloaded microstrip line). It is assumed that the gap distance of gap=2 um is the minimum gap distance which can be achieved practically.

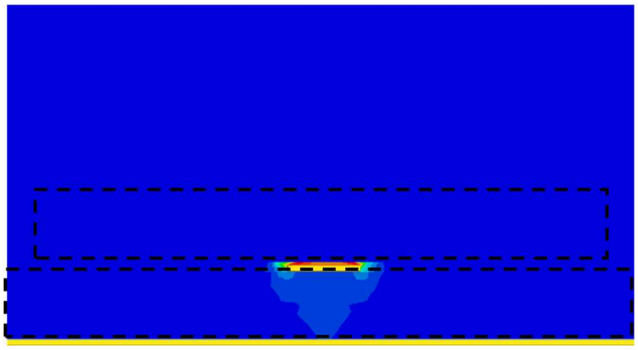

(a) Loaded Microstrip line – 1st mode

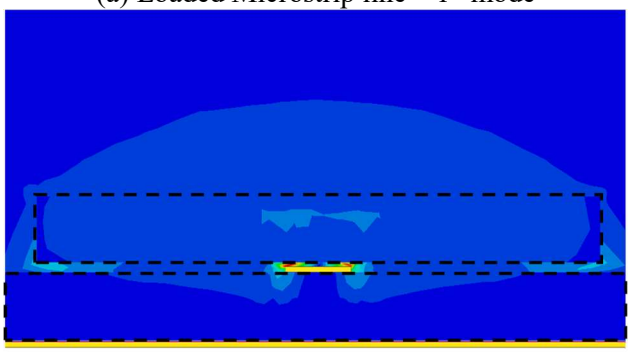

(b) Loaded Microstrip line – 2nd mode

Figure 3-3. The first two modes of the phase shifter

The phase constants of the proposed phase shifter structure for two cases, loaded and unloaded MSL, are numerically studied and the difference is calculated as shown in Fig. 3-4. In loaded case, the gap distance between MSL and the perturber is chosen as gap=2 um. Fig. 3-4 shows that the phase constant difference is $\Delta\beta$=767 rad/m.

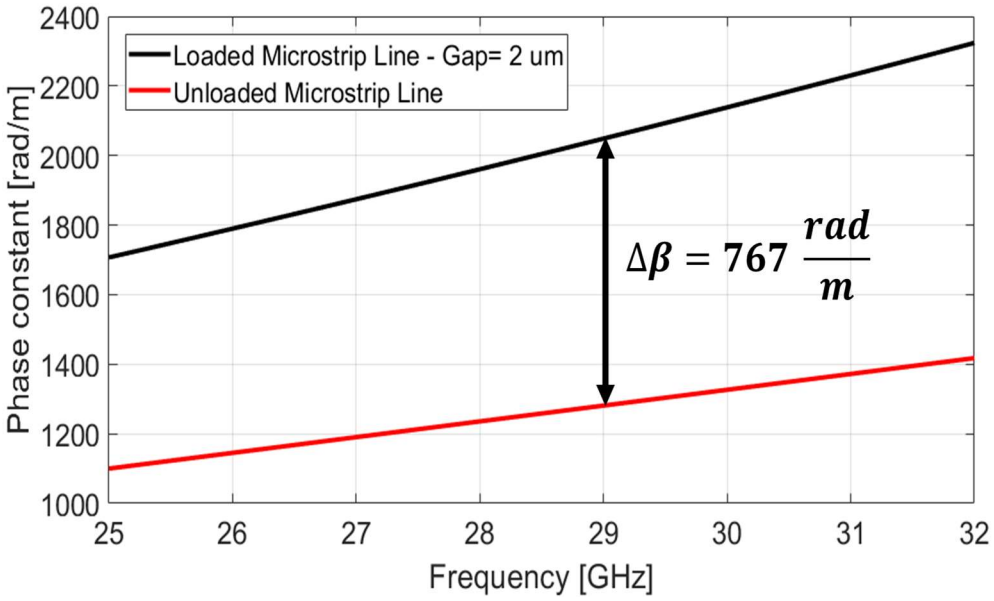

Figure 3-4. The phase constant versus frequency of the loaded and unload microstrip line.

For the full phase tuning range of $\Delta\varphi = 360°$, the perturber length (l) must be l=8.19 mm using (9). For completeness, the frequency response characteristics of the MSL phase shifter with the length of l=10 mm over the operating frequency band is shown in Fig. 3-5 for different gap distances.

The phase shifter shows low insertion loss (IL) of 0.5 dB in average over a wide range of frequency at all the gap distance states as shown in Fig. 3-5a. It is attributed to the fact that the electric field is almost confined inside the air gap between the perturber and the MSL as shown in Fig. 3-3. Also, it achieves wide phase tuning range up to 380° at 29 GHz as shown in Fig. 3-5b. Nevertheless, it was discussed in Section I that one of the constraints for the phase shifter design is the limited available area size of 3×3 mm2 at 30 GHz. Length of l=8.19 mm clearly violates the size constraint for the phase shifter. In order to shrink the size of the phase shifter,

slow-wave mechanism is employed [74]-[75]. In the next sub-section, the design and implementation of the phase shifter is presented.

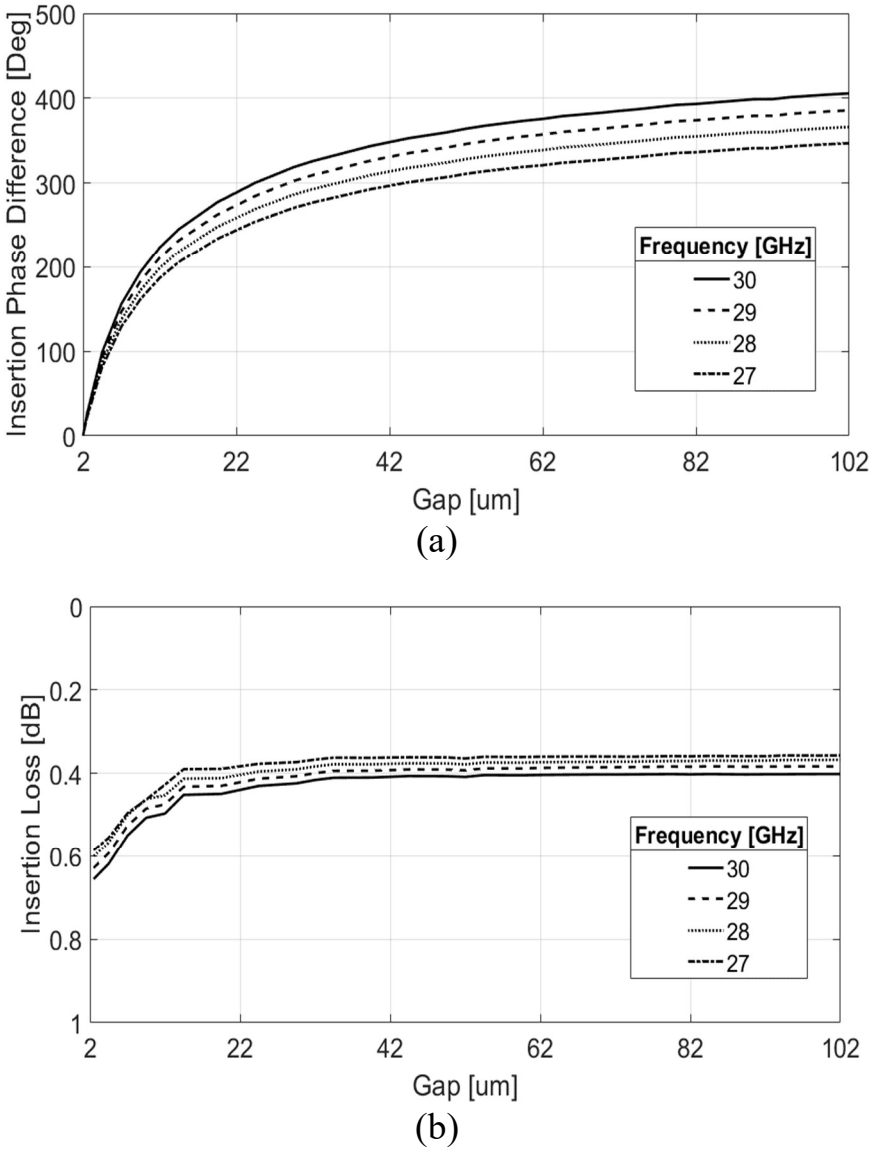

Figure 3-5. The insertion phase difference and (b) the insertion loss of the phase shifter versus the gap distance for different frequencies.

3.4 Design, Simulation and Measurement Results

The structure of the tunable phase shifter is shown in Fig. 3-6. The slow-wave mechanism is realized by adding capacitive loads (CV) to the MSL periodically. In this design, CV is realized by a series L-C resonator operating below its resonance frequency. Cc is the capacitance between the edge of the MSL and the stub and L is the inductance due the shorted stub. A series L-C resonator below its resonance frequency behaves capacitively with larger capacitance value.

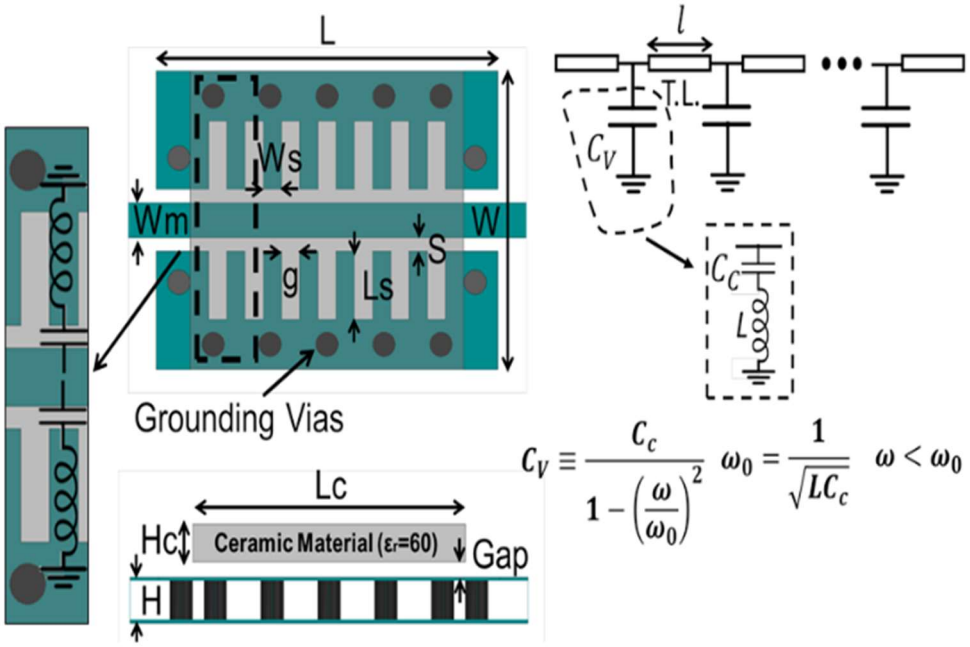

Figure 3-6. The structure of the slow-wave microstrip line phase shifter.

The proposed phase shifter is designed and optimized to operate over the frequency range of 27-30 GHz. RO4360 with the dielectric constant of εr=6.15, the loss tangent of tgδ=0.003, and the thickness of H=0.203 mm is used to design the MSL with the slow-wave structure. The design parameters are listed in Table V. The resonator design parameters (i.e. Ws, Ls, and S) are optimized such that it resonates at 32 GHz at the gap distance of gap= 2 um. The unit cell

length is also set to l=2×Ws= 320 um. Each unit cell provides 50º of phase shift at 30 GHz. Eight unit cells in cascade satisfy the full phase tuning rang coverage at 30 GHz.

TABLE V
DESIGN PARAMETERS OF THE STRUCTURE (MM)

Parameter		Parameter		Parameter	
L	3	Ws	0.16	S	0.11
Lc	2.4	Ls	0.55	Wm	0.28
W	2.4	g	0.16	Hc	0.2

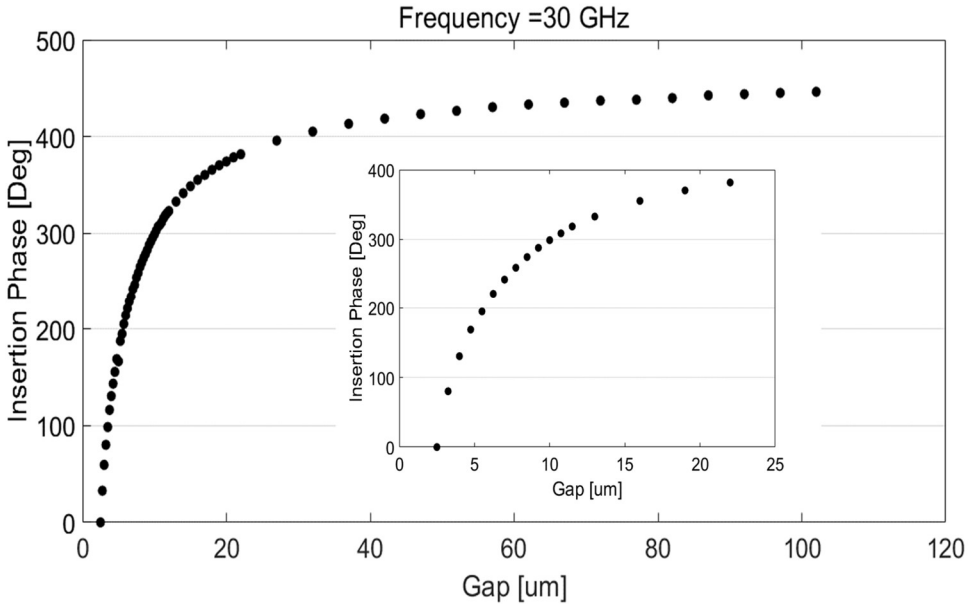

Figure 3-7. The phase tuning response with respect to the Gap distance at 30 GHz.

The insertion phase of the phase shifter for all the tuning states is shown in Fig. 3-7a. It shows the phase tuning range of ~ 430° at 30 GHz. Fig. 3-7b shows the insertion loss of 1±0.6 dB and the return loss of more than 10 dB for all the tuning states over the operating bandwidth. The profile of the phase tuning with respect to the gap distance at 30 GHz is shown in Fig. 3-8. The phase tuning response with respect to the gap distance does not follow a linear trend as shown in Fig. 3-8. Also, the inset in Fig. 3-8 shows that the phase tuning range of 360° is obtained when the gap distance ranges from 2-50 um.

A low-profile magnetic actuator is employed to move the ceramic material with respect to the line and changes the gap distance as discussed in [26]. The fabricated phase shifter prototype is shown in Fig. 3-9. Fig. 3-10a shows the phase tuning range of 380° can be reached by the phase shifter at 30 GHz. The phase shifter shows the return loss of more than 10 dB and the insertion loss of 1.3±0.9 dB in the frequency range of 27-30 GHz at all the tuning states as shown in Fig. 3-10b. It is observed that the actuator draws up to 60 mA of the DC current over DC voltage range of 0-0.5 volts for tuning the phase. Table VI compares the performance of the proposed phase shifter with existing phase shifters which employ the same technique of loading perturbation to a guiding structure. The results in Table VI shows that the proposed phase shifter provides the full phase tuning range of 380° in a smaller footprint size besides maintaining high figure of merit of FoM=190 at 30 GHz where FoM is defined by the ratio of the maximum phase tuning range and the maximum insertion loss for all the tuning states at a specific frequency.

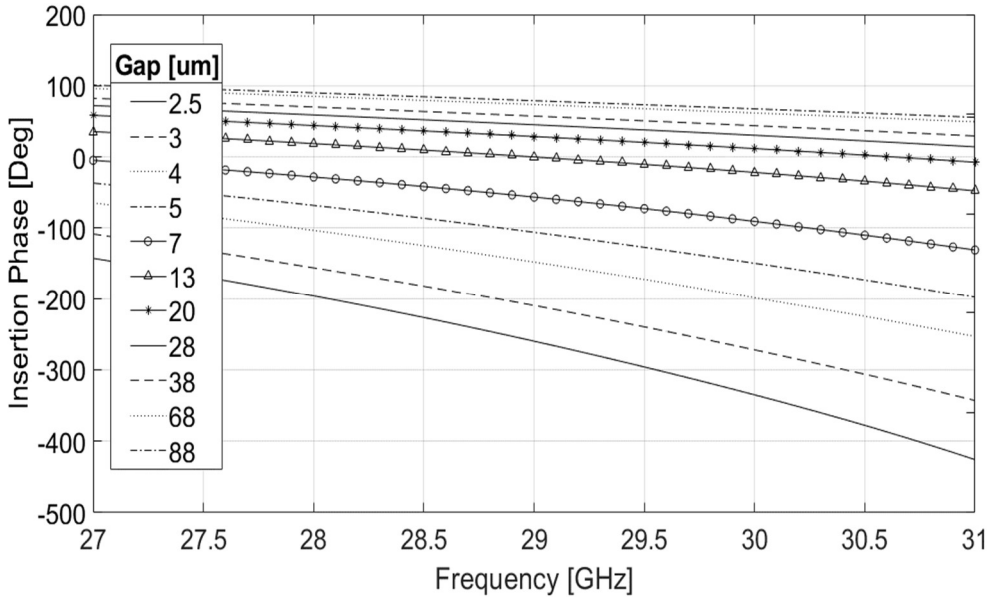

(a)

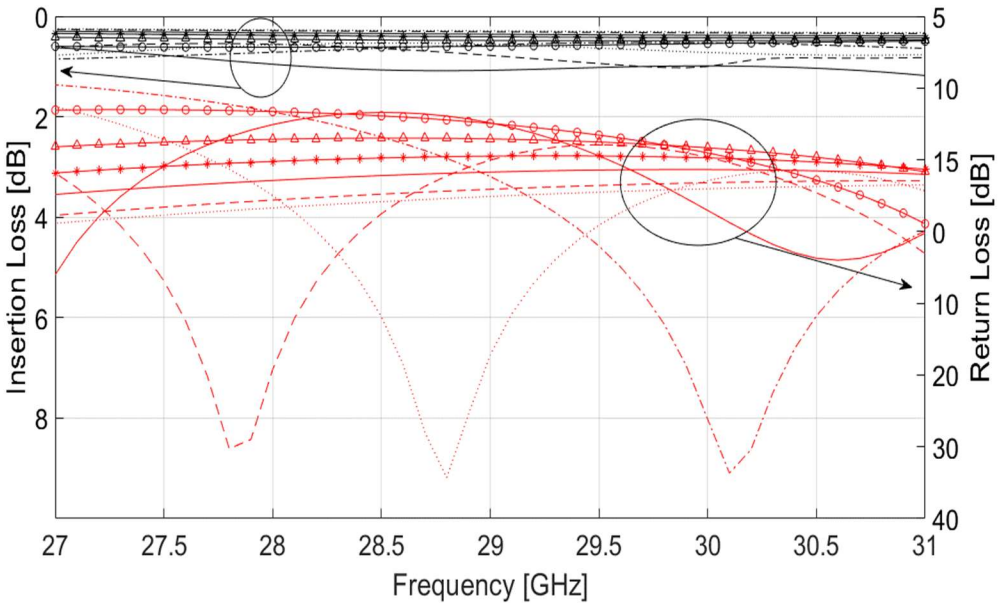

(b)

Figure 3-8. The simulation results of the frequency response of the phase shifter for different gap distances.

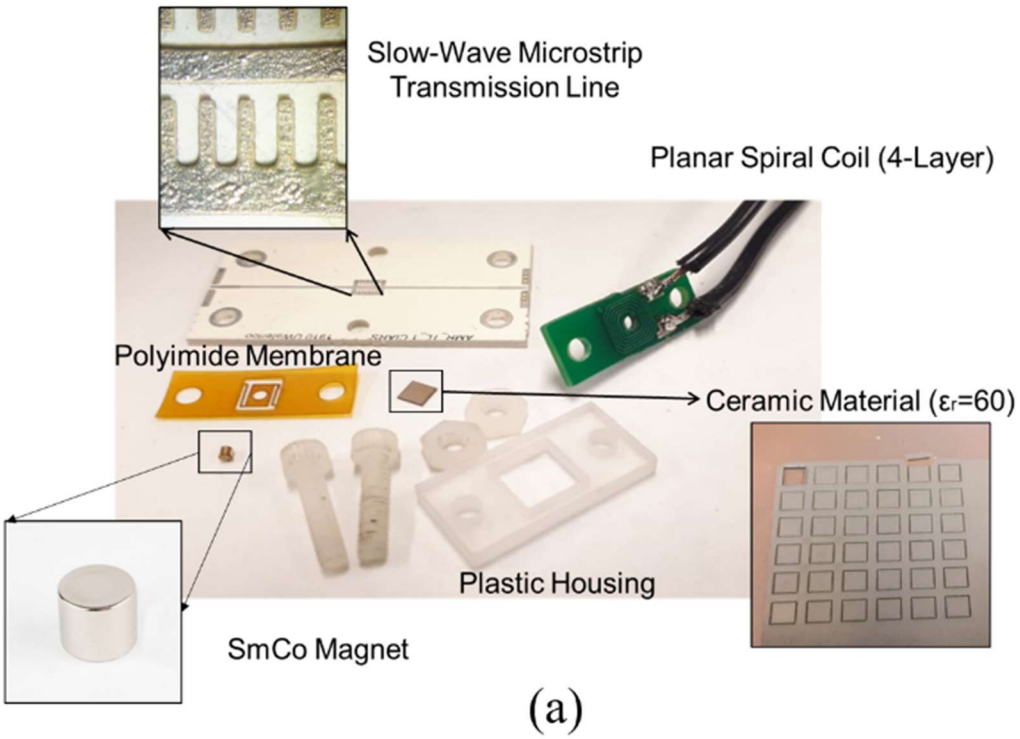

(a)

(b)

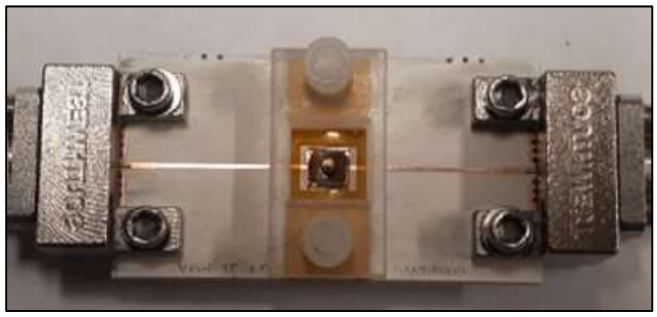

(c)

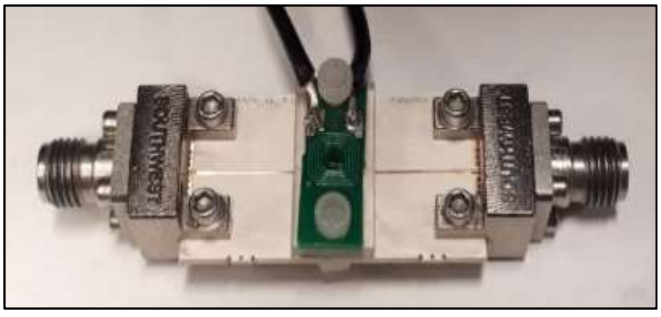

Figure 3-9. (a) Components of the phase shifter. (b) Permanent magnet and the ceramic are adhered to each side of the membrane using adhesive material. (c) Packaged phase shifter.

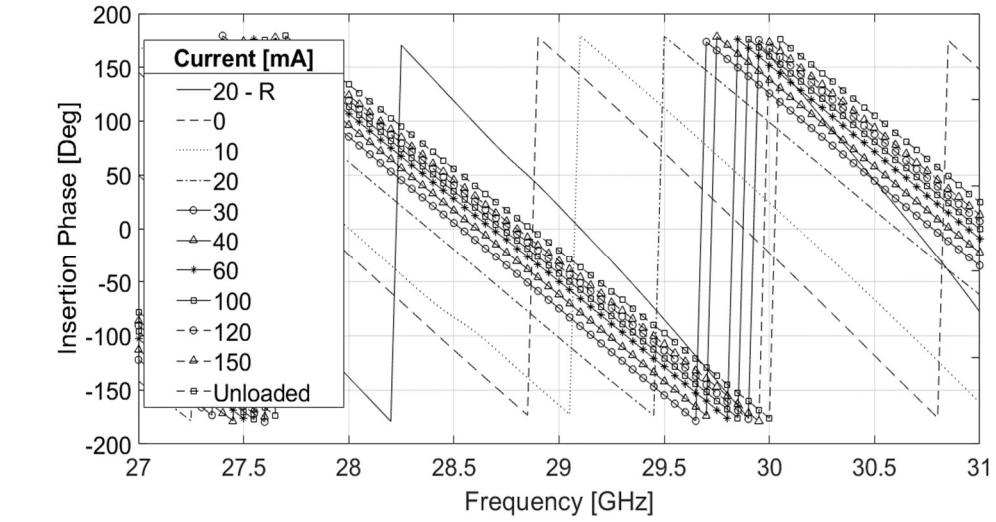

(a)

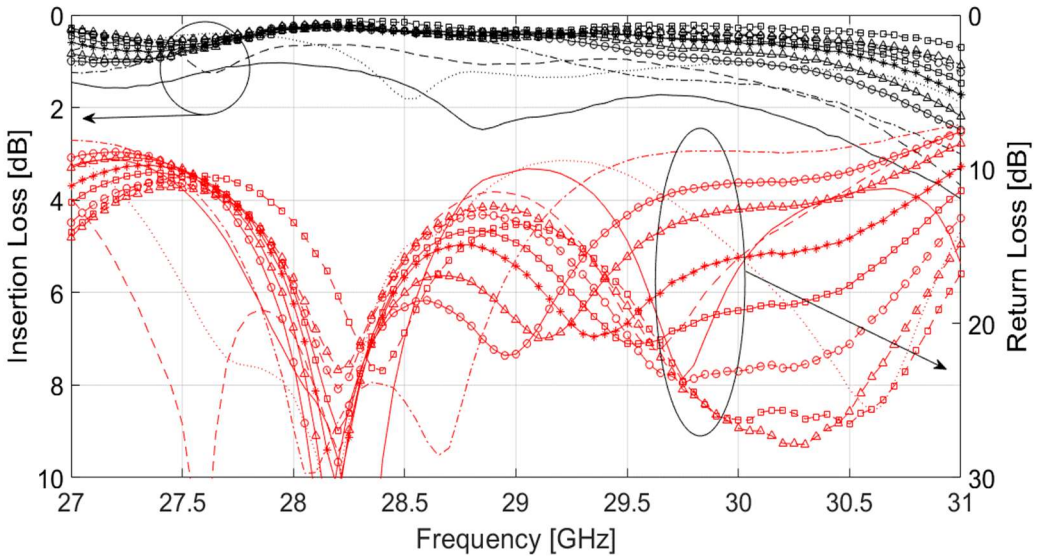

(b)

Figure 3-10. Measurement results of the frequency response of the phase shifter for different DC currents.

TABLE VI
PERFORMANCE COMPARISON OF PHASE SHIFTERS EMPLOYING THE TECHNIQUE OF LOADING PERTURBATION TO A GUIDING STRUCTURER

Ref.	[61]	[63]	[64]	[65]	This Work
Freq [GHz]	6	30	30	88	30
Guiding Structure	Microstrip Line	Grounded Coplanar Waveguide	Substrate Integrated Waveguide	Silicon On Glass	Slow-Wave Microstrip Line
Area [λ_0^2]	2.4×0.36	0.4×0.3	0.6×.4	1.46×2.93	0.3×.24
Perturber	Metal	Dielectric (εr=100)	Dielectric (εr=100)	Silicon	Dielectric (εr=60)
Δφ [Deg]	860	285	275	114	380
I.L [dB]	3.8	1.2	1.5	0.6	2
FoM (Δφ/I.L)	226	237	183	190	190

3.5 Antenna Array

3.5.1 The Antenna Element

The antenna element is an elliptical patch antenna excited by a microstrip line through an L-shaped slot [76]. The antenna structure and the buildup is shown in Fig. 3-11.

Three metal layers, two dielectric substrates and an adhesive layer form the buildup of the structure as it is shown in Fig. 3-11. RO4003 is used as the antenna substrate. It has the permittivity of εr= 3.55, the thickness of 0.508 mm, and the loss tangent of tgδ=0.0035. The patch has an elliptical shape with the major axis length of R1=2.8 mm and the minor axis length of R2=2.45 mm. The elliptical shape provides more degrees of freedom for the realization of circularly-polarized (CP) radiation. The feed substrate is RO4360 with the dielectric constant of εr= 6.15, the thickness of h3= 0.203 mm, and the loss tangent of tgδ= 0.003. The adhesive

is Rogers 4450 with the permittivity of εr= 3.5, the thickness of h2=0.203 mm, and the loss tangent of tgδ=0.003. An L-shaped slot in the second metal layer having two arms with lengths of ls1=1.311mm and ls2=1.529 and slot width of Wslot=0.161 mm is used for excitation of two degenerated orthogonal modes with 90° phase difference for CP radiation. In order to provide the proper input matching, the length of Lstub is chosen to be Lstub= 1.37 mm. The antenna element is surrounded from the sides by periodic boundaries and from the top and bottom by radiation boundaries in the simulation environment. The antenna has a wide impedance bandwidth of 27-31 GHz. The simulation results show the peak gain of 6.7 dBic as shown in Fig. 3-12a and the axial ratio of less than 3 dB in the frequency range of 28.2-29.6 GHz as shown in Fig. 3-12b.

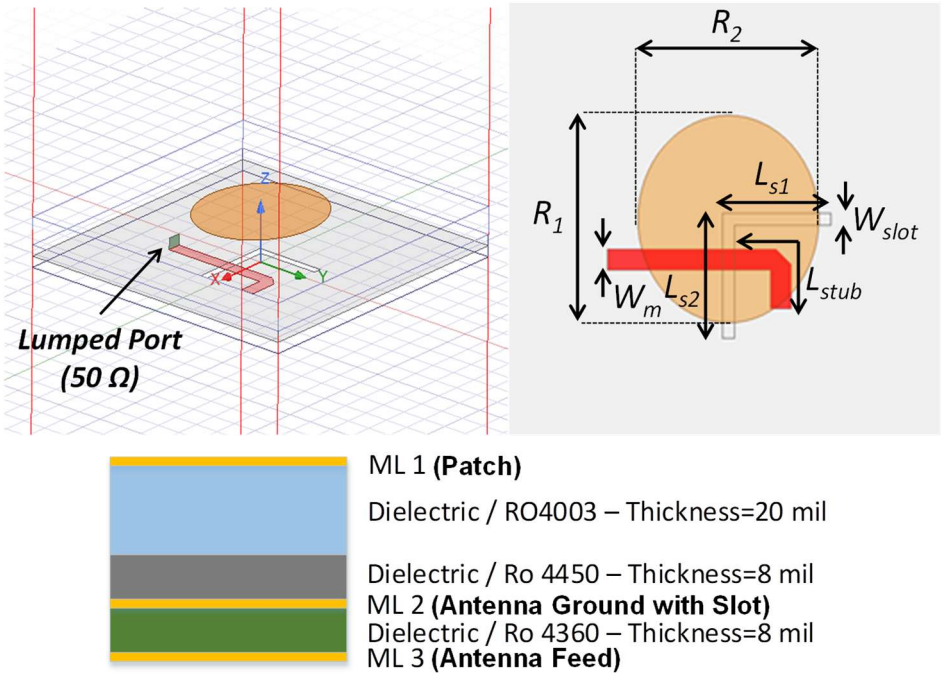

Figure 3-11. The antenna element structure and build up.

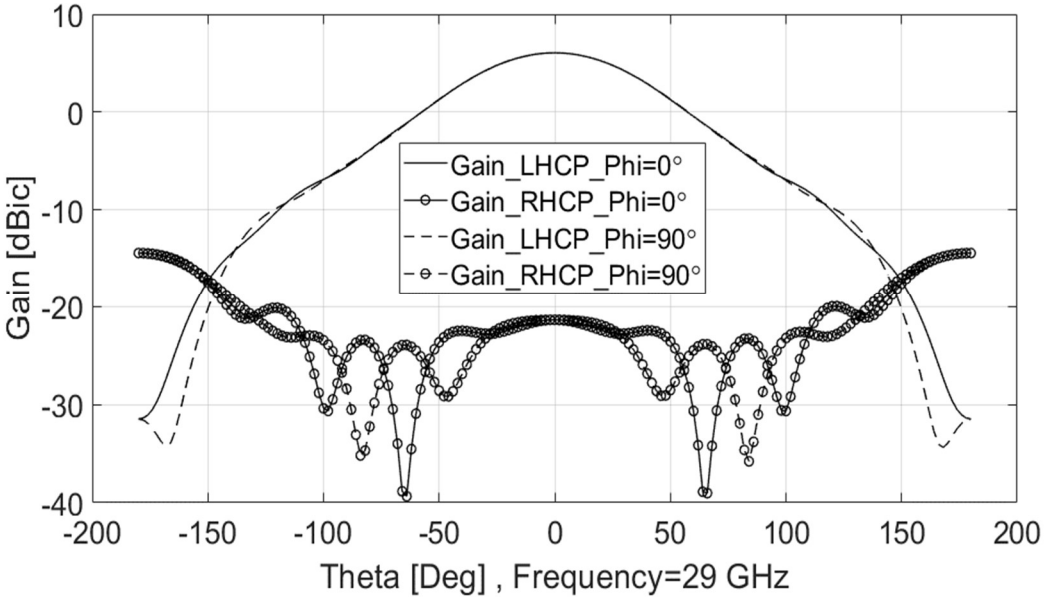

(a)

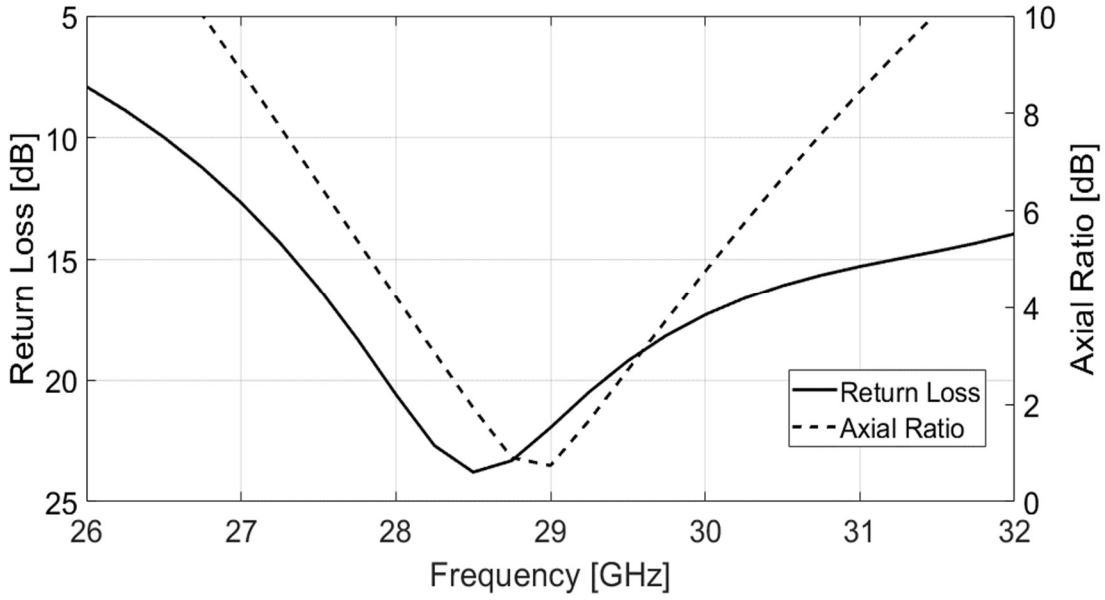

(b)

Figure 3-12. The antenna element simulation results of the return loss and the radiation pattern.

3.5.2 Array Configuration

Sixteen antenna elements are located in square lattice configuration as shown in Fig. 3-13. The element spacing is $0.6\times\lambda_0$ where λ_0 is the free space wavelength at 30GHz. The specified distance between the antenna elements allows grating lobe-free scanning angle up to $\theta_s=46°$ theoretically. The upper half of the array is rotated 180° counterclockwise around the z- axis with respect to the lower half to provide more space for laying out the phase shifters and the splitter/ combiner network. In order to compensate for the rotation, 180° phase shift is provided in the Splitter/Combiner network design. Non-radiating antenna elements are located at the four edges of the array to provide the same boundaries seen by the central elements of the array as shown in Fig. 3-13 [77].

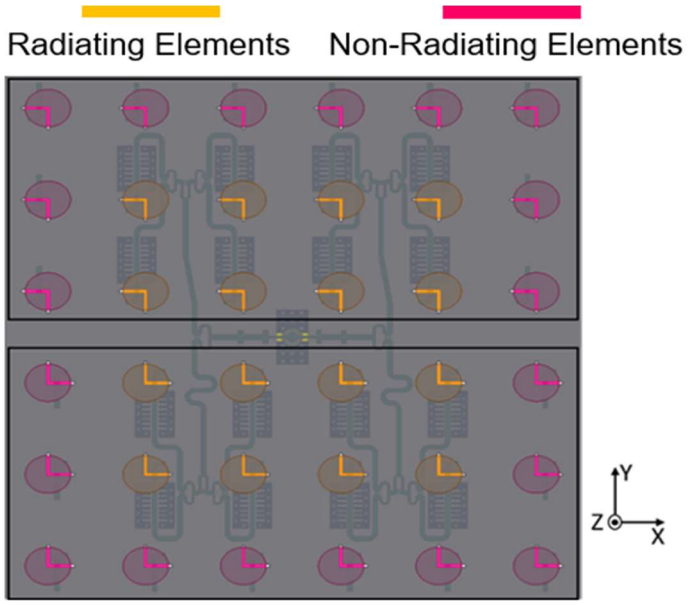

Figure 3-13. The array configuration

3.5.3 Splitting/ Combining Network

The feeding network is a sixteen-way microstrip Wilkinson power divider which is fed by a miniaturized surface-mount connector. RO4360 with the dielectric constant of $\varepsilon r = 6.15$, the thickness of $h3 = 0.203$ mm, and the loss tangent of $tg\delta = 0.003$ is used for the proposed power divider. The proposed power divider shows the average insertion loss of 1.5 dB with ±0.5 dB variation. Also, it shows the phase imbalance of less than 10º among the power divider output branches for each half. It is worth mentioning that half of the output ports show extra phase shift of 180º to compensate for the rotation of the upper half of the antenna array as it was discussed in the previous section. By employing the Wilkinson power divider, the coupling level between the output branches are relatively low and the output branches are matched which is necessary in passive phased-array antenna systems since the phase shifter is directly connected to the output branch of the power divider and any mismatch will degrade the performance of the phase shifter.

3.6 Actuation System, Fabrication and Packaging

A low-profile magnetic actuator is employed to move the ceramic slab vertically with respect to the microstrip line and changes the gap distance as shown in Fig. 3-14.

It consists of a miniaturized light-weight permanent magnet made of samarium-cobalt with high magnetization, FR4 PCB spacers, a planar 4-layer spiral coil, and a membrane. The miniaturized magnet has a cylinder shape with the diameter of 1.1 mm and the height of 0.5 mm. The membrane is made of a thin polyimide layer which has proper elasticity for movement. The modulus of elasticity of polyimide is 2.5 GPa. The membrane thickness is 150 um. The magnetic actuator utilizes the repulsion and the attraction forces between the permanent magnet and the planar electromagnetic coil to move the ceramic vertically with high

precision. The range of the force is controlled by DC current passing through the electromagnet as shown in Fig. 3-14.

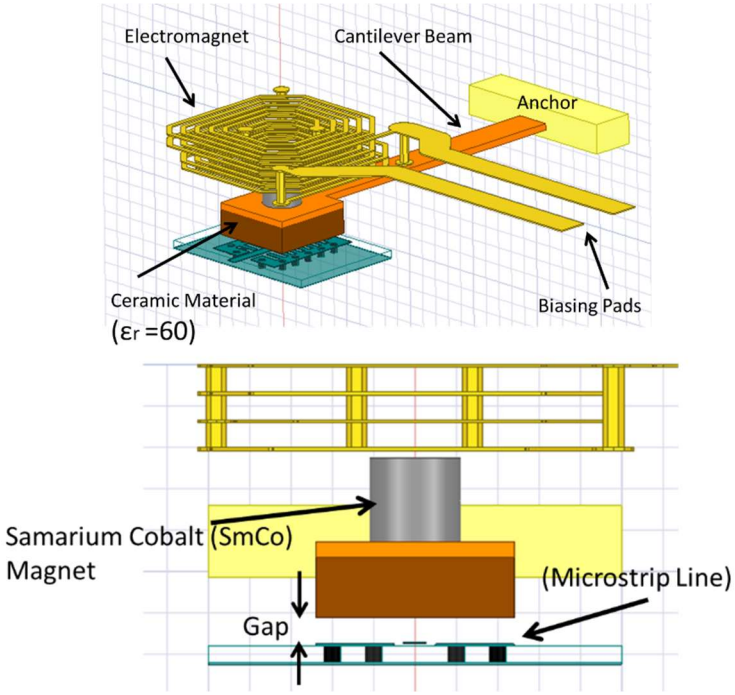

Figure 3-14. The actuation system configuration

By passing electric DC current into the coil, a magnetic field is generated which exerts a magnetic force to the permanent magnet and provides the displacement. The direction of the DC current determines the direction of the vertical displacement. The electromagnet and the cantilever design parameters are optimized such that they are fitted in to a 4×4 array size with the inter-element spacing of 6 mm and have low power consumption. Extensive simulation and analysis by Ansys Maxwell and Ansys Mechanical were performed for characterization and optimization of the actuation system when it is driven by variable DC current source to provide vertical displacements for phase shifting. Simulation results of the interaction between the electromagnet and the magnet shows the generated actuation force range of 0-316 uN when

the DC current changes from 0 mA to the maximum available DC current of 100 mA as shown in Fig. 3-15.

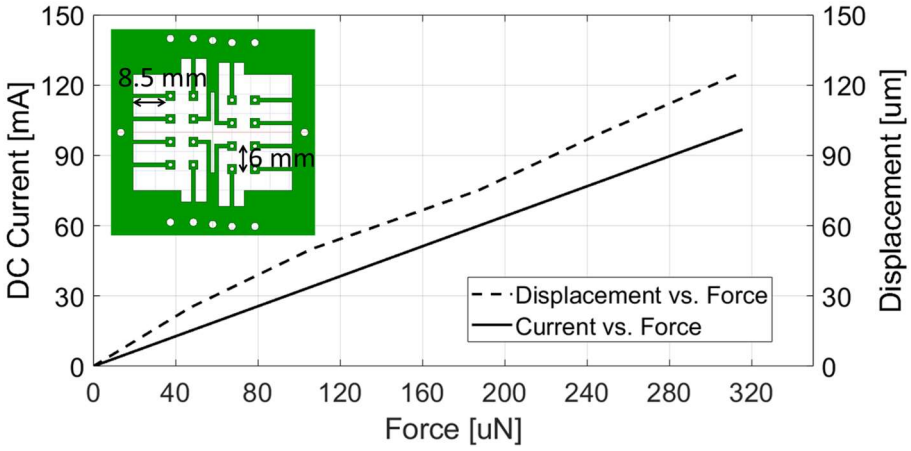

Figure 3-15. The force profile of the actuation system with respect to the DC current and the displacement.

The mechanical simulation results show that the generated force by the actuator provides the vertical displacement range of 0-130 um as shown in Fig. 3-15. The layout of the polyimide membrane sheet with 16 cantilever beams with optimized cantilever length equal to 8.5 mm. Fig. 3-15. Exploded view of the P-PAA system assembly and detailed PCB layer stack-up are shown in Fig. 3-16a and Fig. 3-16b, respectively. The overall thickness becomes 3mm after assembling all parts. Standard multi-layer PCB fabrication processes are used to fabricate the antenna array with back-plane feeding network, and the electromagnet as shown in Fig. 3-17a, and Fig. 3-17d, respectively. Also, membrane sheet, ceramic blocks, and PCB spacers are machined by PCB manufacturer with acceptable accuracy as shown in Fig. 3-17b, and Fig. 3-17c. Magnets and ceramic blocks are adhered to the polyimide sheet using epoxy materials. The magnets must be assembled in such a way that their polarization direction be the same. Fig. 3-17e shows the final P-PAA packaged. Surface-mount RF connector on the RF board is connected to the SMA adaptor through a board-to-board coaxial RF spacer for testing. The

whole system is stacked and connected to a metallic fixture using screws at the edges. The actuation system is tuned by high-precision tunable current sources which are controlled by an Arduino microcontroller unit. Spacer 1 is used between the RF board and the membrane sheet in order to compensate for the ceramic thickness and. Spacer 2 is used to provide enough space for the vertical displacement of the magnet.

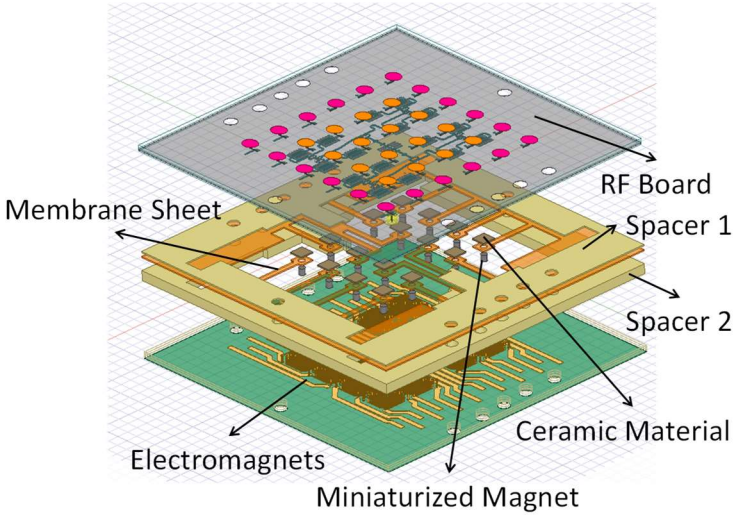

(a)

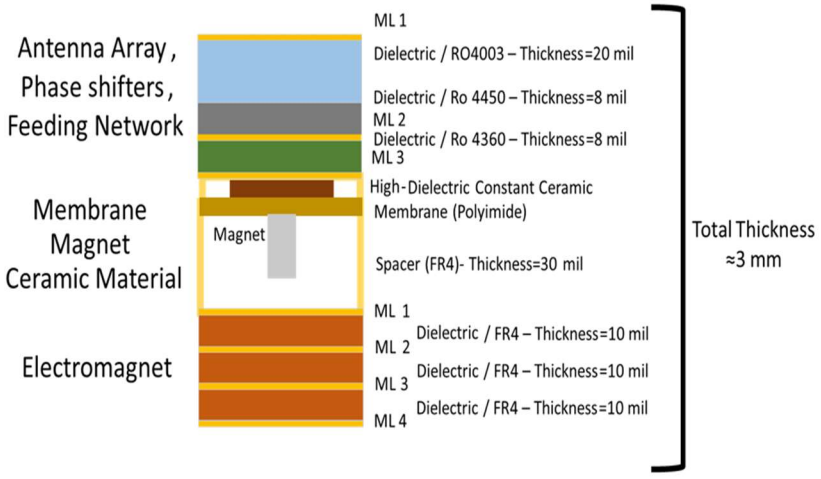

(b)

Figure 3-16. (a) The exploded view and (b) the build-up of the system.

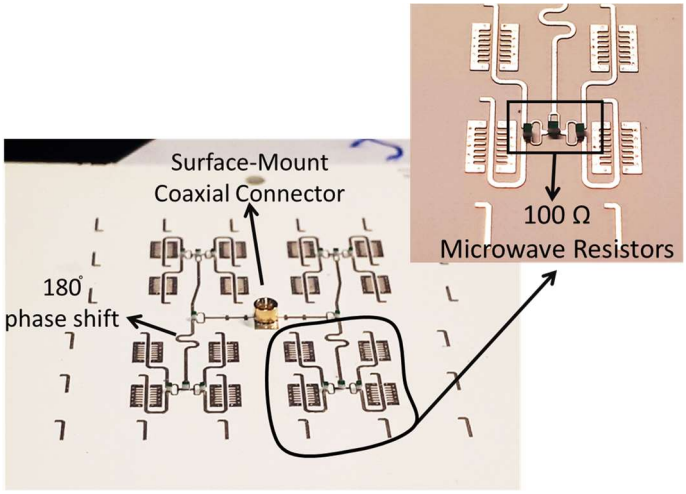

(a)

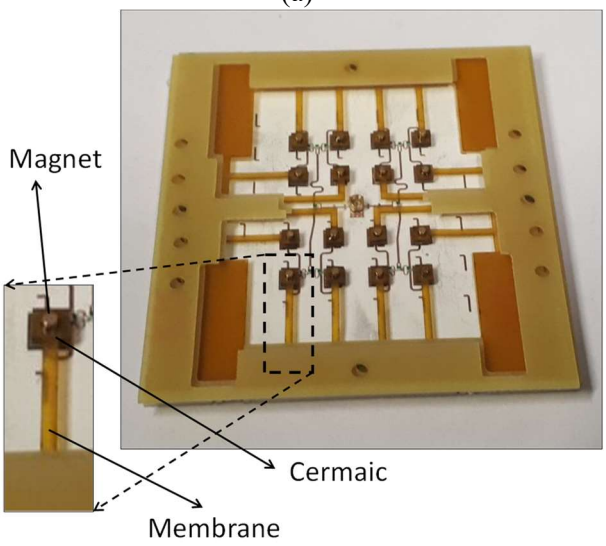

(b)

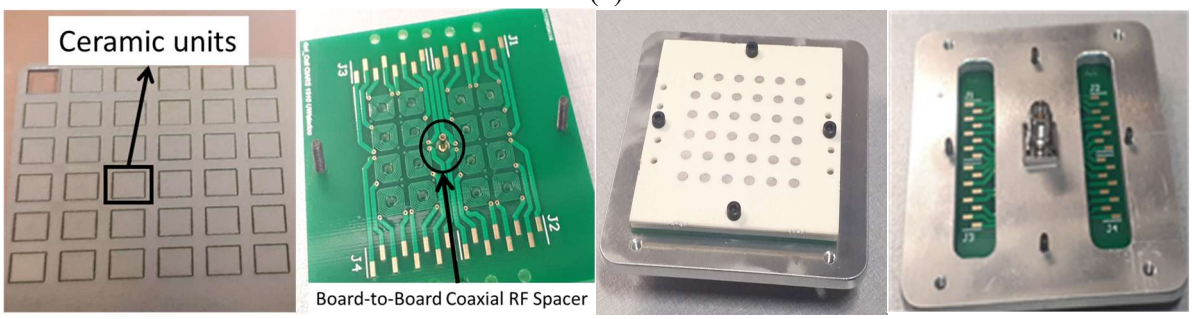

(c) (d) (e) (f)

Figure 3-17. The assembled subsystems: (a) The RF board with the soldered 100 Ω resistors and the surface-mount RF connector. (b) The membrane sheet attached to the magnets and the ceramics with epoxy. (c) Ceramic cuts using laser machine. (d) Electromagnet PCB board stacked with the membrane sheet and the RF board. (e) The whole package.

3.7 Radiation Simulation and Measurement Results

2D beams steering functionality and performance of the P-PAA system is studied by simulation and measurement.

3.7.1 Simulations

For a specific scan angle of (φs,θs), the required phase shift imposed to the antenna element located at (x_{mn},y_{mn}) in a 2D array grid is given by (3-10).

$$\delta\varphi = -k_0(x_{mn}sin(\theta_s)\cos(\varphi_s) + y_{mn}sin(\theta_s)sin(\varphi_s) \quad (3\text{-}10)$$

x_{mn} and y_{mn} are calculated as x_{mn}=(n-1)×dx and y_{mn}=(m-1)×dy respectively, where m and n show the index numbers in x and y directions. In this work, dx and dy are equal to 0.6×λ_0 where λ_0 is the free space wavelength at 30 GHz. In simulation, in order to steer the beam to a specific scan angle of (φs,θs), the required phase shifts distribution over the antenna aperture for all the antenna elements are calculated. Then, the corresponding gap distances required to realize the calculated phase shifts are found using the insertion phase-gap distance (Δφ-Gap) profile shown in Fig. 3-8. It is assumed that the reference state for all the phase shifters corresponds to the gap distance of gap_{ref} = 100 um. Afterwards, all the gap distances are implemented in the ANSYS HFSS simulation model to extract the antenna's main characteristics and compare to the measured results. Fig. 3-18 shows the simulated radiation patterns of the antenna at different scan angles (0º-40º) in two orthogonal planes of X-Z and Y-Z at 29 GHz.

Also, it shows that the co-pol/X-pol discrimination for all the scan angles is more than 10 dB, and side-lobe level (SLL) is less than 6 dB. The SLLs are acceptable for all the scan angles

as tapering is not done to lower the SLLs. The antenna shows the input return loss of more than 10 dB at all the scan angles over the frequency bandwidth of 28-30 GHz. The side-lobe levels are acceptable for all the scan angles as tapering is not done to lower the side-lobe levels.

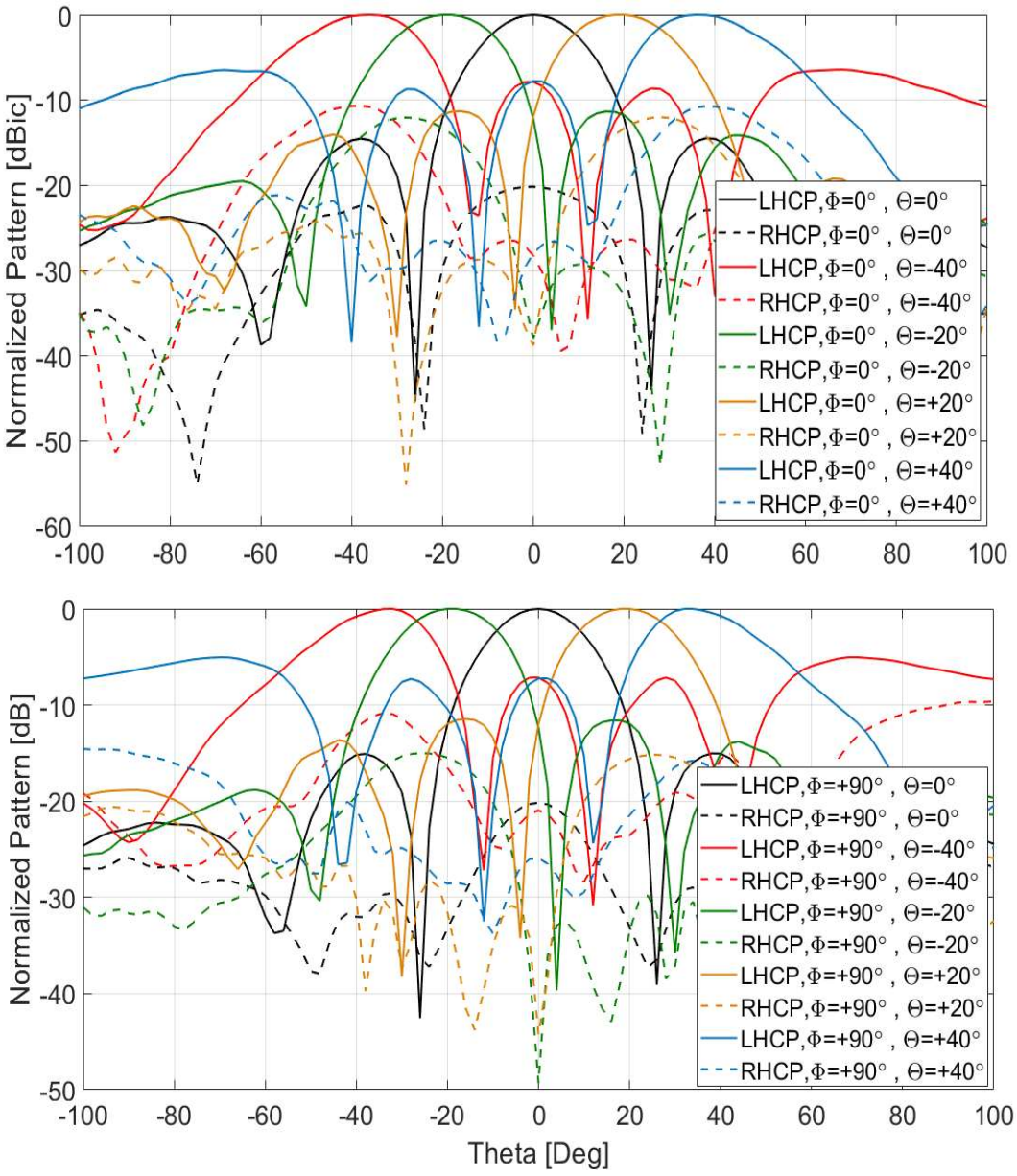

Figure 3-18. The simulation results of the normalized radiation patterns at different scan angles at 29 GHz.

3.7.2 Measurement Results of the Beam Steering

Prior to the radiation pattern measurement, the integrated phase shifters are characterized by near-field planar scanner system. Open-waveguide (OWG) probe is positioned in front of each antenna element, and the transmission coefficient (S21), where port 1 is the input to the antenna systems and port two is the output of the OWG probe) is measured for different DC current states and the corresponding phase shifter is characterized. The distance from the probe to each antenna element is 5 mm for the measurement at 29 GHz. The distance must be as small as possible to make sure that the signal captured by the probe is just coming from the antenna in front of the probe not from the adjacent antenna elements. However, the distance must not be too small that the probe loads the antenna and change its current distribution and input impedance. First, the maximum current is applied to all the actuators in order to place each ceramic at the largest gap distance from the microstrip line (reference state). Then, the current is decreased gradually and the differential insertion phase (with respect to the reference state) is recorded. After reaching the DC current of 0 mA, the direction of the current is reversed to continue the vertical movement down ward. The procedure is repeated for all sixteen phase shifters by moving the probe in front of their corresponding antenna element. It is observed that the maximum measured phase tuning range provided by all of the sixteen phase shifters does not exceed 330º. It is well known that maximum phase tuning range of 330º provides maximum grating lobe-free scan angle of 32º, which is almost proven by measuring maximum scan angle $\theta_{s,max}$=30º as shown in Fig. 3-20 . Although the standalone phase shifter provides more than 380º of the phase shift in measurements, it provides 330º when embedded in the antenna system. This discrepancy is attributed to the inaccuracy in the manual assembly and fabrication process of the proposed prototype. Therefore, more accurate fabrication and

assembly process of the system guarantees accurate initial positioning of the ceramics with respect to the MSL.

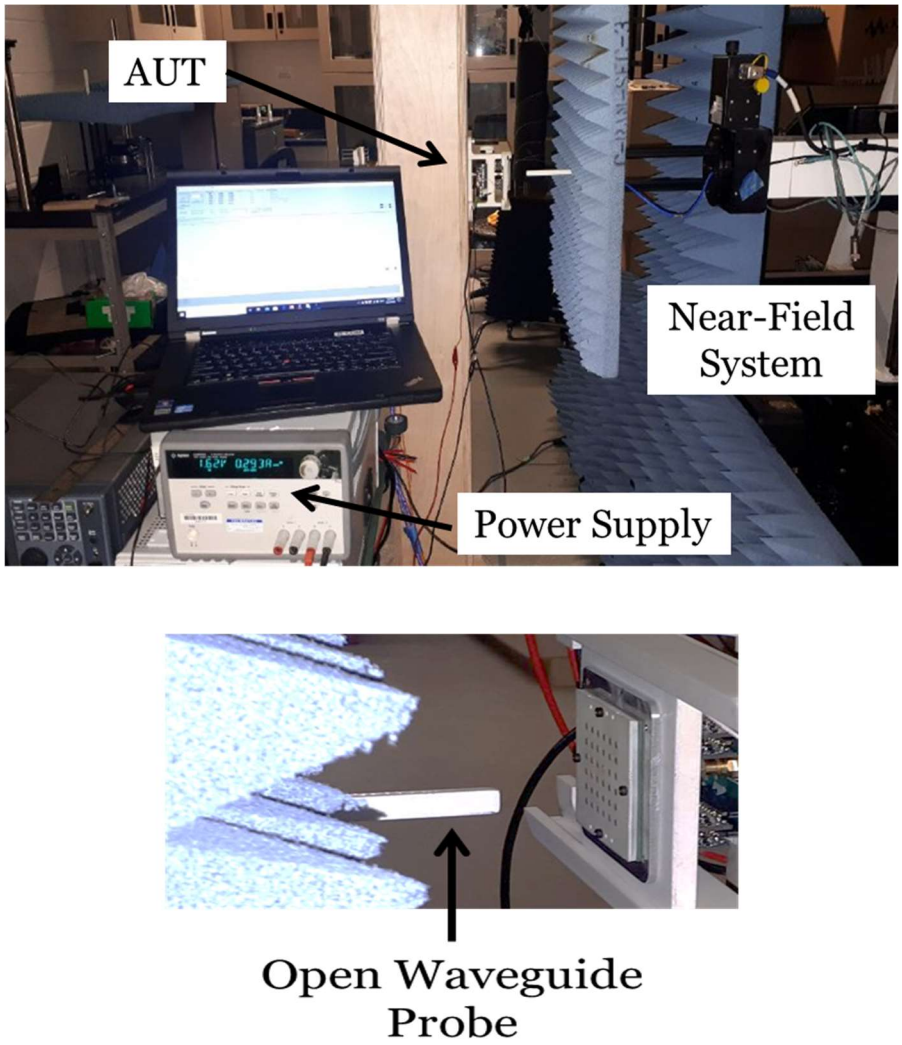

Figure 3-19. The measurement setup.

P-PAA's radiation patterns are measured by a planar nearfield (PNF) measurement system from NSI using the setup shown in Fig. 3-19 at Electromagnetic Radiation Lab (ERL) at the University of Waterloo. An open rectangular waveguide probe scans and measures the phase and amplitude of the antenna near field (NF) over a finite plane. The scanning range of the

scanner is calculated based on the required maximum far-field angle, the size of the antenna and the distance between the probe and the AUT (Antenna Under Test). In this measurement, in order to accurately measure the far field pattern up to +/- 70 degree, the near field data in the area of 0.26 m2 is captured by the probe. The distance between the probe and the antenna is 3 cm. Also, the sampling resolution in both X and Y direction is 0.435 λ. The resolution is calculated based on the Nyquist sampling theorem for the NF (Near Field) to FF (Far-Field) Fourier transform at the highest measurement frequency, which is f = 31 GHz in our measurement. After near field data acquisition, the system post processes the far field data by using a NF-to-FF Fourier transformation. The far field data is collected with angular resolution of $\Delta\theta = \Delta\varphi = 0.5°$. The directivity is then calculated by having the normalized radiated output power which is the integration of the normalized radiation intensity at the far field points.

In testing the radiation pattern at a specific scan angle, DC currents required for realizing the calculated phase shifts distribution over the elements are applied to the actuation system. The measured CP radiation patterns are formed and measured at different scan angles 0º, ±10º, and ±30º for demonstration. A good agreement between simulation and measurement radiation results is observed, especially close to the maximum of main lobes as shown in Fig. 3-20. The antenna radiates LHCP waves with co-pol/X-pol discrimination more than 14 dB at all the steering angles at 29 GHz with SLLs less than -10 dB as shown in Fig. 3-21a. The axial ratio of the radiation pattern with respect to the frequency for different scan angles from both the simulation and measurement results is shown in Fig. 3-21b. The discrepancy between the measured and simulated axial ratios at large scan angles is due to the amplitude imbalance between the antenna elements which is mainly due to higher amplitude variation of the phase shifters for larger phase shifts in measurements. Both directivity (dBic) and efficiency (%) of the proposed P-PAA are measured at different scan angles over the frequency bandwidth of

28-30 GHz as shown in Fig. 3-22. Standard gain horn technique is used for the calculation of the measured efficiency results. The antenna shows measured peak directivity of ~18 dBic with ±0.5 dB difference between the measured and simulated directivity results which is attributed to the amplitude imbalance between the antenna elements. The simulation results show the radiation efficiency of more than 55 % over the operating frequency bandwidth at all the scan angles. Alternatively, the measured radiation efficiency results show the radiation efficiency of more than 26 % as shown in Fig. 3-22. This discrepancy is investigated by characterizing the feeding network loss by simulation and measurement.

Microstrip line (MSL) back-to-back test structure (two-port) with two different lengths, 2 cm and 3 cm are simulated, tested and IL (dB) per unit length (cm) is calculated for each case. It is found that the measured and the simulated attenuation in dB/cm are 0.8 and 0.33, respectively which explains the degradation in the measured efficiency compared to that of the simulation. RO4006 laminate properties and the surface roughness of the metal layer at Ka-band are the factors which could not be modeled in simulation. The input return loss of the antenna system is measured at different scanning angles and the results are shown in Fig. 3-23. The antenna system maintains the input return loss of more than 10 dB over the operating frequency bandwidth of 28-30 GHz. It is worth mentioning that the actuation system consumes the maximum DC power ~ 60 mW by each phase shifter. Table VII compares the proposed P-PAA to existing systems published in the literature. The proposed system not only provides two-dimensional beam steering capability, it shows relatively higher efficiency.

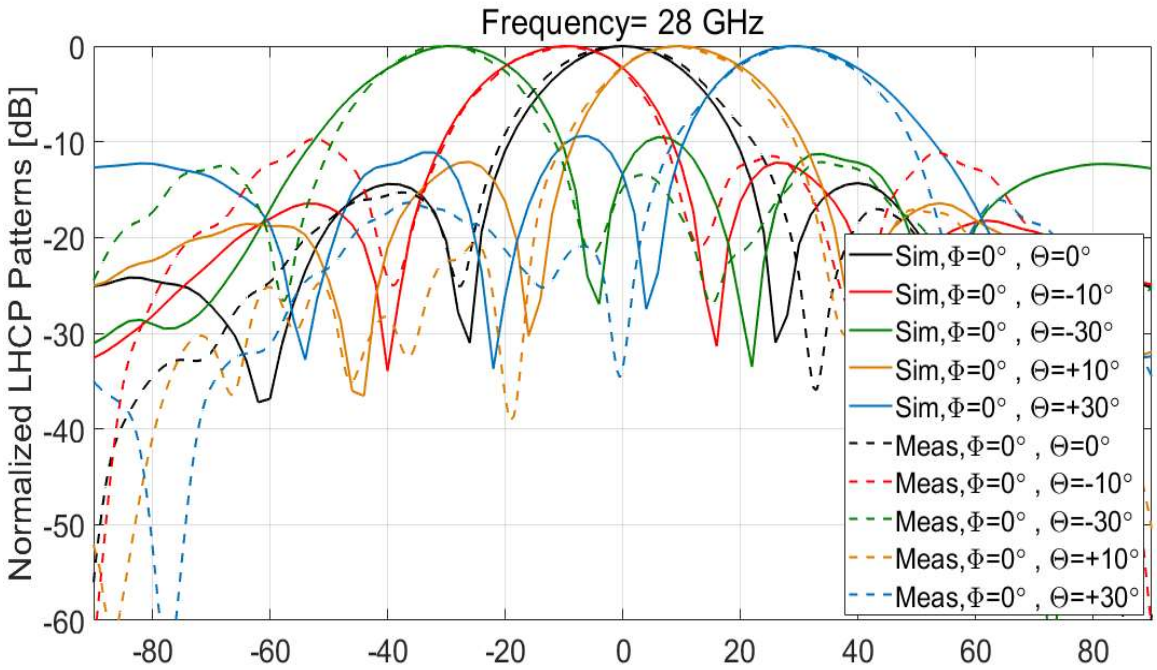
Frequency= 28 GHz
Normalized LHCP Patterns [dB]
0
-10
-20
-30
-40
-50
-60
-80
-60
-40
-20
0
20
40
60
80
Sim,Φ=0° , Θ=0°
Sim,Φ=0° , Θ=-10°
Sim,Φ=0° , Θ=-30°
Sim,Φ=0° , Θ=+10°
Sim,Φ=0° , Θ=+30°
Meas,Φ=0° , Θ=0°
Meas,Φ=0° , Θ=-10°
Meas,Φ=0° , Θ=-30°
Meas,Φ=0° , Θ=+10°
Meas,Φ=0° , Θ=+30°

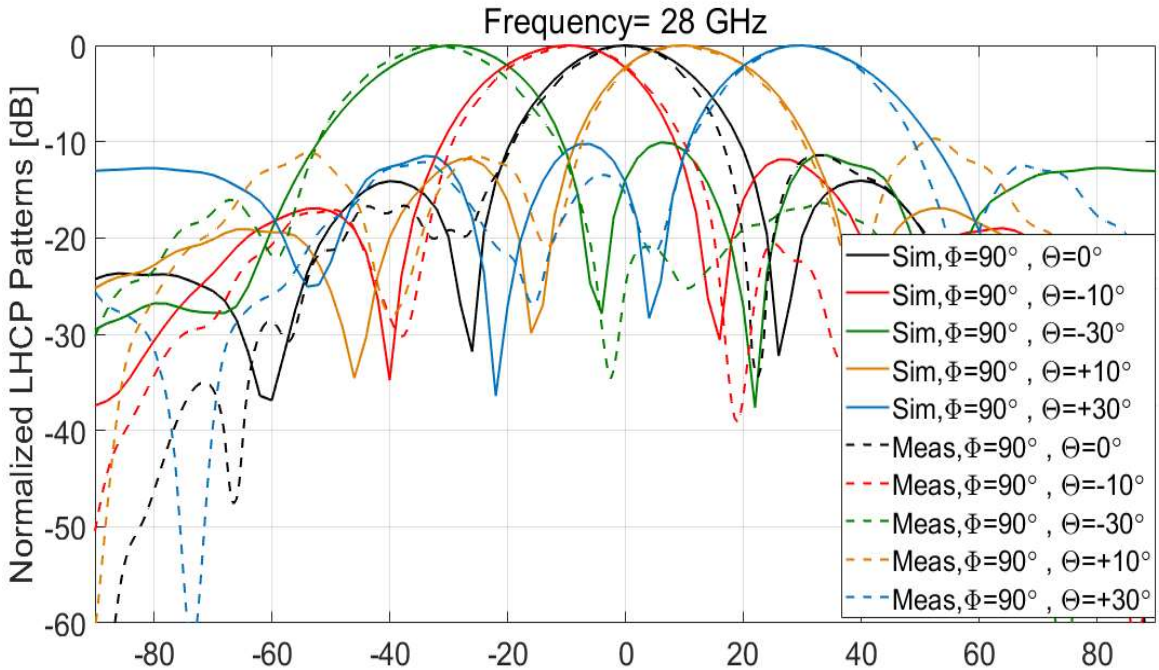
Frequency= 28 GHz
Normalized LHCP Patterns [dB]
0
-10
-20
-30
-40
-50
-60
-80
-60
-40
-20
0
20
40
60
80
Sim,Φ=90° , Θ=0°
Sim,Φ=90° , Θ=-10°
Sim,Φ=90° , Θ=-30°
Sim,Φ=90° , Θ=+10°
Sim,Φ=90° , Θ=+30°
Meas,Φ=90° , Θ=0°
Meas,Φ=90° , Θ=-10°
Meas,Φ=90° , Θ=-30°
Meas,Φ=90° , Θ=+10°
Meas,Φ=90° , Θ=+30°

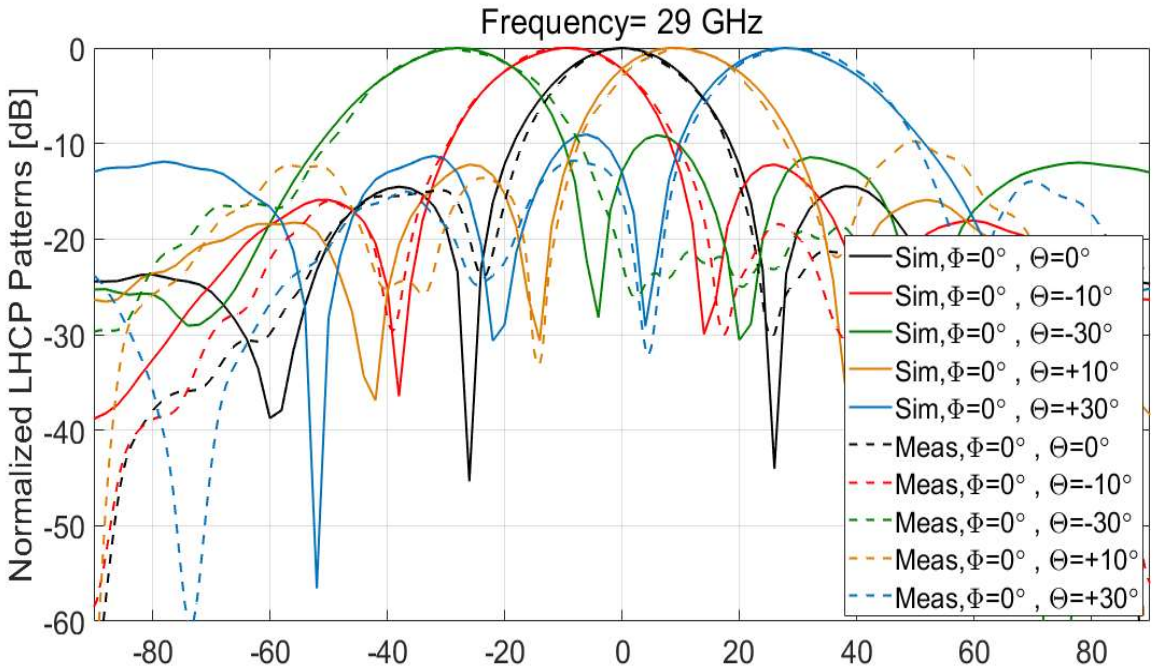
Frequency= 29 GHz
Normalized LHCP Patterns [dB]
0
-10
-20
-30
-40
-50
-60
-80
-60
-40
-20
0
20
40
60
80
Sim,Φ=0° , Θ=0°
Sim,Φ=0° , Θ=-10°
Sim,Φ=0° , Θ=-30°
Sim,Φ=0° , Θ=+10°
Sim,Φ=0° , Θ=+30°
Meas,Φ=0° , Θ=0°
Meas,Φ=0° , Θ=-10°
Meas,Φ=0° , Θ=-30°
Meas,Φ=0° , Θ=+10°
Meas,Φ=0° , Θ=+30°

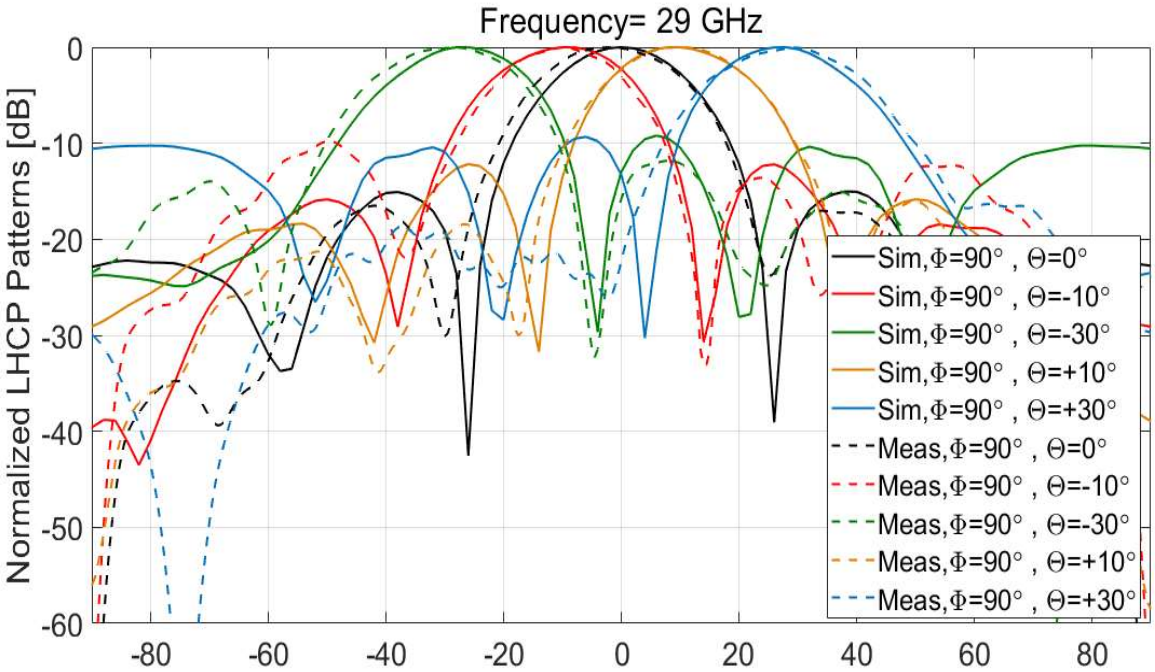
Frequency= 29 GHz
Normalized LHCP Patterns [dB]
0
-10
-20
-30
-40
-50
-60
-80
-60
-40
-20
0
20
40
60
80
Sim,Φ=90° , Θ=0°
Sim,Φ=90° , Θ=-10°
Sim,Φ=90° , Θ=-30°
Sim,Φ=90° , Θ=+10°
Sim,Φ=90° , Θ=+30°
Meas,Φ=90° , Θ=0°
Meas,Φ=90° , Θ=-10°
Meas,Φ=90° , Θ=-30°
Meas,Φ=90° , Θ=+10°
Meas,Φ=90° , Θ=+30°

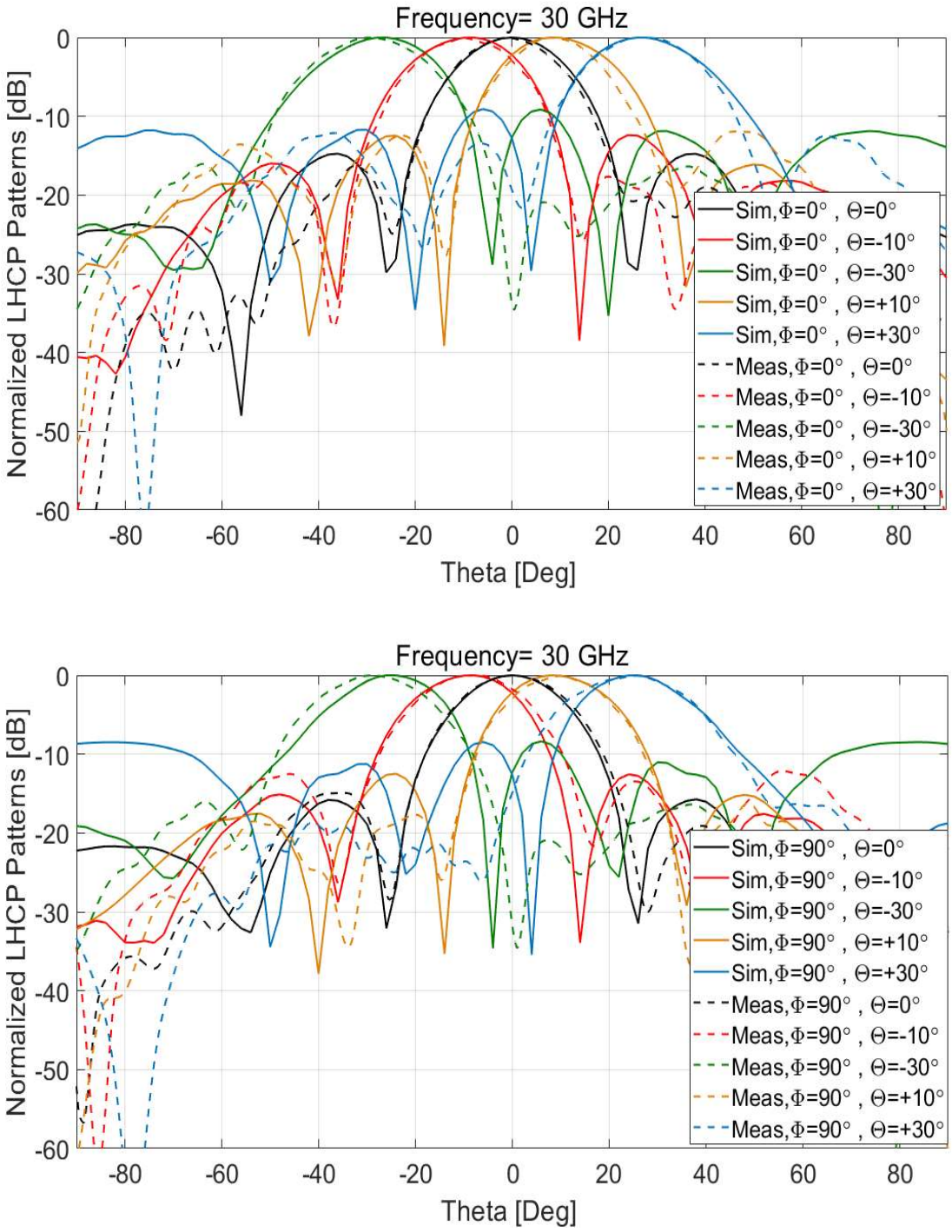

Figure 3-20. The measurement results of the radiation pattern for different scan angles in two planes of X-Z and Y-Z.

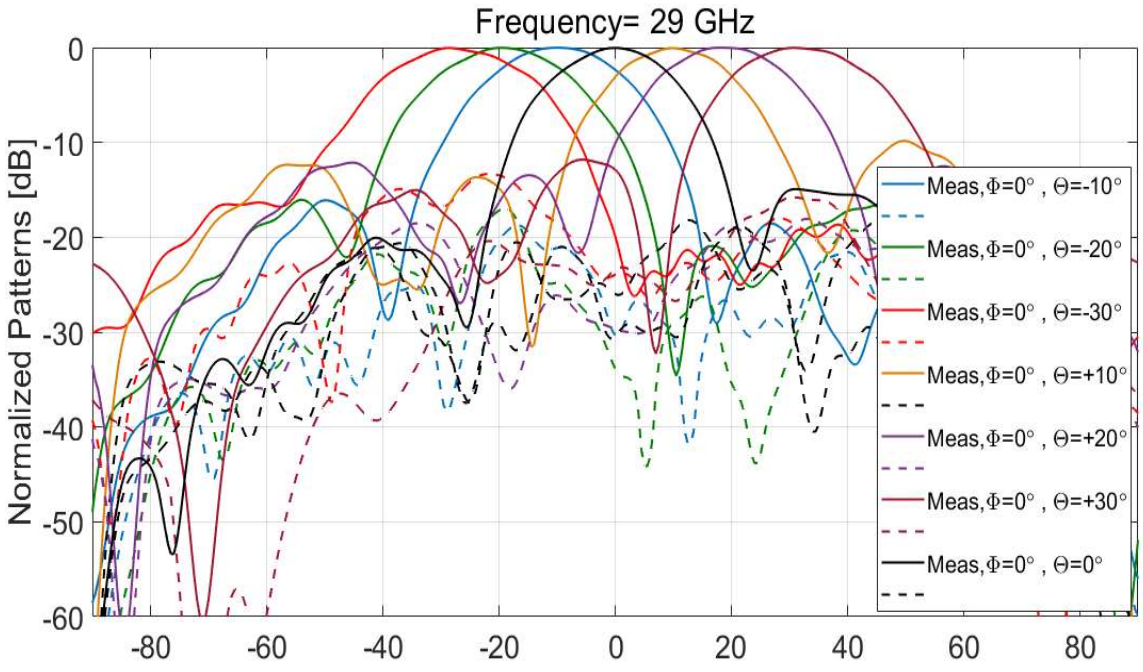

(a)

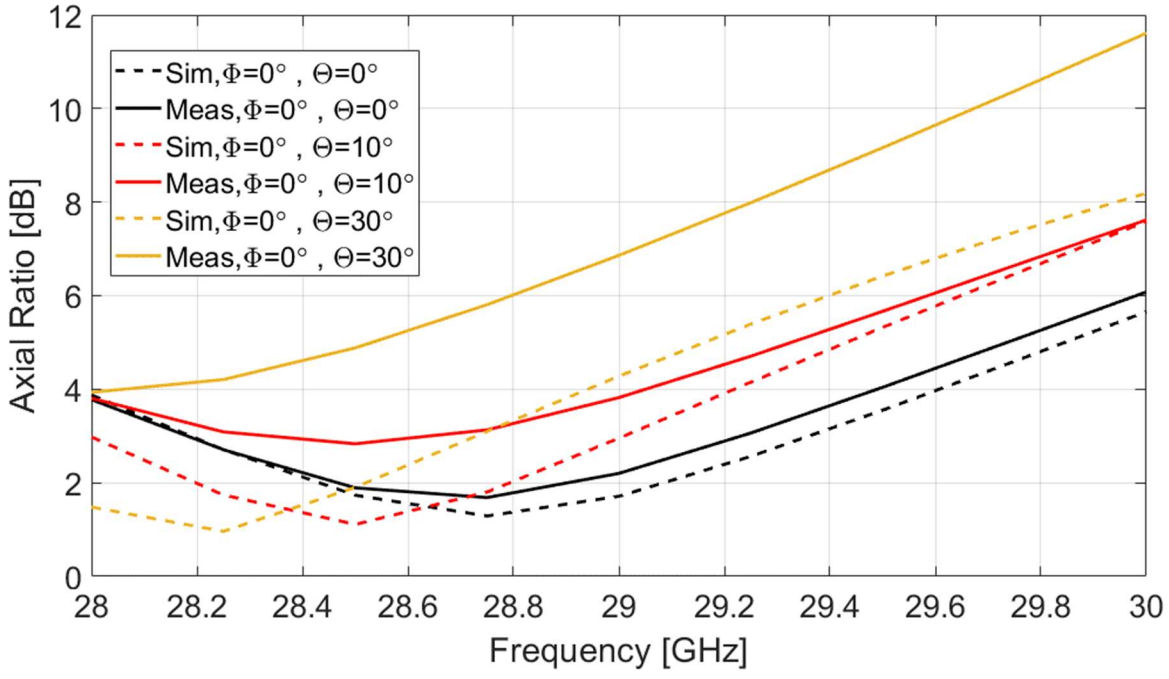

(b)

Figure 3-21. (a)The measurement results of the Co-pol (LHCP) and X-pol (RHCP) radiation patterns at the plane of X-Z at 29 GHz. (b) Axial Ratio over frequency for different scan angles.

TABLE VII
PERFORMANCE COMPARISON OF THE PROPOSED ANTENNA SYSTEM WITH STATE-OF-THE-ART PASSIVE PHASED-ARRAY ANTENNA SYSTEMS

Reference	f_0 [GHz]	Phase shifter Technology	Array Size	Beam steering Coverage	Gain [dBi] (Boresight)	Efficiency (%) (Boresight)	Polarization	Biasing *
This work	29	MEMS-Based	4×4	±30° / 2D	15.8	58	CP	0 mA- 100 mA (0 v - 0.6 v)
[63]	30	MEMS-Based	1×4	±30° / 1D	7.4	60	LP	0 mA- 100 mA (0 v - 0.6 v)
[66]	30	MEMS-Based	1×4	±38° / 1D	8.2	48	CP	0 mA- 100 mA (0 v - 0.6 v)
[72]	14	RF MEMS	2×2	-4° to 8° / 1D	7.75	33	LP	-
[73]	14.6	RF MEMS	1×4	±14° / 1D	-	-	LP	-
[52]	12.8	BST Ferroelectric	4×4	±25° / 2D	8.1	7.76	LP	0 v - 180 v
[71]	13.2	Ferrite	2×3	±19° / 1D	4.9	-	LP	0 mA - 200 mA**
[69]	5.5	Varactor Diode	1×4	±45° / 1D	11	-	LP	0 v- 20 v
[54]	29	Liquid Crystal	2×2	±25° / 2D	5.9	-	LP	0 v - 15 v
[70]	28.4	Liquid Crystal	1×4	±40° / 2D	3.5	8.6	LP	0 v-5 v

* The biasing is required for each phase shifter in order to provide its tunability.

** The required range of voltages in not reported for generation of the required current.

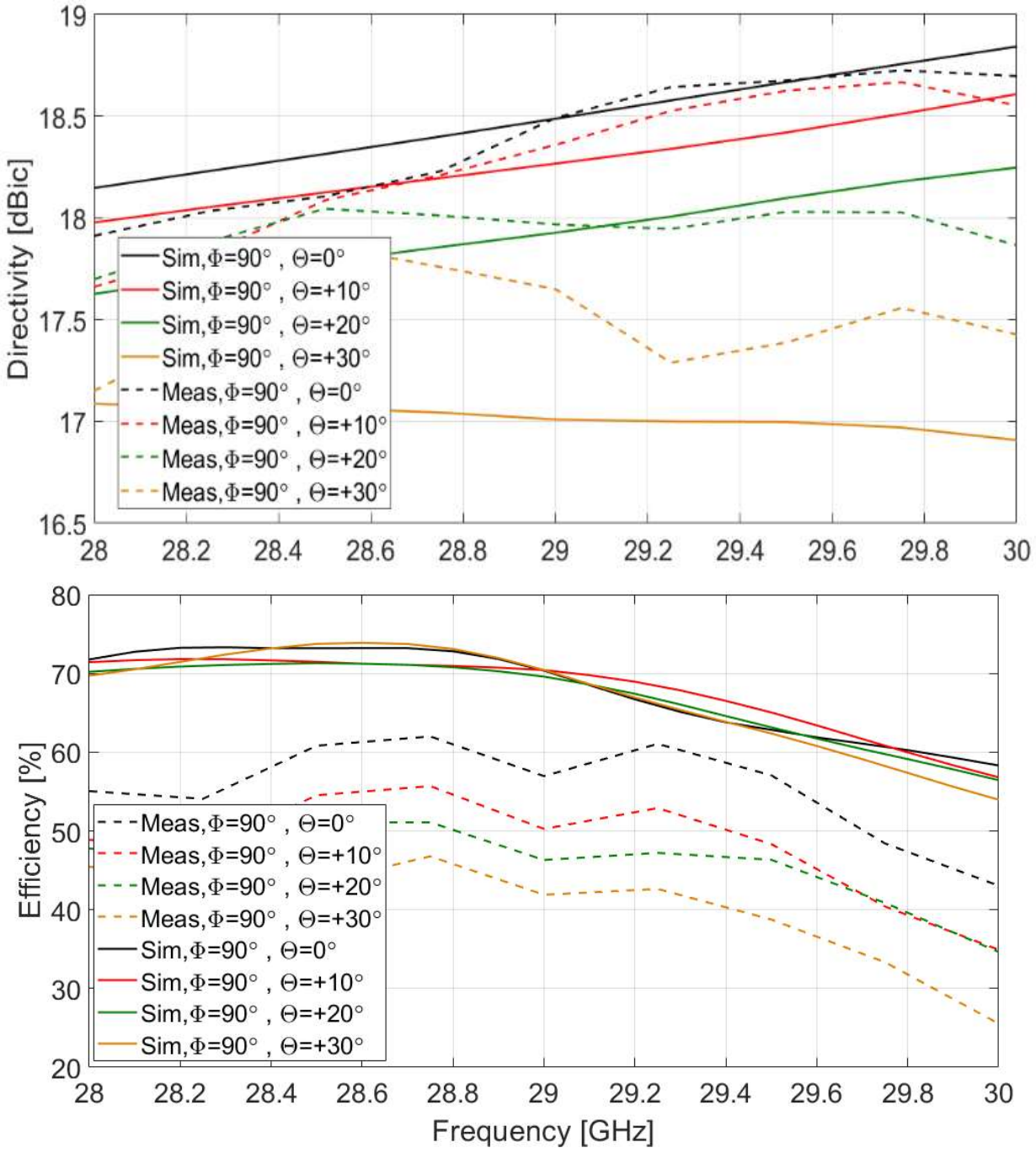

Figure 3-22. The simulation and measurement results of the peak directivity and the radiation efficiency for different scan angles.

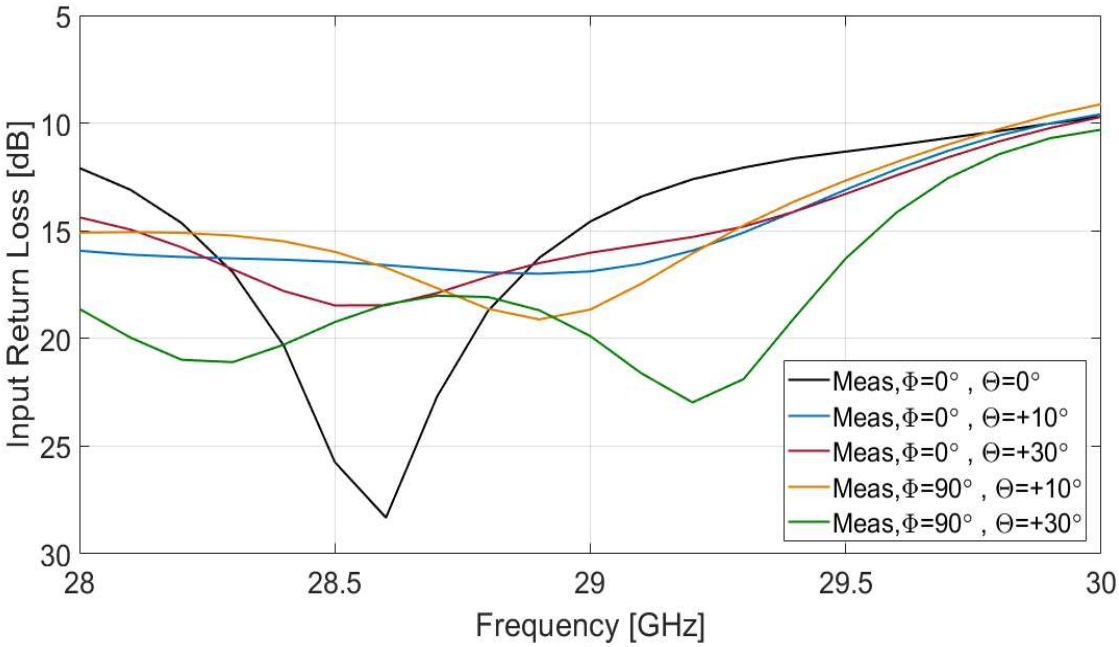

Figure 3-23. The measured input return loss for different scan angles.

3.8 Conclusion

In this article, the design and implementation aspects of a 4×4 antenna array with integrated passive beamformer for low-cost and efficient millimeter wave applications is presented. The phase shifter's operational principle and actuation mechanism are discussed in this thesis. Slow-wave structure is employed to shrink the size of the phase shifter. The simulation and measurement results of the phase shifter are presented.

Measurement results show the maximum insertion loss of 2.2 dB in all the tuning states and the insertion loss variation is 1.2 dB. Also, it provides 380º of the phase tuning range in a compact footprint area of 2.4 mm × 3 mm. 2D P-PAA is designed, simulated and measured over the operating band.

Measurement results show the antenna‘s main beam can be steered over an angular range of ±30º in both elevation and azimuth planes.. The operating frequency bandwidth of the system ranges from 28-30 GHz. The antenna’s main characteristics, such as radiation pattern, directivity, efficiency, and reflection coefficient are measured and presented in this thesis

Chapter 4- Concluding Remarks and Future Works

4.1 Summary and Contributions

In this thesis, two different architectures for phased-array AiP are presented. The first architecture is a 4×4 active transmit phased-array AiP with polarization control at Ka-band. The second architecture is a 4×4 bi-directional antenna array with integrated passive beamformer with left-handed circular polarization (LHCP) radiation.

In chapter II, a 4×4 active transmit phased-array AiP with polarization control at Ka-band is discussed. The proposed active AiP is modular and scalable and is able to be employed as the unit cell for a large-scale phased array antenna system.

The proposed AiP provides 42 dB of active gain at the boresight. The effective isotropic radiated power (EIRP) of the current module is 41 dBm at the 1-dB compression point of the active beamformer chips and it consumes 2.6 W of DC power when the system radiates left-handed circular polarization.

Calibration and radiation pattern measurement of the system is also discussed and the measurement results for a case of left-handed circularly polarized (LHCP) radiation is presented.

The contribution of this work includes the modular and scalable implementation of the system as well introducing a novel interconnect for connecting of the phased-array unit cell with the back-plane power splitting network.

In chapter III, a 4×4 bi-directional antenna array with integrated passive beamformer with left-handed circular polarization (LHCP) radiation is presented. The design and implementation aspects of a 4×4 antenna array with integrated passive beamformer for low-cost and efficient millimeter wave applications is presented.

The phase shifter's operational principle and actuation mechanism are discussed in detail. Slow-wave structure is employed to shrink the size of the phase shifter. The simulation and measurement results of the phase shifter are presented.

Measurement results show the maximum insertion loss of 2.2 dB in all the tuning states and the insertion loss variation is 1.2 dB. Also, it provides 380º of the phase tuning range in a compact footprint area of 2.4 mm × 3 mm. 2D P-PAA is designed, simulated and measured over the operating band.

Measurement results show the beam steering range of ±30º in both elevation and azimuth planes. The operating frequency bandwidth of the system ranges from 28-30 GHz to provide co-pol/X-pol discrimination of more than 12 dB for all the steering angles. The simulation results show the peak gain of 15.8 dBic and the radiation efficiency of 58% at boresight at the frequency of 29 GHz. The gain drops by 2dB when the scan angles reaches the maximum.

The contribution of this work includes implementing a compact, high-performance bi-directional passive beamformer.

4.2 Future Work

- **Over-the-air modulated signal evaluation transmitted through the proposed active phased-array antenna.**
- **Implementation of a large-scale phased-array antenna system using the proposed active phased-array antenna unit cell.**
- **The monolithic integration of the proposed passive phased-array antenna.**
- **Adding amplitude control functionality to the proposed passive phased-array antenna.**

References:

1. Mohammad Fakharzadeh Jahromi (2009). Optical and Microwave Beamforming for Phased Array Antennas. UWSpace.

2. Stutzman, Warren L., and Gary A. Thiele. Antenna theory and design. John Wiley & Sons, 2012.

3. Yu, Yikun, Peter GM Baltus, and Arthur HM Van Roermund. Integrated 60GHz RF beamforming in CMOS. Springer Science & Business Media, 2011.

4. Herd, Jeffrey S., and M. David Conway. "The evolution to modern phased array architectures." Proceedings of the IEEE 104.3 (2015): 519-529.

5. Rebeiz, Gabriel M., and Kwang-Jin Koh. "Silicon RFICs for phased arrays." IEEE Microwave Magazine 10.3 (2009): 96-103.

6. Sadhu, Bodhisatwa, et al. "A 28-GHz 32-element TRX phased-array IC with concurrent dual-polarized operation and orthogonal phase and gain control for 5G communications." IEEE Journal of Solid-State Circuits 52.12 (2017): 3373-3391.

7. Kopp, Bruce A., Michael Borkowski, and George Jerinic. "Transmit/receive modules." IEEE Transactions on Microwave Theory and Techniques 50.3 (2002): 827-834.

8. Wallace, Jack, Harold Redd, and Robert Furlow. "Low cost MMIC DBS chip sets for phased array applications." 1999 IEEE MTT-S International Microwave Symposium Digest (Cat. No. 99CH36282). Vol. 2. IEEE, 1999.

9. Van Vliet, F. E., and A. De Boer. "Fully-integrated core chip for X-band phased array T/R modules." 2004 IEEE MTT-S International Microwave Symposium Digest (IEEE Cat. No. 04CH37535). Vol. 3. IEEE, 2004.

10. Hashemi, Hossein, Xiang Guan, and Ali Hajimiri. "A fully integrated 24 GHz 8-path phased-array receiver in silicon." 2004 IEEE International Solid-State Circuits Conference (IEEE Cat. No. 04CH37519). IEEE, 2004.

11. Natarajan, Arun, Abbas Komijani, and Ali Hajimiri. "A 24 GHz phased-array transmitter in 0.18/spl mu/m CMOS." ISSCC. 2005 IEEE International Digest of Technical Papers. Solid-State Circuits Conference, 2005.. IEEE, 2005.

12. Sadhu, Bodhisatwa, Xiaoxiong Gu, and Alberto Valdes-Garcia. "The More (Antennas), the Merrier: A Survey of Silicon-Based mm-Wave Phased Arrays Using Multi-IC Scaling." IEEE Microwave Magazine 20.12 (2019): 32-50.

13. Tousi, Yahya, and Ehsan Afshari. "14.6 A scalable THz 2D phased array with+ 17dBm of EIRP at 338GHz in 65nm bulk CMOS." 2014 IEEE International Solid-State Circuits Conference Digest of Technical Papers (ISSCC). IEEE, 2014.

14. Natarajan, Arun, et al. "A fully-integrated 16-element phased-array receiver in SiGe BiCMOS for 60-GHz communications." IEEE Journal of Solid-State Circuits 46.5 (2011): 1059-1075.

15. Valdes-Garcia, Alberto, et al. "A fully integrated 16-element phased-array transmitter in SiGe BiCMOS for 60-GHz communications." IEEE journal of solid-state circuits 45.12 (2010): 2757-2773.

16. Gu, Xiaoxiong, et al. "W-band scalable phased arrays for imaging and communications." IEEE communications magazine 53.4 (2015): 196-204.

17. Rebeiz, Gabriel M., Guan-Leng Tan, and Joseph S. Hayden. "RF MEMS phase shifters: Design and applications." IEEE microwave magazine 3.2 (2002): 72-81.

18. HUSSAM AL-SAEDI (2018). A Modular and Scalable Architecture for Millimeter-Wave Beam-forming Antenna Systems. UWSpace.

19. Nikfalazar, Mohammad, et al. "Two-dimensional beam-steering phased-array antenna with compact tunable phase shifter based on BST thick films." IEEE Antennas and Wireless Propagation Letters 16 (2016): 585-588.

20. Yang, Lu, et al. "18–40-GHzBeam-shaping/steering phased antenna array system using Fermi antenna." IEEE transactions on microwave theory and techniques 56.4 (2008): 767-773.

21. Van Caekenberghe, Koen, et al. "Ka-band MEMS TTD passive electronically scanned array (ESA)." 2006 IEEE Antennas and Propagation Society International Symposium. IEEE, 2006.

22. Rebeiz, Gabriel M. RF MEMS: theory, design, and technology. John Wiley & Sons, 2004.

23. Topalli, Kagan, et al. "A monolithic phased array using 3-bit distributed RF MEMS phase shifters." IEEE Transactions on Microwave Theory and Techniques 56.2 (2008): 270-277.

24. Z. R. Omam et al., "Ka-Band Passive Phased-Array Antenna With Substrate Integrated Waveguide Tunable Phase Shifter," in IEEE Transactions on Antennas and Propagation.

25. Natarajan, Arun, Abbas Komijani, and Ali Hajimiri. "A fully integrated 24-GHz phased-array transmitter in CMOS." IEEE Journal of solid-state circuits 40.12 (2005): 2502-2514.

26. Sarkas, Ioannis. Analysis and Design of W-Band Phase Shifters. Diss. 2010.

27. F. De Flaviis, N. G. Alexopoulos and O. M. Stafsudd, "Planar microwave integrated phase-shifter design with high purity ferroelectric material," in IEEE Transactions on Microwave Theory and Techniques, vol. 45, no. 6, pp. 963-969, June 1997.

28. Garg, Robin, and Arun S. Natarajan. "A 28-GHz low-power phased-array receiver front-end with 360° RTPS phase shift range." IEEE Transactions on Microwave Theory and Techniques 65.11 (2017): 4703-4714.

29. Koh, Kwang-Jin, and Gabriel M. Rebeiz. "0.13-$\mu $ m CMOS phase shifters for X-, Ku-, and K-band phased arrays." IEEE Journal of Solid-State Circuits 42.11 (2007): 2535-2546.

30. Lee, Wooram, and Alberto Valdes-Garcia. "Continuous True-Time Delay Phase Shifter Using Distributed Inductive and Capacitive Miller Effect." IEEE Transactions on Microwave Theory and Techniques 67.7 (2019): 3053-3063.

31. Jost, M., et al. "Continuously tuneable liquid crystal based stripline phase shifter realised in LTCC technology." 2015 European Microwave Conference (EuMC). IEEE, 2015.

32. Compact, Low-Loss, Wideband, and High-Power Handling Phase Shifters With Piezoelectric Transducer-Controlled Metallic Perturber

33. Z. Briqech, A. Sebak and T. A. Denidni, "Low-Cost Wideband mm-Wave Phased Array Using the Piezoelectric Transducer for 5G Applications," in IEEE

Transactions on Antennas and Propagation, vol. 65, no. 12, pp. 6403-6412, Dec. 2017.

34. H. Al-Saedi et al., "A Low-Cost Ka-Band Circularly Polarized Passive Phased-Array Antenna for Mobile Satellite Applications," in IEEE Transactions on Antennas and Propagation, vol. 67, no. 1, pp. 221-231, Jan. 2019.

35. N. Ranjkesh, M. Basha, A. Abdellatif, S. Gigoyan and S. Safavi-Naeini, "Millimeter-Wave Tunable Phase Shifter on Silicon-on-Glass Technology," in IEEE Microwave and Wireless Components Letters, vol. 25, no. 7, pp. 451-453, July 2015.

36. T. S. D. Cheung and J. R. Long, "Shielded passive devices for silicon-based monolithic microwave and millimeter-wave integrated circuits," in IEEE Journal of Solid-State Circuits, vol. 41, no. 5, pp. 1183-1200, May 2006.

37. S. Seki and H. Hasegawa, "Cross-tie slow-wave coplanar waveguide on semi-insulating GaAs substrates," in Electronics Letters, vol. 17, no. 25, pp. 940-941, 10 December 1981.

38. Sadhu, Bodhisatwa, Xiaoxiong Gu, and Alberto Valdes-Garcia. "The More (Antennas), the Merrier: A Survey of Silicon-Based mm-Wave Phased Arrays Using Multi-IC Scaling." IEEE Microwave Magazine 20.12 (2019): 32-50.

39. Sadhu, Bodhisatwa, et al. "A 28-GHz 32-element TRX phased-array IC with concurrent dual-polarized operation and orthogonal phase and gain control for 5G communications." IEEE Journal of Solid-State Circuits 52.12 (2017): 3373-3391.

40. K. Bhattacharyya, Phased Array Antennas—Floquet Analysis, Synthesis, BFNs and Active Array Systems. Hoboken, NJ, USA: Wiley, 2006.

41. Rebeiz, Gabriel M., Guan-Leng Tan, and Joseph S. Hayden. "RF MEMS phase shifters: Design and applications." IEEE microwave magazine 3.2 (2002): 72-81.

42. Herd, Jeffrey S., and M. David Conway. "The evolution to modern phased array architectures." Proceedings of the IEEE 104.3 (2015): 519529.

43. E. Baladi, M. Y. Xu, N. Faria, J. Nicholls and S. V. Hum, "Dual-Band Circularly Polarized Fully Reconfigurable Reflectarray Antenna for Satellite Applications in the Ku Band," in IEEE Transactions on Antennas and Propagation, doi: 10.1109/TAP.2021.3090577.

44. K. Klionovski, M. S. Sharawi and A. Shamim, "A Dual-PolarizationSwitched Beam Patch Antenna Array for Millimeter-Wave Applications," in IEEE Transactions on Antennas and Propagation, vol. 67, no. 5, pp. 3510-3515, May 2019, doi: 10.1109/TAP.2019.2900438.

45. Y. Hu, J. Zhan, Z. H. Jiang, C. Yu and W. Hong, "An Orthogonal Hybrid Analog–Digital Multibeam Antenna Array for Millimeter-Wave Massive MIMO Systems," in IEEE Transactions on Antennas and Propagation, vol. 69, no. 3, pp. 1393-1403, March 2021, doi: 10.1109/TAP.2020.3016400.

46. Natarajan, Arun, Abbas Komijani, and Ali Hajimiri. "A 24 GHz phasedarray transmitter in 0.18/spl mu/m CMOS." ISSCC. 2005 IEEE International Digest of Technical Papers. Solid-State Circuits Conference, 2005.. IEEE, 2005.

47. Rebeiz, Gabriel M., and Kwang-Jin Koh. "Silicon RFICs for phased arrays." IEEE Microwave Magazine 10.3 (2009): 96-103.

48. G. Gültepe, T. Kanar, S. Zihir and G. M. Rebeiz, "A 1024-Element KuBand SATCOM Dual-Polarized Receiver With >10-dB/K G/T and Embedded Transmit

Rejection Filter," in IEEE Transactions on Microwave Theory and Techniques, vol. 69, no. 7, pp. 3484-3495, July 2021, doi: 10.1109/TMTT.2021.3073321.

49. G. Gültepe, T. Kanar, S. Zihir and G. M. Rebeiz, "A 1024-Element KuBand SATCOM Phased-Array Transmitter With 45-dBW SinglePolarization EIRP," in IEEE Transactions on Microwave Theory and Techniques, doi: 10.1109/TMTT.2021.3075678.

50. Jakoby, Rolf, Alexander Gaebler, and Christian Weickhmann. 2020. "Microwave Liquid Crystal Enabling Technology for Electronically Steerable Antennas in SATCOM and 5G Millimeter-Wave Systems" Crystals 10, no. 6: 514.

51. H. Krishnaswamy, A. Valdes-Garcia and J. Lai, "A silicon-based, allpassive, 60 GHz, 4-element, phased-array beamformer featuring a differential, reflection-type phase shifter," 2010 IEEE International Symposium on Phased Array Systems and Technology, 2010, pp. 225232, doi: 10.1109/ARRAY.2010.5613365.

52. M. Nikfalazar et al., "Two-Dimensional Beam-Steering Phased-Array Antenna With Compact Tunable Phase Shifter Based on BST Thick Films," in IEEE Antennas and Wireless Propagation Letters, vol. 16, pp. 585-588, 2017, doi: 10.1109/LAWP.2016.2591078.

53. O. H. Karabey, A. Gaebler, S. Strunck and R. Jakoby, "A 2-D Electronically Steered Phased-Array Antenna With 2$\,\times\,$ 2 Elements in LC Display Technology," in IEEE Transactions on Microwave Theory and Techniques, vol. 60, no. 5, pp. 1297-1306, May 2012, doi: 10.1109/TMTT.2012.2187919.

54. Franc, O. H. Karabey, G. Rehder, E. Pistono, R. Jakoby and P. Ferrari, "Compact and Broadband Millimeter-Wave Electrically Tunable Phase Shifter Combining

Slow-Wave Effect With Liquid Crystal Technology," in IEEE Transactions on Microwave Theory and Techniques, vol. 61, no. 11, pp. 3905-3915, Nov. 2013, doi: 10.1109/TMTT.2013.2282288.

55. R. Garg and A. S. Natarajan, "A 28-GHz Low-Power Phased-Array Receiver Front-End With 360° RTPS Phase Shift Range," in IEEE Transactions on Microwave Theory and Techniques, vol. 65, no. 11, pp. 4703-4714, Nov. 2017, doi: 10.1109/TMTT.2017.2707414.

56. B. Min and G. M. Rebeiz, "Single-Ended and Differential Ka-Band BiCMOS Phased Array Front-Ends," in IEEE Journal of Solid-State Circuits, vol. 43, no. 10, pp. 2239-2250, Oct. 2008, doi: 10.1109/JSSC.2008.2004336.

57. W. Lee and A. Valdes-Garcia, "Continuous True-Time Delay Phase Shifter Using Distributed Inductive and Capacitive Miller Effect," in IEEE Transactions on Microwave Theory and Techniques, vol. 67, no. 7, pp. 3053-3063, July 2019, doi: 10.1109/TMTT.2019.2901678.

58. E. Lin, C. Huang, S. Tang, C. Su and Y. Wang, "A 36 GHz four-bit tunable all-pass phase shifter using 0.15-µm GaAs technology," TENCON 2015 - 2015 IEEE Region 10 Conference, 2015, pp. 1-4, doi: 10.1109/TENCON.2015.7372814.

59. T. Singh and R. R. Mansour, "Loss Compensated PCM GeTe-Based Latching Wideband 3-bit Switched True-Time-Delay Phase Shifters for mmWave Phased Arrays," in IEEE Transactions on Microwave Theory and Techniques, vol. 68, no. 9, pp. 3745-3755, Sept. 2020, doi: 10.1109/TMTT.2020.3007833.

60. T. Singh, N. K. Khaira and R. R. Mansour, "Thermally Actuated SOI RF MEMS-Based Fully Integrated Passive Reflective-Type Analog Phase Shifter for mmWave

Applications," in IEEE Transactions on Microwave Theory and Techniques, vol. 69, no. 1, pp. 119-131, Jan. 2021, doi: 10.1109/TMTT.2020.3018141.

61. J. Wu et al., "Compact, Low-Loss, Wideband, and High-Power Handling Phase Shifters With Piezoelectric Transducer-Controlled Metallic Perturber," in IEEE Transactions on Microwave Theory and Techniques, vol. 60, no. 6, pp. 1587-1594, June 2012.

62. Tae-Yeoul Yun and Kai Chang, "Analysis and optimization of a phase shifter controlled by a piezoelectric transducer," in IEEE Transactions on Microwave Theory and Techniques, vol. 50, no. 1, pp. 105-111, Jan. 2002, doi: 10.1109/22.981254.

63. H. Al-Saedi et al., "A Low-Cost Ka-Band Circularly Polarized Passive Phased-Array Antenna for Mobile Satellite Applications," in IEEE Transactions on Antennas and Propagation, vol. 67, no. 1, pp. 221-231, Jan. 2019, doi: 10.1109/TAP.2018.2878335.

64. Z. Rahimian Omam et al., "Tunable Substrate Integrated Waveguide Phase Shifter Using High Dielectric Constant Slab," in IEEE Microwave and Wireless Components Letters, vol. 30, no. 5, pp. 485-488, May 2020, doi: 10.1109/LMWC.2020.2980264.

65. N. Ranjkesh, M. Basha, A. Abdellatif, S. Gigoyan and S. Safavi-Naeini, "Millimeter-Wave Tunable Phase Shifter on Silicon-on-Glass Technology," in IEEE Microwave and Wireless Components Letters, vol. 25, no. 7, pp. 451-453, July 2015.

66. Z. R. Omam et al., "Ka-Band Passive Phased-Array Antenna With Substrate Integrated Waveguide Tunable Phase Shifter," in IEEE Transactions on Antennas and Propagation, vol. 68, no. 8, pp. 60396048, Aug. 2020, doi: 10.1109/TAP.2020.2983838.

67. K. Kibaroglu, M. Sayginer and G. M. Rebeiz, "A Low-Cost Scalable 32Element 28-GHz Phased Array Transceiver for 5G Communication Links Based on a 2×2 Beamformer Flip-Chip Unit Cell," in IEEE Journal of Solid-State Circuits, vol. 53, no. 5, pp. 1260-1274, May 2018, doi: 10.1109/JSSC.2018.2791481.

68. J. Curtis, Hongyu Zhou and F. Aryanfar, "A Fully Integrated Ka-Band Front End for 5G Transceiver," 2016 IEEE MTT-S International Microwave Symposium (IMS), 2016, pp. 1-3, doi: 10.1109/MWSYM.2016.7540314.

69. Y. Ji, L. Ge, J. Wang, Q. Chen, W. Wu and Y. Li, "Reconfigurable Phased-Array Antenna Using Continuously Tunable Substrate Integrated Waveguide Phase Shifter," in IEEE Transactions on Antennas and Propagation, vol. 67, no. 11, pp. 6894-6908, Nov. 2019, doi: 10.1109/TAP.2019.2927813.

70. D. Wang, E. Polat, H. Tesmer, R. Jakoby and H. Maune, "A Compact and Fast 1 x 4 Continuously Steerable End-Fire Phased-Array Antenna Based on Liquid Crystal," in IEEE Antennas and Wireless Propagation Letters, doi: 10.1109/LAWP.2021.3096035.

71. Nafe, F. A. Ghaffar, M. F. Farooqui and A. Shamim, "A Ferrite LTCC-Based Monolithic SIW Phased Antenna Array," in IEEE Transactions on Antennas and

Propagation, vol. 65, no. 1, pp. 196-205, Jan. 2017, doi: 10.1109/TAP.2016.2630502.

72. N. Kingsley, G. E. Ponchak and J. Papapolymerou, "Reconfigurable RF MEMS Phased Array Antenna Integrated Within a Liquid Crystal Polymer (LCP) System-on-Package," in IEEE Transactions on Antennas and Propagation, vol. 56, no. 1, pp. 108-118, Jan. 2008, doi: 10.1109/TAP.2007.913151.

73. K. Topalli, Ö. A. Civi, S. Demir, S. Koc and T. Akin, "A Monolithic Phased Array Using 3-bit Distributed RF MEMS Phase Shifters," in IEEE Transactions on Microwave Theory and Techniques, vol. 56, no. 2, pp. 270-277, Feb. 2008, doi: 10.1109/TMTT.2007.914377.

74. Franc, O. H. Karabey, G. Rehder, E. Pistono, R. Jakoby and P. Ferrari, "Compact and Broadband Millimeter-Wave Electrically Tunable Phase Shifter Combining Slow-Wave Effect With Liquid Crystal Technology," in IEEE Transactions on Microwave Theory and Techniques, vol. 61, no. 11, pp. 3905-3915, Nov. 2013, doi: 10.1109/TMTT.2013.2282288.

75. M. Jost et al., "Miniaturized Liquid Crystal Slow Wave Phase Shifter Based on Nanowire Filled Membranes," in IEEE Microwave and Wireless Components Letters, vol. 28, no. 8, pp. 681-683, Aug. 2018, doi: 10.1109/LMWC.2018.2845938.

76. Raeesi, H. Al-Saedi, W. M. Abdel-Wahab, S. Gigoyan and S. Safavi Naeini, "Ka-Band Circularly-Polarized Antenna Array with Wide Gain and Axial Ratio Bandwidth," 2021 15th European Conference on Antennas and Propagation (EuCAP), 2021, pp. 1-5, doi: 10.23919/EuCAP51087.2021.9411453.

77. Nafe, K. Kibaroglu, M. Sayginer and G. M. Rebeiz, "An In-Situ SelfTest and Self-Calibration Technique Utilizing Antenna Mutual Coupling for 5G Multi-Beam TRX Phased Arrays," 2019 IEEE MTT-S International Microwave Symposium (IMS), 2019, pp. 1229-1232, doi: 10.1109/MWSYM.2019.8701072.

78. W. M. Abdel-Wahab et al., "A Modular Architecture for Wide Scan Angle Phased Array Antenna for K/Ka Mobile SATCOM," 2019 IEEE MTT-S International Microwave Symposium (IMS), 2019, pp. 1076-1079, doi: 10.1109/MWSYM.2019.8700842.

79. K. K. W. Low, G. M. Rebeiz, S. Zihir and T. Kanar, "A Reconfigurable Dual-Polarized 1024-Element Ka-Band SATCOM Transmit Phased-Array with Large Scan Volume and +48 dBW EIRP," 2021 IEEE MTT-S International Microwave Symposium (IMS), 2021, pp. 638-640, doi: 10.1109/IMS19712.2021.9574982.

80. G. Gültepe, T. Kanar, S. Zihir and G. M. Rebeiz, "A 1024-Element Ku-Band SATCOM Phased-Array Transmitter With 45-dBW Single-Polarization EIRP," in IEEE Transactions on Microwave Theory and Techniques, vol. 69, no. 9, pp. 4157-4168, Sept. 2021, doi: 10.1109/TMTT.2021.3075678.

81. D. Liu, X. Gu, C. W. Baks and A. Valdes-Garcia, "Antenna-in-Package Design Considerations for Ka-Band 5G Communication Applications," in IEEE Transactions on Antennas and Propagation, vol. 65, no. 12, pp. 6372-6379, Dec. 2017, doi: 10.1109/TAP.2017.2722873.

82. A. H. Aljuhani, T. Kanar, S. Zihir and G. M. Rebeiz, "A 256-Element Ku-Band Polarization Agile SATCOM Transmit Phased Array With Wide-Scan Angles, Low Cross Polarization, Deep Nulls, and 36.5-dBW EIRP per Polarization," in

IEEE Transactions on Microwave Theory and Techniques, vol. 69, no. 5, pp. 2594-2608, May 2021, doi: 10.1109/TMTT.2021.3053293.

83. Y. Zhang and J. Mao, "An Overview of the Development of Antenna-in-Package Technology for Highly Integrated Wireless Devices," in Proceedings of the IEEE, vol. 107, no. 11, pp. 2265-2280, Nov. 2019, doi: 10.1109/JPROC.2019.2933267.

84. N. Ghaffarian et al., "Characterization and Calibration Challenges of an K-Band Large-Scale Active Phased-Array Antenna with a Modular Architecture," 2020 50th European Microwave Conference (EuMC), 2021, pp. 1039-1042, doi: 10.23919/EuMC48046.2021.9338111.

85. https://emagtech.com/emag-solutions/

86. Low, K. K. W., Zihir, S., Kanar, T., & Rebeiz, G. M. (2022). A 27-31-GHz 1024-Element Ka-Band SATCOM Phased-Array Transmitter With 49.5-dBW Peak EIRP, 1-dB AR, and±70° Beam Scanning. IEEE Transactions on Microwave Theory and Techniques.

87. X. Luo et al., "A Scalable Ka-Band 1024-Element Transmit Dual-Circularly-Polarized Planar Phased Array for SATCOM Application," in IEEE Access, vol. 8, pp. 156084-156095, 2020, doi: 10.1109/ACCESS.2020.3019174.